Transport coefficients of artificially modulated two-dimensional electron gases

Uzur, Dejan

Award date:
2004

Awarding institution:
University of Bath

TRANSPORT COEFFICIENTS OF ARTIFICIALLY MODULATED TWO-DIMENSIONAL ELECTRON GASES

Submitted by Dejan Uzur
for the degree of
Doctor of Philosophy
of the University of Bath
2004

ProQuest LLC
789 East Eisenhower Parkway
P.O. Box 1346
Ann Arbor, MI 48106-1346

Abstract

Transport coefficients of artificially modulated two-dimensional electron gases (2DEGs) have been investigated. Commensurability oscillations were observed in the phonon-drag thermopower of 2DEGs modulated by a periodic array of dysprosium stripes which resulted in electrostatic modulation of the electron system. These oscillations were found to be in phase with the commensurability oscillations measured in the longitudinal resistance of the same samples. Their origin was explained by assuming anisotropic scattering between electron and phonon systems. An exact solution of the Boltzmann equation, driven by an anisotropic electron-phonon scattering, agrees well with the experimental data. An effective temperature gradient, misaligned with the principal axis of anisotropy of the superlattice, correctly explained the observed antisymmetry of commensurability oscillations.

The diffusion thermopower of a multiprobe ballistic conductor in the form of caterpillarlike Sinai billiard was also investigated. Both longitudinal and transverse (Nernst-Ettingshausen effect) components of thermopower exhibit commensurability effects, more pronounced than the corresponding effects observed in magnetoresistance. Results of theoretical simulations based on the generalised Landauer-Büttiker approach were found to be in agreement with experimental results.

Oscillations periodic in perpendicularly applied magnetic field were observed in the magnetoresistance of samples modulated by lateral surface ferromagnetic dots and anti-dots. Such oscillations arose from singly periodic orbits which returned to their point of departure after n bounces on the dot profile. A semi-classical model was derived which correctly predicts the magnetic field increment required to depin shell n and $n+1$ from the magnetic billiard.

ACKNOWLEDGEMENTS

As one of my ex-colleagues once remarked, although "there are more people to thank than can be mentioned here", it is a worthwhile exercise, and I intend to give it a good go here.

I would like to start by thanking my supervisor, Dr. Alain Nogaret, for the guidance and supervision throughout the project. Without his support and enthusiasm I would not have been able to complete the work presented here. I would also like to thank Professor Simon Bending for granting access to experimental facilities, to our collaboration teams led by Dr. Arthur Pogosov, Dr. Chris Marrows and Professor J. C. Portal.

It is a pleasure to take this opportunity to express sincere gratitude to the following people, from the department of physics, who have proved an invaluable help over the years. Ms. Wendy Lambson for keeping the clean-room well-stocked with chemicals and in good working order, Mr. Bob Draper and Mr. Eddie Lambson for all the technical assistance, Mr. Mike Harriman for interesting electrical discussions, Mr. Barry Chapman for taking care of the electron-beam microscope, Dr. Peter Ford for making the ordering system seem effortless, Ms. Eva Ashford for the help with University bureaucracy and seemingly knowing everybody and everything, Mr. Adrian Hooper for IT support, and all the members of the school office.

I am also grateful to my friends and colleagues: Tom Hedley and Graham Cook for the social gatherings, Dr. James Gregory and Dr. David Lawton for creating an enjoyable working environment, Dr. William Reeves, Alex Brook, Dr. Alex Pross and Dr. Sasha Grigorenko for all their help, David Cole, Daria Sokhan, Dr. Richard Martin, Ruth Mason, Dr. Tom Kehoe and Nick Lambert for their companionship and generally interesting conversations. For providing me with the most enjoyable combination of sports and social life I thank Saul, Kathryn, Ross, Martin, Richard, Lyndsay, Jon, Robert, Doyle and a select few from the Bath Volleyball Club.

Finally, I would like to thank my family, and in particular my mother and sister, for their unquestioning support and encouragement. I dedicate this work to them, and to my father, who always knew I could do this.

PUBLICATIONS

The work presented in this thesis has led to the following publications:

D. Uzur, A. Nogaret, H. E. Beere, D. A. Ritchie, C. H. Marrows, B. J. Hickey; *Observation of the Electronic Shell Structure of Magnetic Billiards*, submitted to *Phys. Rev. B* 2003

D. Uzur, A. Nogaret, A. G. Pogosov, H. E. Beere, D. A. Ritchie; *Phonon-drag thermopower of lateral superlattices: the role of anisotropic scattering*, *J. Phys. Cond. Matt.* **15**, 6985, 2003

D. Uzur, A. Nogaret, S. J. Bending, C. H. Marrows, B. J. Hickey, H. E. Beere, D. A. Ritchie; *Standing waves of magnetic edge states in mesoscopic magnetic rings*, to be published in *Physica E*, 2003, and proceedings of EP2DS15 conference, Japan, 2003

D. Uzur, A. Nogaret, S. J. Bending, A. G. Pogosov, H. E. Beere, D. A. Ritchie; *Phonon drag thermopower of the periodically modulated two-dimensional electron gas*, proceedings of ICPS26 conference, Edinburgh, UK, 2002 (Oral contribution).

A. G Pogosov, M. V. Budantsev, D. Uzur, A. Nogaret, A. E. Plotnikov, A. K. Bakarov, A. I. Toropov; *Thermoelectric properties of a multiprobe ballistic conductor*, *Phys. Rev. B*, **66**, 201303, 2002

Contents

Chapter 1

Introduction

1.1 Background and motivation

The study of electrons or holes confined to quantum wells had been a theoretical subject until the advent of techniques which allowed the fabrication of thin films of these particles. In the early seventies, various research groups started work on molecular beam epitaxy (MBE) [1] and metal-organic chemical vapour deposition (MOCVD) [2], techniques which allow the growth of heterostructures containing thin layers of different semiconductors. A quantum confined layer of electrons, known as a two-dimensional electron gas, is formed at the interface between the different semiconductors.

Two-dimensional electron gases (2DEGs) formed at the interface between gallium arsenide and aluminium gallium arsenide ($GaAs/Al_xGa_{1-x}As$), have been a model choice for a majority of experimental work performed in the field of quantum transport and magnetoelectronics. In 1980 Klaus von Klitzing *et al.* [3] reported the observation of quantised Hall resistance by performing experiments on devices fabricated from such systems. Similar structures led to the discovery of the fractional quantum Hall resistance [4], weak localisation effects, edge state transport in point contacts, and most recently, in the measurements of thermal conductance [5] and in the definition of the quantum of thermal conductance [6]. Of course, a significantly larger amount of work, most of which is outside the scope of this thesis, has been performed on devices made from GaAs/AlGaAs

heterostructures.

The objective of the research reported here was to experimentally study the transport coefficients of artificially modulated two-dimensional electrons. This led to a comprehensive study of phonon-drag thermopower (PDTP) in periodically modulated 2DEGs, work prompted by the discovery of commensurability oscillations in magnetoresistance [7] and diffusion thermopower [8]. Such oscillations were explained [9] as a resonance between the periodic cyclotron motion and an oscillating $\mathbf{E} \times \mathbf{B}$ drift of the orbit centre induced by the superlattice. It was believed that the study of phonon-drag thermopower in such systems should lead to better understanding of electron-phonon coupling.

Transport studies have also been carried out on systems exhibiting dynamic chaos. It is well known that magnetoresistance can be used to distinguish between stable and chaotic electron orbits [10]. However, a kinetic coefficient much more sensitive to changes in conductivity has not been investigated in such systems. The results of experimental and theoretical studies of diffusion thermopower in Sinai billiards, which is proportional to the energy derivative of conductivity evaluated at the Fermi level, are reported. Such billiards, first proposed by a Russian mathematician Yakov Sinai [11], contain chains of anti-dots etched into a narrow wire. Both longitudinal and transverse magnetoresistance have been shown to exhibit commensurability effects at magnetic fields at which the classical cyclotron radius of the electron is equal to the integral number of periods of anti-dots.

Finally, the ability to distinguish between stable and chaotic electron orbits was also the motivation for the magnetoresistance studies of systems modulated by laterally defined magnetic dots and anti-dots. It was believed that, by forcing electrons to follow a closed path around a dot or an anti-dot, the wavelength of magnetic edge states could be determined. Such edge states form in the area between two regions of differing magnetic field.

Overview of the thesis

The rest of this chapter gives a brief introduction to the physics of two-dimensional electron gases, starting with their formation in GaAs/AlGaAs heterostructures. Following that, a discussion of electron transport regimes obtained by micro-

fabrication of 2DEG wafers is given, after which the principles of semiclassical transport theory based on the Boltzmann equation are introduced. The last section deals with the response of electrons to perpendicularly applied magnetic fields.

Chapter 2 contains information on the techniques used in the fabrication of working devices. Standard clean-room procedures such as wet-chemical etching and metal deposition, are briefly mentioned. Electron beam lithography techniques, developed and refined for the patterning of modulation structures in this project, are discussed in greater detail.

Experimental and theoretical results are discussed in chapters 3, 4 and 5. Magnetic field dependence of phonon-drag thermopower in periodically modulated two-dimensional electron gases is discussed in chapter 3. A brief introduction of the concept of thermopower is followed by experimental results of phonon-drag thermopower measurements in unmodulated 2DEGs. Results of magnetoresistance and magnetothermopower measurements in modulated 2DEGs are reported in the rest of the chapter, along with the failings of the current theory to explain the observed effects in PDTP. A modified theory which agrees well with experimental observations is given together with proposals for experiments which would test the robustness of the theory further.

Dynamic electron chaos is a theme common to chapters 4 and 5. Results of experimental study of magnetoresistance and diffusion thermopower of Sinai billiards are given as an introduction to chapter 4. Theory, based on the Landauer-Büttiker formalism and used in the Monte-Carlo simulations, successfully explains the origin of commensurability effects observed. The final experimental chapter presents magnetotransport results of lateral magnetic dots and anti-dots. The dependence of resistance on electron density, modulation strength and radius of the structure precedes a discussion of a theoretical model used to fit the data. Finally, the last chapter summarises the work and presents conclusions and recommendations for further work in these areas.

1.2 Two-dimensional electron gases

Two-dimensional electron gases differ from thin metal films through a number of desirable properties, such as low electron density (and correspondingly a large Fermi wavelength) and a large mean free path. At very low temperatures (below 1K), quantum mechanical phase coherence in the system can be maintained over distances exceeding several micrometers, making this a very convenient system in the study of ballistic and phase coherent transport. Since this behaviour is intermediate between quantum and macroscopic, the physics of low-dimensional systems is known as mesoscopic.

Growth of semiconductor heterostructures is strongly influenced by three important properties of the constituent semiconductors, and the first requirement is that the 'raw' materials are of highest purity and crystalline perfection. The second requirement places a limit on the difference between the lattice constants of the semiconductors: the heterostructure must have no strain between different layers, and in order to achieve this, lattice constants must not differ by more than 1%. This requirement means that the formation of dislocations which can trap electrons is also reduced. Finally, the difference in the energy band gap between two semiconductors must be sufficiently large in order that the potential well produced is deep enough to trap electrons within it.

Figure 1.1 shows the energy band diagram of a GaAs/AlGaAs heterojunction. Due to the smaller energy gap (E_g) between the valence and conduction bands in GaAs as opposed to AlGaAs, quantum confinement of electrons occurs in the GaAs layer.

In order to form a 2DEG, electrons must be free to move in the conduction band. As figure 1.1 shows, if the GaAs/AlGaAs heterostructure is neutral, the conduction band is flat, and the electrons are not free to move. By applying a technique known as modulation doping, impurities are introduced into the heterostructure, resulting in a positively doped AlGaAs region. Assuming that the GaAs region is left undoped, electrons move away from the doped region of AlGaAs towards the undoped GaAs. This simple picture is not complete, however, because Coulomb interaction arising between electrons released by impurities and the charged impurities left behind results in electron – ionised-impurity scattering. This type of scattering restricts the motion of electrons through the structure and reduces

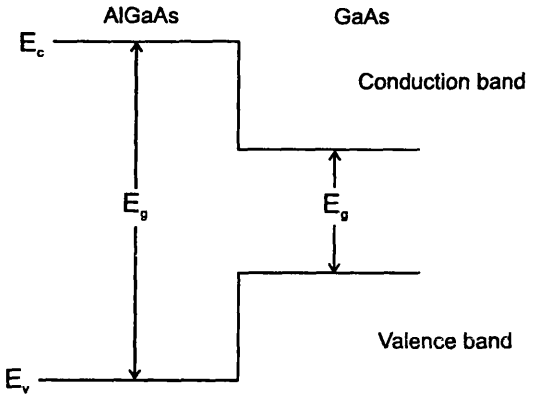

Figure 1.1: A gallium arsenide/aluminium gallium arsenide heterojunction.

electron mobility in the sample.

Electrons which cross into the GaAs layer lose some energy due to the offset in energy between the conduction bands of GaAs and AlGaAs, and once that happens, they become trapped in the GaAs region. The kinetic energy of these electrons changes at the heterojunction, and the potential energy arises from the electrostatic potential, set-up because of the separation of charged impurities and electrons. If the electrostatic potential is assumed to be $\phi(z)$, the electron potential energy is $-e\phi(z)$, where e is the electronic charge, and the total energy at the bottom of the GaAs conduction band is then the sum of the kinetic and potential energy contributions. Clearly, the difference between the conduction band energies acts as one side of a potential well as the electrostatic field cannot move electrons back into the AlGaAs layer, and the electrostatic potential, $\phi(z)$, pushes them against the interface. The resulting potential well has a triangular shape, with the motion along the direction of growth of the heterostructure quantised. The process of obtaining a two-dimensional electron gas is shown schematically in figure 1.2.

Electron – ionised-impurity scattering is reduced by the introduction of an undoped spacer layer between the doped AlGaAs and GaAs. This increases electron mobility, however, it also leads to a reduction in electron density of the 2DEG since electrons have to travel a longer distance to reach the heterojunction.

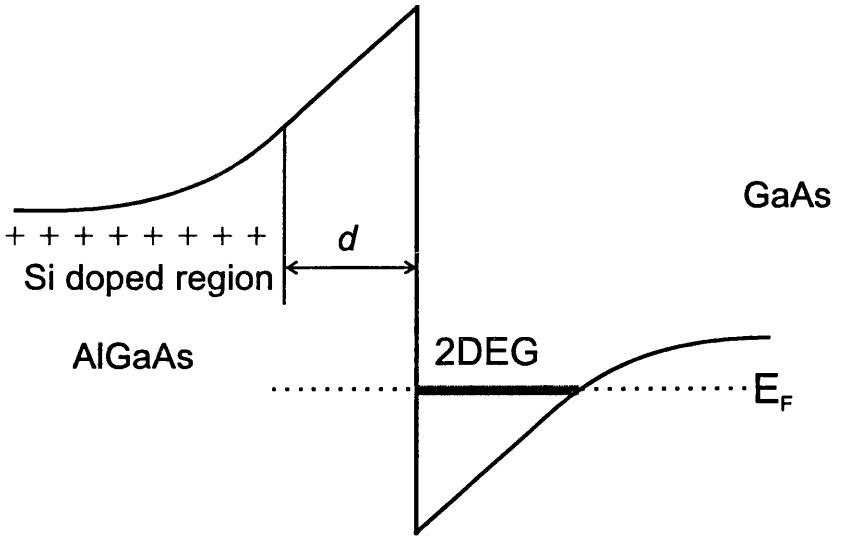

Figure 1.2: Bending of the conduction band in a modulation doped GaAs/$Al_xGa_{1-x}As$ heterostructure. The 2DEG layer is formed at the interface between the positively doped AlGaAs and the undoped GaAs layers.

1.3 Electron transport in mesoscopic conductors

The fabrication of samples in which electron-impurity scattering can be controlled has become a reality following the advent of various heterostructure-microfabrication techniques. This opened up many new possibilities in the studies of quantum transport, some of which are described in this thesis. The rest of this section describes the three transport regimes obtainable.

In mesoscopic systems, in which the size of the sample is smaller than the quantum mechanical phase coherence length, two length scales determine the regime in which electrons move. One is the electron mean free path, defined as the distance an electron moves between two successive scattering events with an impurity. It is given by the product of electron's Fermi velocity, v_F, and the electron-impurity scattering time, τ_{ei}. The second length scale depends on the geometry of the device patterned out of the semiconductor nanostructure. In the simplest case of a thin wire, the important length scales are the wire width, w, and the length, L, whereas in the case of a quantum dot, the only important length scale is the diameter, d.

The regime in which the mean free path of electrons is much larger than the width and length of the wire ($l \gg w, L$) can be achieved either by having large electron density and long electron-impurity scattering time, or by reducing the wire width and length sufficiently. It is known as a ballistic regime, and the enhancement to the resistance is due to diffuse scattering of electrons from the boundary walls. In this regime, conductance ($G = (e^2/h)T$, where T is the probability of transmission between probes) is the only important property (conductivity plays no role), and the resistance is independent of the length of the sample. A schematic diagram of a thin-film wire in ballistic regime is shown in figure 1.3(a).

In the other limit, when the mean free path of the electron is much smaller than the width or the length of the wire ($l \ll w, L$), the electrons suffer multiple collisions with impurities before reaching the walls of the wire. The resistance of samples in the diffusive regime arises due to impurity scattering. A schematic diagram of this regime is shown in 1.3(b).

The regime in which the mean free path of the electron and the geometrical size of the sample are comparable ($w < l < L$), is known as quasi-ballistic. The probability of electrons suffering collisions with impurities and wire walls, and consequently the contribution to resistance from these events, is roughly the same. Quasi ballistic regime is shown schematically in figure 1.3(c).

1.4 Principles of semiclassical transport theory

The study of transport coefficients reported in this work has been performed in the semi-classical regime. This is the regime of small magnetic fields ($B < 0.5$T) in which the electron energy spectrum is continuous. In such a regime, motion of electrons under the influence of external fields, temperature gradients and scattering effects by impurities is governed by the Boltzmann equation, the main principles of which are introduced in this section.

Statistically, the local concentration of electrons in a state $\mathbf{k}$ at a point $\mathbf{r}$ in space, is described by the non-equilibrium, local Fermi-Dirac distribution function, $f(\mathbf{k}, \mathbf{r}, t)$. Here, $\mathbf{k}$ and $\mathbf{r}$ are the two-dimensional electron wavevector and position vector, respectively. The application of a temperature gradient, for ex-

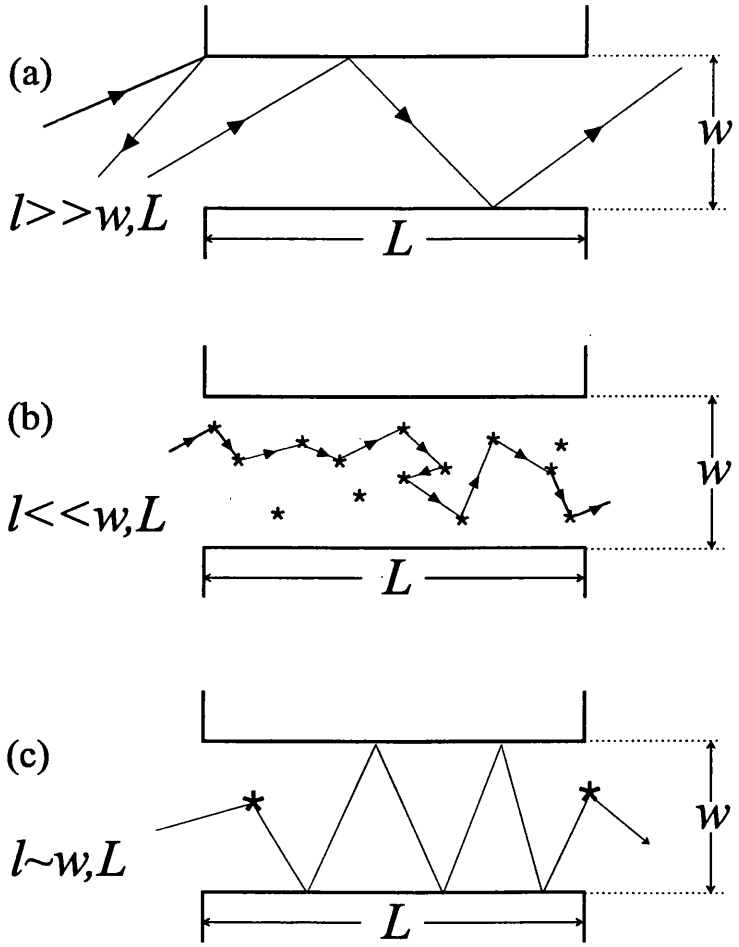

Figure 1.3: Collisions electrons suffer in artificial potential landscapes. Part *a* shows electrons in the ballistic regime where the electron mean free path, l is larger than the length and the width of the channel ($l \gg w, L$). Part *b* is the diffusive regime ($l \ll w, L$) where the electron-impurity collisions dominate. Part *c* is the intermediate regime ($w < l < L$) and the electron-impurity and wall collisions occur with roughly the same probability.

ample, moves electrons out of the region described by $\mathbf{r}$. The electrons are said to diffuse in the temperature gradient, and taking their velocity as $\mathbf{v_k}$, they travel a distance $t\mathbf{v_k}$ in a time t. According to Liouville's theorem, the volume in phase space is invariant and so the number of electrons at position $\mathbf{r}$ at a time t will be the same as the number of electrons at position $\mathbf{r} - t\mathbf{v_k}$ at a time $t = 0$, i.e. $f(\mathbf{k}, \mathbf{r}, t) = f(\mathbf{k}, \mathbf{r} - t\mathbf{v_k}, 0)$. Taking these arguments into account, the rate of change of electron distribution due to diffusion can be expressed as shown in equation 1.1.

$$\left.\frac{\partial f_\mathbf{k}}{\partial t}\right|_{diffusion} = -\mathbf{v_k}.\frac{\partial f_\mathbf{k}}{\partial \mathbf{r}} = -\mathbf{v_k}.\nabla f_\mathbf{k} \tag{1.1}$$

In addition to the effect of temperature gradients, electron distribution can also be altered by application of electric ($\mathbf{E}$) and magnetic ($\mathbf{B}$) fields. In contrast to the previous case where the temperature gradient acted to change the electron distribution in space, the magnetic field acts to change the electron wavevector, $\mathbf{k}$. The rate of change of $\mathbf{k}$ is shown in equation 1.2.

$$\frac{\partial \mathbf{k}}{\partial t} = -\frac{e}{\hbar}\left(\mathbf{E} + \mathbf{v_k} \times \mathbf{B}\right) \tag{1.2}$$

The rate of change of $\mathbf{k}$ can be thought of as velocity of an electron in momentum space, and electron distribution at time t is then given as $f(\mathbf{k}, \mathbf{r}, t) = f(\mathbf{k} - \dot{\mathbf{k}}t, \mathbf{r}, 0)$. Equation 1.3 is the rate of change of $f(\mathbf{k}, \mathbf{r}, t)$ under the influence of $\mathbf{E}$ and $\mathbf{B}$ fields.

$$\left.\frac{\partial f_\mathbf{k}}{\partial t}\right|_{field} = -\frac{\partial \mathbf{k}}{\partial t}.\frac{\partial f_\mathbf{k}}{\partial \mathbf{k}} = -\frac{e}{\hbar}\left(\mathbf{E} + \mathbf{v_k} \times \mathbf{B}\right).\frac{\partial f_\mathbf{k}}{\partial \mathbf{k}} \tag{1.3}$$

If the application of a temperature gradient and magnetic field moves the electron distribution out of equilibrium, then the scattering of electrons by impurities can bring it back to equilibrium. If the electron is in state $\mathbf{k}$ before a collision, then after a collision it is in state $\mathbf{k}'$. Scattering events $\mathbf{k} \rightarrow \mathbf{k}'$ clearly decrease $f(\mathbf{k}, \mathbf{r}, t)$, but the reverse process ($\mathbf{k}' \rightarrow \mathbf{k}$), which is also possible, increases $f(\mathbf{k}, \mathbf{r}, t)$. Whether or not an electron is scattered from state $\mathbf{k}$ to $\mathbf{k}'$ is dependent

on the number of electrons in state $\mathbf{k}$, and the number of vacancies in $\mathbf{k}'$ (the opposite is true for the other scattering case). If there was a way of knowing that the state $\mathbf{k}$ is occupied and state $\mathbf{k}'$ is empty, then the rate of transition between these two states ($Q(\mathbf{k}, \mathbf{k}')$) would be known. Taking into account these weighting factors, the rate of change of $f(\mathbf{k}, \mathbf{r}, t)$ due to scattering is given by equation 1.4.

$$\frac{\partial f_{\mathbf{k}}}{\partial t}|_{scattering} = \int \{f_{\mathbf{k}'}(1 - f_{\mathbf{k}}) - f_{\mathbf{k}}(1 - f_{\mathbf{k}'})\} Q(\mathbf{k}, \mathbf{k}') d\mathbf{k}' \tag{1.4}$$

According to the Boltzmann equation, the net change in the electron distribution is zero, and this is true at any point in space $\mathbf{r}$, and for every value of $\mathbf{k}$. Therefore, the sum of the rates of change of $f(\mathbf{k}, \mathbf{r}, t)$ due to the application of temperature gradients, external magnetic fields and scattering events is zero, as shown in equation 1.5.

$$\frac{\partial f_{\mathbf{k}}}{\partial t}\bigg|_{diffusion} + \frac{\partial f_{\mathbf{k}}}{\partial t}\bigg|_{field} + \frac{\partial f_{\mathbf{k}}}{\partial t}|_{scattering} = 0 \tag{1.5}$$

Although this is not an extensive analysis of the semiclassical transport theory, the contents of this section should be useful in the understanding of some of the theoretical analysis which follows.

1.5 Response of electrons to magnetic fields

Although the Boltzmann equation contains a lot of information about the effect an applied magnetic field has on the distribution of electrons in space, it is also important to understand its effect on the energy and motion of individual electrons. All studies reported in this thesis were performed primarily as a function of magnetic field applied perpendicularly to the 2DEG layer, and it is the aim of this section to introduce this subject.

As shown in equation 1.2, magnetic field acts to change the magnitude and direction of the electron wavevector $\mathbf{k}$. By expressing equation 1.2 as $\hbar \partial \mathbf{k}/\partial t$, the effect of the field can be considered as a force acting on the electron. This is

the Lorentz force, given by equation 1.6, where the velocity of electrons is $\mathbf{v}$ and magnetic field is $\mathbf{B}$.

$$\hbar\frac{\partial \mathbf{k}}{\partial t} = -e\mathbf{v} \times \mathbf{B} \tag{1.6}$$

Lorentz force acts in a direction perpendicular to the velocity forcing electrons to move in a circle. Electron motion and the velocity are in a plane perpendicular to the applied field, as shown in a simple diagram in figure 1.4.

Since the force is perpendicular to the velocity, no work is done on the electron. Equation 1.6 is a form of Newton's law, and expressing acceleration as $v\frac{d\theta}{dt}$, where $d\theta$ is the angle electron moves through in time dt, it can be seen that the angular frequency of the electron is proportional to the applied magnetic field, as shown in equation 1.7.

$$\frac{d\theta}{dt} = \omega_c = \frac{eB}{m} \tag{1.7}$$

Angular frequency, ω_c is known as cyclotron frequency, and m in equation above is the electron mass.

The effect of the magnetic field on the energy of electrons is defined by the solution of Schrödinger equation. In the presence of a magnetic field, the canonical

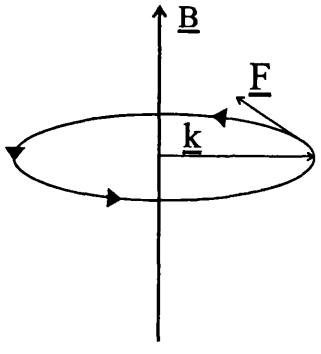

Figure 1.4: Force acting on an electron moving in a plane perpendicular to the direction of applied magnetic field B.

momentum of an electron ($\mathbf{p} = -i\hbar\nabla_{\mathbf{r}}$) is given by the sum of the kinetic ($m\mathbf{v}$) and electromagnetic momenta ($q\mathbf{A}$). Defining the Hamiltonian of the electron as

$$\hat{H} = \frac{1}{2m}\left(-i\hbar\nabla + e\mathbf{A}\right)^2, \tag{1.8}$$

allows the Schrödinger equation to be written as

$$-\frac{\hbar^2}{2m}\left[\frac{\partial^2}{\partial x^2} + \left(\frac{\partial}{\partial y} - \frac{ieBx}{\hbar}\right)^2 + \frac{\partial^2}{\partial z^2}\right]\psi = E\psi. \tag{1.9}$$

The vector potential $\mathbf{A}$ was taken in the Landau gauge ($\mathbf{A}(\mathbf{r}) = (0, Bx, 0)$) by assuming that the applied magnetic field is in the z-direction. Solution of equation 1.9 has the form $\psi(x, y, z) = u(x)exp[i(k_y y + k_z z)]$, and using this, the energy eigenvalue of an electron in a magnetic field is given by

$$E_n = \frac{\hbar^2 k_z^2}{2m} + \left(n + \frac{1}{2}\right)\hbar\omega_c. \tag{1.10}$$

Motion of electrons parallel to the z-direction is unaffected by the field, and energy dependence on k_z is the same as for a free electron in the absence of a field. However, motion in the z-direction in a 2DEG is completely absent, and the three-dimensional result of equation 1.10 is replaced by the two-dimensional analogue

$$E = E_0 + (n + \frac{1}{2})\hbar\omega_c, \tag{1.11}$$

where E_0 is the energy of the bottom subband. Equation 1.11 shows that the energy spectrum of electrons laterally confined to a narrow channel is fully discrete. Quantisation of energy into levels, known as Landau levels ($n = 0, 1, 2..$), occurs at high magnetic fields, $\omega_c\tau_{ei} \gg 1$. Each Landau level has the same number of states per unit area, and this is equal to one state per flux quantum (h/e) through the sample.

Energy quantisation causes the density of states at the Fermi level ($n(E_F)$) to oscillate. Since, according to the Fermi Golden Rule, the scattering rate (τ_{ei}^{-1}) is proportional to the density of states, and the Drude resistivity is proportional to the scattering rate, the oscillatory behaviour of $n(E_F)$ is reflected in resistivity. At integer Landau level filling factors ($\nu = (n_s h)/(g_s g_v eB = 1, 2, 3..)$, where factors g_s and g_v account for spin and valley degeneracy respectively), the Fermi level lies between two Landau levels and the resistivity is minimum. Increasing the magnetic field increases the separation of Landau levels and when the Fermi level is 'inside' a Landau level, the resistance is maximum. The B^{-1}-periodic oscillations which arise in magnetoresistance due to oscillatory density of states are known as Shubnikov – de-Haas oscillations (SdH).

Chapter 2

Device design and microfabrication techniques

2.1 Introduction

This chapter contains the background information required in the understanding of the design and microfabrication of working experimental devices. The first section schematically outlines the devices used. In the next section, the process by which working devices were obtained is briefly mentioned, and the technique which allowed the patterning of modulation structures is explained in some detail. Finally, the experimental set-up and different measurements performed on the devices is discussed.

2.2 Device design

Figure 2.1 shows the four different samples designed in order to study different transport coefficients. Part *a* of this figure shows samples used in the measurement of phonon-drag thermopower (PDTP) of periodically modulated 2DEGs. Since total thermopower is a sum of diffusion and phonon-drag contributions, which are not easily separable, it was crucial to design samples for PDTP measurements in which the detected diffusion component is minimised. The fact

that electrons thermally diffuse through relatively short distances ($\sim 100\mu m$) meant that diffusion could be suppressed if the voltage-probe separation exceeded 100μm. As figure 2.1(a) shows, five voltage/current probes separated by $1000\mu m$ were fabricated on either side of a $50\mu m$ wide Hall channel. Two different superlattices were designed: one in which the period was 500nm and the width of individual stripes was 200nm, and one with 1000nm period and 400nm wide stripes. Homogenous modulation of the 2DEG was obtained by fabricating the superlattice over most of the Hall channel length. It should be noted here that this was the first time a superlattice was fabricated over distances in excess of 4 millimeters.

Sample shown in part (b) was designed for the study of the effect of tilted temperature gradients on PDTP in periodically modulated 2DEG. Eight voltage/current probes, fabricated on a 10μm wide Hall channel, were much closer together (4μm separation) compared to the original samples. The four heating lines were not in electrical contact with the main Hall channel, to suppress the diffusion thermopower component from the detected signal. The superlattice was defined to cover the whole length of the channel (40μm).

In order to determine the effects of 2, 3 and 4μm diameter dots or anti-dots on magnetotransport, an 8μm channel was designed with 7 voltage probes on each side and two current probes parallel to the channel. The different radius dots/anti-dots were then patterned in the centre of every other Hall cross, thus allowing measurements to be performed on each individual dot/anti-dot. The novelty in the design of this sample compared to previous work [12] is that the gap between the dot edge and channel edge (2-3μm) is large enough to prevent scattering of magnetic edge states by the channel boundaries. A gate layer was designed to allow the study the magnetotransport dependence on electron density. The gate also had a dual purpose in that it was used to prevent oxidation of dysprosium, a common problem leading to electrostatic modulation of the electron layer. The outline of the sample is shown in figure 2.1(c).

The design of the samples used in diffusion thermopower measurements was relatively straightforward. A short chain of anti-dots was sufficient in creating the modulation of electron layer, therefore, the sample dimensions could be kept to a minimum. Two current probes were designed to extend from the extremities of the Hall channel. Two voltage probe pairs were designed to encompass the

entire anti-dot chain, and a further probe pair was placed in the middle of the chain. Longitudinal resistance and thermovoltage could then be measured across the entire chain or only half the chain. It also allowed the study of the effect of the billiard on transverse resistance and thermovoltage, since a comparison could be made between R_{xy} (U_{xy}) measured away from the chain, and in the middle of the chain. Device layout is shown in figure 2.1(d).

The layout of the devices was scaled to the right dimensions using computer aided design, and physical masks used in optical lithography were then fabricated at the Rutherford-Appleton Laboratory. The masks were made by evaporating chromium onto a slide which is transparent to ultra-violet light. The rest of this chapter gives a brief outline of fabrication techniques which allowed the fabrication of working devices from the designs.

2.3 Device fabrication

This section outlines the microfabrication techniques used to fabricate working devices from the designs. The majority of the work described is standard processing technology and is briefly mentioned. However, the use of electron beam lithography in the definition of modulation structures was refined for the purposes of this project and will be described in depth.

2.3.1 Properties of 2DEG wafers

Experimental devices were fabricated from epitaxially-grown GaAs/$Al_{0.3}Ga_{0.7}As$ layers, and physical properties of these wafers are given in table 2.1.

Wafers CL1 and CL2 were grown by D. A. Ritchie and H. E. Beere at the Cavendish Laboratory, University of Cambridge, by remote δ-doping technique in which a narrow silicon layer was grown at the centre of a wide AlGaAs layer. This technique allowed the growth of shallow 2DEGs, a desirable property which was unfortunately counterbalanced by the relative inaccuracy in controlling the physical properties, such as electron density and mobility, of the wafer during growth. The depth of the 2DEG below the surface in CL1 and CL2 samples

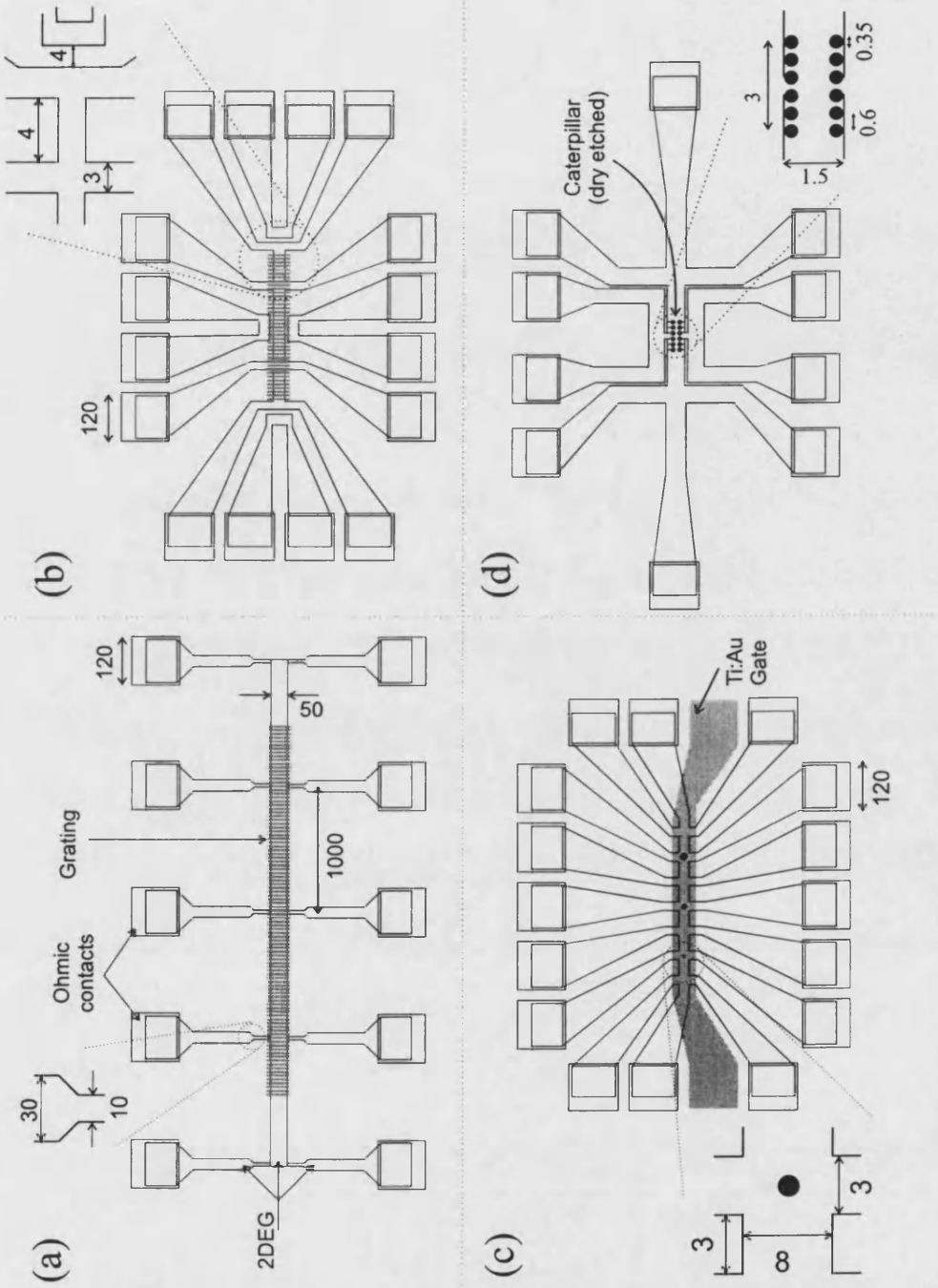

Figure 2.1: Schematic diagrams of the samples used in the measurement of phonon-drag thermopower (a) and (b), magnetic ring oscillations (c) and diffusion thermopower (d). The dimensions in the figure are expressed in micrometers.

Sample name	2DEG depth (nm)	$n_s(\times 10^{15} m^{-2})$ (dark)	$n_s(\times 10^{15} m^{-2})$ (light)	$\mu(m^2/Vs)$ (dark)	$\mu(m^2/Vs)$ (light)
NU1	24	1.9	3.3	59.6	114.0
NU2	24	1.5	3.1	31.9	107.9
CL1	30	5.3	11.1	34.7	47.6
CL2	50	3.3	6.9	71.6	160.0
ISP1	24	1.0	3.0	60.0	80.0

Table 2.1: Physical properties of samples used in experiments. Electron densities were calculated from Hall resistance measurements; *dark* refers to density after the initial cool-down and *light* refers to density at saturation.

was determined by assuming that the total width of the AlGaAs layer was Xnm (the width of the spacer layer $X/2$) and therefore the depth of the 2DEG was $X + 5$nm since the heterostructure was capped by a 5nm GaAs layer. Value of X in CL1 and CL2 was 25 and 45nm, respectively, giving the 2DEG depths in these samples as shown in table 2.1.

In wafers NU1, NU2 (grown by M. Henini, Nottingham University) and ISP1 (grown by A. K. Bakarov and A. I. Toropov, Institute of Semiconductor Physics, Russia) the narrow silicon layer was grown at the centre of a narrow GaAs layer. This type of δ-doping technique also produced a shallow quantum well, however, mobility in these wafers was reduced by electron-dopant impurity scattering due to their close proximity. As table 2.1 also shows, electron density in NU1, NU2 and ISP1 wafers was smaller compared to the CL1 and CL2 samples.

2.3.2 Optical lithography

Optical lithography is a method by which features of a device are patterned on a wafer by relying on the optical properties of an organic polymer, called photo-resist, sensitive to ultra-violet (UV) light. A $\sim 1.3\mu$m thick [13] layer of photo-resist was obtained by covering the wafer in resist and spinning at 4000rpm for 30 seconds. Following that, the resist was baked for either 30 minutes at 90°C (if the exposed pattern was being etched), or for 15 minutes at 90°C, followed by a 15 minute soak in chlorobenzene and another 15 minute–90° baking stage if metals were being thermally evaporated onto the wafer.

The transfer of device pattern was done by placing the optical mask into contact

Sample →	NU1	NU2	CL1	CL2	ISP1
2DEG depth (nm)	24	24	30	50	24
Etch depth (nm)	300	300	46	70	100

Table 2.2: Table of etch depths of experimental devices.

with the wafer and shining ultra-violet light through it. Light which passes through the transparent areas of the mask hits the wafer and weakens the bonds between polymers of the resist. The weakened resist bonds are then completely broken and removed from the wafer by photoresist developer.

2.3.3 Wet chemical etching

Following the first stage of optical lithography, in which the Hall channel and voltage/current probes were patterned, wafers were wet-chemically etched in order to confine the 2DEG layer to only those regions. For this purpose, an ammonia etch solution (HNO_4:H_2O_2:H_2O in proportion 1:1:50) with an etch rate of 8nm/s, was prepared. By immersing the wafer into the solution for different lengths of time, different etch depths were obtained, as shown in table 2.2.

2.3.4 Fabrication of electrical contacts and gate layers

In general, electrical contact to a 2DEG layer can be made by the deposition and subsequent annealing of metals or metallic alloys, following which the Fermi levels of the metal and semiconductor line up. This occurs as a result of electron diffusion across the induced metal-semiconductor junction.

The fabrication of metallic contacts results in a fraction of a subsequently measured signal being due to the voltage drop across such contacts and a fraction across the active region of the 2DEG. In order to minimise the drop across the contacts, their resistance must be kept low. Low contact resistance is achieved by heavy doping of the semiconductor layer underneath the metal, reducing the width of the depletion layer. In this configuration electrons quantum mechanically tunnel through the induced Schottky barrier, and the contact resistance

decreases exponentially with increasing doping density.

In all samples used in this project, the Ohmic contacts were made by annealing thermally evaporated films of germanium (60nm), gold (90m), nickel (30nm) and gold (200nm) in an inert-gas chamber. The diffusion of gallium into the eutectic alloy, formed by gold and germanium, left vacant sites in the GaAs lattice. These sites became occupied by germanium which formed the necessary highly doped region in the semiconductor. Nickel layer was fabricated in order to prevent 'balling' of metals, which would result in rough contact surface, and also to aid inter-diffusion of germanium into GaAs.

Gate layer was fabricated by thermally evaporating 33nm of titanium and 200nm of gold. The presence of a gate layer induced a Schottky barrier forcing the conduction and valence bands to bend in order to equalise the Fermi level throughout the device. The application of a bias voltage to the gate then forced further adjustment of the Fermi level, and this resulted in the change of the carrier density observed.

2.3.5 Electron beam lithography

The advantage of optical lithography is the relative ease of use and the ability to expose multiple patterns at the same time. However, the major flaw is that the smallest features which can be defined are of the order of 1μm. Due to their size, the superlattice, shown in figure 2.2 and dot/anti-dot structures, shown in figure 2.3, were patterned by electron beam lithography.

Electron beam lithography (EBL) was performed using an integrated Hitachi – Raith advanced scanning electron microscope nanolithography system. The movement of the sample stage and the electron tip during the pattern definition was controlled by Raith software and hardware [14]. The ability of the software to interpret computer files written in GDSII format meant that no physical mask was needed for EBL, and this is the main difference in pattern transfer between optical lithography and EBL.

The preparation of the wafer for lithography involved the deposition of a thin layer of polymethylmethacrylate (PMMA), an electron-energy sensitive resist.

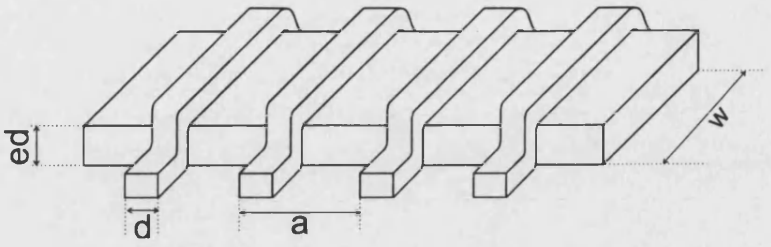

Figure 2.2: The schematic outline of the lateral surface superlattices superimposed on a Hall channel of width w and etch-depth ed. The width of individual stripes was $d = 200$ and 400nm and the period of superlattice was $a = 500$ and $a = 1000$nm, respectively.

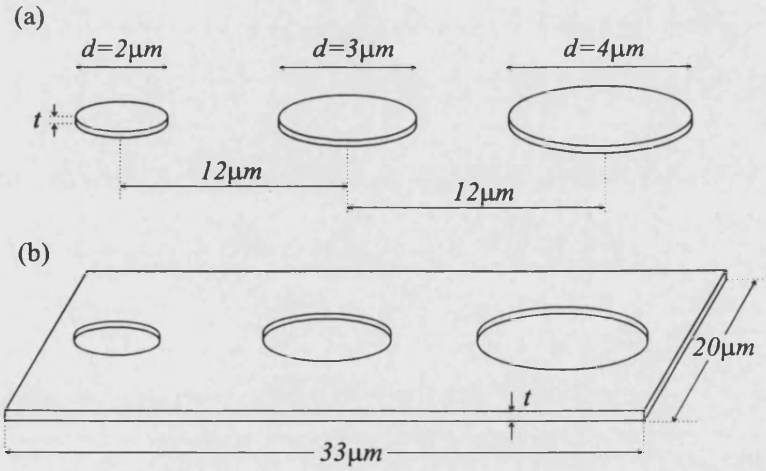

Figure 2.3: The outline of the (a) dot and (b) anti-dot structures. Radii of the anti-dots were the same as those of the corresponding dots. Three thicknesses of dysprosium were used on different devices, $t = 75, 150, 225$nm.

A 30 second spinning stage (at 4000rpm), followed by a 30 minute baking at 150°C, resulted in a 250nm thick layer, which was found to give the best exposure results. Before the patterns could be exposed, it was important to align the coordinate system of the microscope (x,y,z) with that of the lithography system (u,v,w). The alignment was aided by the presence of registration marks which were thermally evaporated onto the wafer at the same time as the contact pads. Three marks, oriented so that they form a right angle between them, were used, and the alignment accuracy was improved by choosing marks at the edges of the wafer. The (x,y,z) coordinate was then read for every point and adjusted by the software which had assigned the (u,v,w) coordinate for that point. By knowing the coordinates of each point in both systems, the computer calculated the angle of misalignment between the (x,y) and (u,v) axes.

The next stage involved choosing the correct writefield for the exposure. Writefield is defined as the size of a square which contains all of the features being exposed, and a 50μm writefield was used for both superlattice and dot/anti-dot structures. Microscope resolution associated with every writefield is inversely proportional to the size of the writefield, consequently, using a small writefield, small features can be patterned. The final alignment step was the alignment of the writefield itself. The idea behind this is that the sample on which a pattern is being exposed has a finite thickness and a random orientation on the sample holder, and by aligning the writefield, correct 'zoom factor' and sample rotation could be determined. In essence, this means that a 1μm feature on the computer will be exposed as a 1μm feature on the sample.

Writefield alignment was aided by the presence of alignment feature (cross made out of five 20 $\times$ 20μm squares) on the sample. The cross was defined by optical lithography and metallised at the same time as the contact pads. The microscope was then used to measure the distance of three points on the cross (refer to figure 2.4) relative to the reference point. Since these distances are known precisely (from the mask design), they were input into the microscope computer which then calculated the correct zoom factor. This zoom factor, along with sample rotation angle, were then sent to the digital-to-analogue converters interfacing the computer and the microscope.

Once the alignment process was completed, the correct exposure dose was determined. Exposure dose refers to the amount of electron flux used to expose

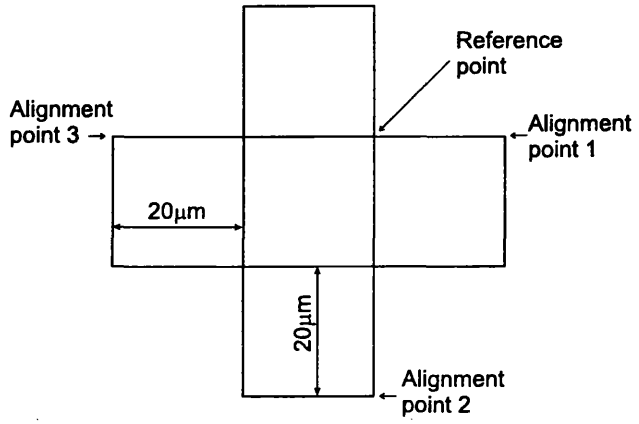

Figure 2.4: Alignment mark used to align the writefield in electron beam lithography.

a certain feature, and is inversely proportional to the feature area. Equation 2.1 was used to calculate the approximate exposure dose. Knowing the approximate dose, an exposure array was written (on a test sample) in which the dose was changed incrementally around this approximate value. Following the 30 second development (in IPA 3:1 MIBK mixture), the exact dose was determined by comparing the patterns in the array.

$$dose \propto \frac{I_{beam} t_{dwell}}{A_{feature}} \tag{2.1}$$

In equation 2.1, I_{beam} is the beam current (in μA), measured by placing the electron gun over a Faraday cup on the sample holder. The dwell time, t_{dwell}(s), is the time the gun spends over the smallest area (few nm^2) into which the area of the whole feature is divided, and the $A_{feature}$ is the area of the whole feature to be exposed (in cm^2). The final stage of electron lithography was the patterning of the modulation structures on the working devices. In order to obtain the best results, the modulation on each Hall channel was patterned individually.

2.4 Cryomagnetic system and measurement set-up

This section describes the operation of the liquid helium cryostat and measurement system used in the project. The experimental set-up consisted of two central components, lock-in amplifier, used to supply the excitation current and detect voltage drop, and a high voltage/high current powering the superconducting coil providing the external magnetic field.

2.4.1 Cryomagnetic system

The T=4.2K experiments were carried out in a liquid helium cryostat shown in figure 2.5. The cryostat consists of three chambers: the inner helium jacket, the outer nitrogen jacket and a vacuum jacket placed in-between which reduces heat transfer between the two adjoining compartments. The sample was placed inside the superconducting solenoid immersed in the liquid helium bath. In order to prevent the freezing of atmospheric gases present in the sample space at room temperature, the chamber was pumped down using a rotary pump. The heat transfer between the sample and the helium bath was then established by introducing helium exchange gas into the chamber.

Sample probe, shown as the inset to figure 2.5, contained the sample oriented perpendicular to the field produced by the niobium wire magnet. The electrical wires were housed inside the cylindrical tube and were attached to the sample on the bottom end, and to the contact boxes outside the cryostat. The infra-red LED placed vertically above the sample was used to change the electron density of the 2DEG during the experiments.

The sub-Kelvin experiments (300-600mK range) were performed at the High Magnetic Field Laboratory in Grenoble. The sample probe system is essentially the same as the one just described. Low temperature was achieved in the helium dilution refrigerator in which a mixture of He^3 and He^4 is cooled to below 0.9K. Extracting the vapour from the fridge, which results from the separation of helium mixture into two different phases, allows the temperature to be kept in the mK

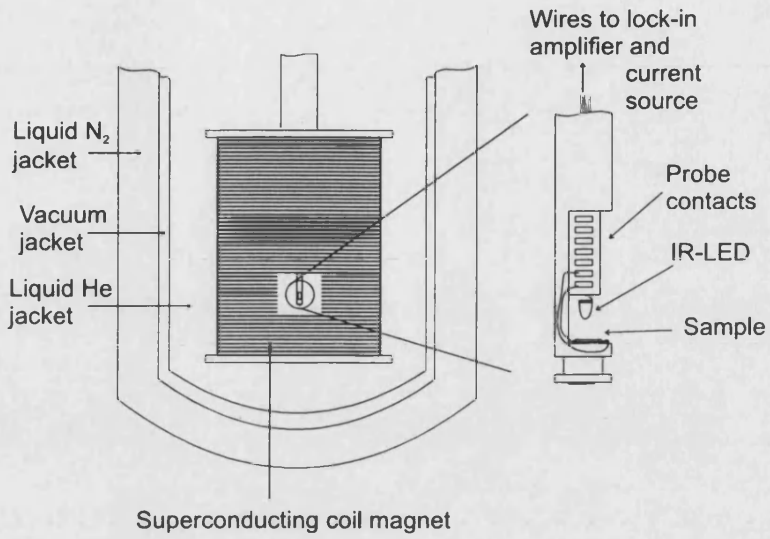

Figure 2.5: The lower part of the liquid helium cryostat used in the 4.2K experiments, incorporating a superconducting (niobium) wire magnet. Inset shows the sample probe with an infra-red LED vertically above the sample.

range. A superconducting magnet capable of providing fields in excess of 15T was incorporated into the system.

2.4.2 Resistance measurements

Resistance measurements can be performed on the basis of either a two- or a four-terminal technique. In the two-terminal technique, most commonly used in hand-held multimeters, current is passed between two probes over which the voltage drop is measured. On the other hand, in the four-terminal technique the voltage drop is measured over two contact probes independent of the probes through which current is passed. Therefore, in a four-terminal measurement, the amount of contact resistance detected is reduced, making this a superior technique.

The four-terminal resistance measurements can be classified as being local or non-local. A local measurement is made by measuring the voltage drop between two probes positioned between two current probes, usually situated at the extremities of the active region. In a non-local measurement, voltage probes are situated away from the current probes, thus allowing an indirect study of the effects of

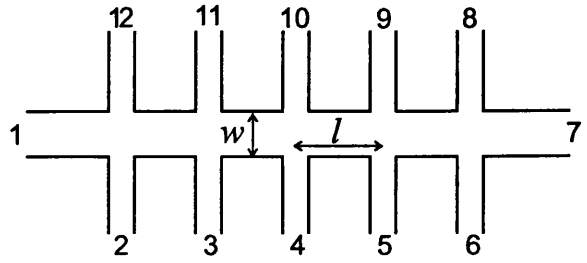

Figure 2.6: Typical probe arrangement of a device. The numbering is used to explain the measurement configuration of the different techniques implemented.

the current.

In this work, resistance measurements were performed on the basis of the four terminal alternating-current technique. Current oscillating at 30Hz, was applied to the sample by dropping 0.5V from an ac voltage source, built into a lock-in amplifier, across a large resistor. Large resistance (5MΩ) was used in order to minimise the effect of the variations of the device resistance (Ω-kΩ range) on the current. Referring to figure 2.6, current was applied between probe pair (1-7) (probe 7 was the ground contact), and the voltage drop was measured between probes (11-10) and (10-4) in the longitudinal and transverse cases respectively. The lock-in amplifier was used because of the ability to lock onto a signal of a particular frequency, and the resistance measurements were performed by locking onto the 30Hz signal.

Bend resistance, a non-local measurement, was studied by passing current through probe pair (1-10) and detecting the drop between probe pair (4-7). The advantage of this technique is that it is very sensitive to the inhomogeneities present in the area across which the measurement is made (the Hall cross in this case). The voltage drop was detected at the frequency of the oscillating current (30Hz).

2.4.3 Thermopower measurements

Thermopower measurements, both phonon-drag and diffusion, cannot be classed as either two- or four-terminal because the current is used only to induce temperature gradients by the Joule heating technique. Use of low frequency currents for this purpose is an established technique [15], since in that regime, the induced

temperature gradient oscillates at the same frequency.

The heating line was established by passing a $f_{th} = 7$Hz oscillating heating current between probe pair (12-2). In the case of diffusion measurements, low heating currents were applied to the sample ($\sim 0.2\mu A$) so that only the electron system was heated. Measurement of phonon-drag thermopower required excitation of the phonon system, consequently larger heating currents were used. The best results were obtained in the range $700 - 2000\mu A$. The voltage drop in phonon-drag and diffusion case, known as thermovoltage, was measured at double the excitation frequency ($2f = 14$Hz). The reason for this is that thermopower (thermovoltage) is proportional to Joule power dissipated, and if the excitation current oscillates at *f*, the power component oscillates at *2f*. Probe pairs for longitudinal thermovoltage were along the same side of the Hall bar (same as in longitudinal resistance measurement), and for transverse on opposite side of the bar (as in transverse resistance case).

Chapter 3

Magnetic field dependence of phonon-drag thermopower

3.1 Introduction

This chapter contains the experimental and theoretical results obtained in the study of phonon-drag thermopower of unmodulated and periodically modulated two-dimensional electron gases. A theory, based on the modified Boltzmann equation and developed in order to explain the observed experimental features, is explained here.

3.2 Background, motivation and phonon-drag thermopower

The magnetoresistance and diffusion thermopower are two kinetic coefficients studied extensively in mesoscopic systems. Early work in this field, particularly that of Weiss *et al.* [7] on the magnetoresistance of periodically modulated two-dimensional electron gases, sparked an extreme interest in the transport properties of modulated systems, both in the theoretical [9, 16, 17, 18, 19, 20] and experimental domains [8, 21, 22, 23, 24, 25, 26, 27]. Another kinetic coefficient,

until recently largely ignored in the studies of electronic properties of modulated systems, contains a lot of physical information and is the subject of the present chapter.

The existence of phonon-drag thermopower was theoretically proposed by Conyers Herring [28] in an attempt to explain the experimental results of thermopower measurements of germanium at low temperature. Frederikse [29] and Geballe and Hull [30] observed large deviations which could not be explained by assuming the sole contribution to thermopower was the diffusion of electrons. Herring proposed that the enhancement in thermoelectric power (TEP) was due to the coupling between electrons and phonons in which momentum from the phonon system is passed onto the electron system.

The aim of the work presented here was to experimentally and theoretically investigate phonon-drag thermopower in a 2DEG subject to a periodic electrostatic potential. The presence of a superlattice potential on top of a two-dimensional electron gas leads to quasi-classical resonance between the classical cyclotron diameter and an integral number of periods of the superlattice. These resonances give rise to commensurability oscillations in magnetoresistance and diffusion thermopower, and similar observations were expected to be made in phonon-drag. Since the period of the superlattice (500 and 1000nm) is larger than the wavelength of an electron (typically 50nm), the interference of electron waves could be ignored, thus simplifying the analysis of results.

In the next section, a brief theoretical overview of thermopower is given. This is followed by the results of phonon-drag measurements in unmodulated 2DEGs.

Thermopower

In general, thermoelectric power (TEP) is defined as the proportionality factor S between a temperature gradient ∇T applied to a conductor, and the resulting electric field,

$$\mathbf{E} = S\nabla\mathbf{T}. \tag{3.1}$$

Under the influence of an electric field and a temperature gradient, the thermoelectric transport is defined by the electrical current density,

$$\mathbf{J} = \sigma\mathbf{E} - \epsilon\nabla\mathbf{T}, \tag{3.2}$$

where σ is the electrical conductivity and ϵ is the thermoelectric tensor. Thermopower is measured without the application of an external current, $\mathbf{J}$=0, to the conductor, therefore it is possible to reduce equation 3.2 to $\sigma\mathbf{E} = \epsilon\nabla\mathbf{T}$. Combining this with equation 3.1 gives the expression for TEP in terms of conductivity and thermoelectric tensor,

$$S = \sigma^{-1}\epsilon. \tag{3.3}$$

In the presence of a finite external magnetic field applied in a direction perpendicular to the direction of the temperature gradient, the thermoelectric power coefficient is a tensor with independent longitudinal (S_{xx}) and transverse (S_{xy}) components given by

$$\begin{aligned} S_{xx} &= \rho_{xx}\epsilon_{xx} + \rho_{xy}\epsilon_{yx}, \\ S_{xy} &= \rho_{xx}\epsilon_{xy} + \rho_{xy}\epsilon_{yy}. \end{aligned} \tag{3.4}$$

Longitudinal component is parallel to the direction of the temperature gradient, while the transverse component (Nernst-Ettingshausen coefficient) is in the direction perpendicular to the gradient. The components of resistivity are given by the tensor of equation 3.5 with $\rho = m/(n_s e^2 \tau_{ei})$ the usual Drude resistivity term.

$$\rho = \rho \begin{bmatrix} 1 & \omega_c\tau_{ei} \\ -\omega_c\tau_{ei} & 1 \end{bmatrix} \tag{3.5}$$

In the limit of weak electron-phonon interaction, two distinct processes – diffusion

(S^d) and phonon-drag (S^g) – contribute to the total thermopower of the system, $S = S^d + S^g$. Diffusion thermopower is the subject of the following chapter, therefore, only phonon-drag will be discussed here.

Phonon-drag thermopower quantifies the coupling between electron and phonon systems. Intuitively, one may expect that phonon-flow from hotter to colder regions is induced in a conductor to which a sufficiently large temperature gradient ∇T is applied. Associated with such flow is a momentum current proportional to $-\Lambda\nabla T$, where Λ is the phonon mean free path. Following electron-phonon collisions, a fraction of this momentum is transferred to the electron system at a rate proportional to τ_{ep}^{-1}, where τ_{ep} is the electron-phonon scattering time. As a result of the collision, electrons start moving in the direction of scatter, giving rise to an electric current $\mathbf{j_{th}}$, referred to as the thermoelectric current. Since electrons also suffer collisions with impurities, the acquired momentum is retained by electrons for a time τ_{ei}, the electron-impurity scattering time. Assuming that $\tau_{ei} \ll \tau_{ep}$, it can be seen that the momentum is quickly randomised.

$$\mathbf{j_{th}} \propto \frac{1}{\tau_{ep}} \tau_{ei} \Lambda \nabla T. \tag{3.6}$$

Since thermopower is measured when the total current is zero, the existence of a thermoelectric current $\mathbf{j_{th}}$ suggests the existence of a compensating current with the same magnitude but an opposite sign. This drift current is the result of a compensating electric field $\mathbf{E}$, and is given as

$$\mathbf{j_E} = \sigma \mathbf{E}. \tag{3.7}$$

The compensating field is proportional to $-\Lambda\nabla T\tau_{ep}^{-1}$, and since $\mathbf{E} = S\nabla\mathbf{T}$, it can be seen that S^g is proportional to $-\Lambda/\tau_{ep}$. In the case of 3D non-degenerate semiconductors, S^g is given by

$$S^g = -\frac{\Lambda v}{\mu_{ph} T}, \tag{3.8}$$

where v is the sound velocity, μ_{ep} the phonon-limited electron mobility $\mu_{ph} =$

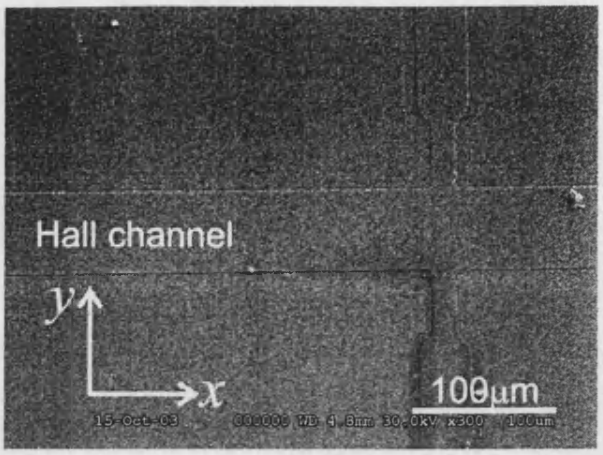

Figure 3.1: Electron micrograph of a part of a Hall bar used in the measurements of phonon-drag thermopower of unmodulated 2DEGs.

$(e\tau_{ep}/m_{eff})$ with m_{eff} the effective mass of an electron. To a good approximation, equation 3.8 can also be used to calculate the phonon-drag thermopower of a 2DEG [31, 32] at zero-magnetic field.

A closer examination of equation 3.8 reveals that phonon-drag thermopower is independent of electron-impurity scattering which is a determining factor in resistance. This is due to the fact that conductivity is a function of τ_{ei}, and by combining $\mathbf{j_E}$ and $\mathbf{j_{th}}$ terms, τ_{ei} dependence cancels out. Clearly, phonon-drag is a powerful tool in the study of coupling between electron and phonon systems, however, electron-phonon scattering is a minor event for both electron and phonon systems at low temperatures and carrier densities. Therefore, experimental detection of S^g is not a trivial exercise.

3.3 Phonon-drag thermopower of unmodulated 2DEGs

This section presents results of systematic measurements of longitudinal and transverse components of phonon-drag thermopower of unmodulated 2DEGs. The measurements were performed at 4.2K using samples with outline shown in figure 2.1a (without the grating). Figure 3.1 shows an electron micrograph of one sample.

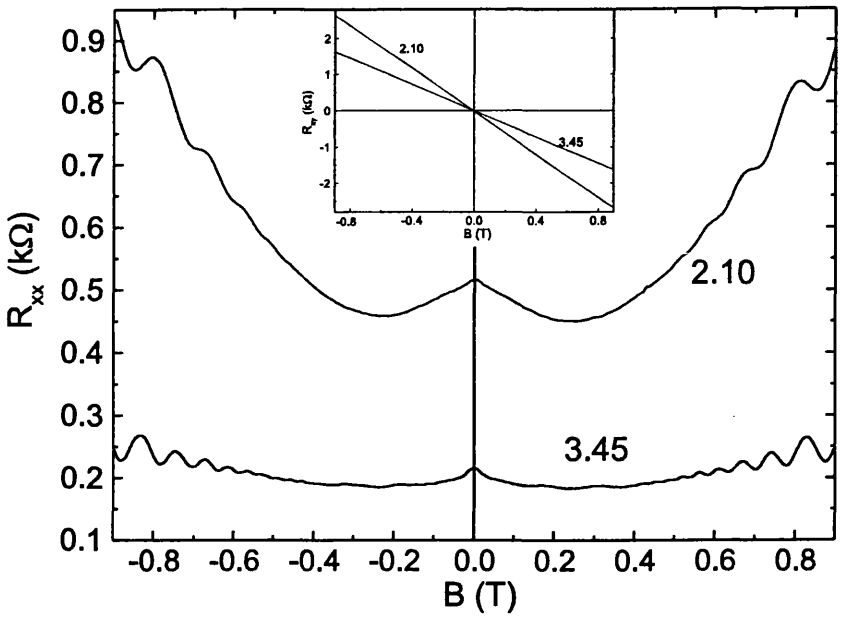

Figure 3.2: Longitudinal resistance, R_{xx}, measured as a function of the magnetic field B applied perpendicularly to the film of electrons. The top curve was measured at electron density, $n_s = 2.10 \times 10^{15}\text{m}^{-2}$, and the bottom at $n_s = 3.45 \times 10^{15}\text{m}^{-2}$. The inset shows Hall resistance measured at the same n_s.

3.3.1 Experiment

In addition to phonon-drag measurements, complimentary measurements of longitudinal and Hall resistance were performed. Figure 3.2 shows the longitudinal resistance measured at two different values of electron density, n_s, as a function of magnetic field B perpendicular to the plane of the 2DEG. The electron density was varied in the Hall bar by infra-red illumination, and was $2.10 \times 10^{15}\text{m}^{-2}$ in the dark (top curve) and $3.45 \times 10^{15}\text{m}^{-2}$ after illumination (bottom curve). Electron density values were extracted from Shubnikov de-Haas oscillations observed at $B > 0.6$T.

The peak in R_{xx} observed around zero-field was due to weak-localisation [33, 34]. Weak localisation is the increase in longitudinal resistivity ρ_{xx} ($\propto R_{xx}$) due to the backscattering of clockwise and anticlockwise electron paths. One way in which weak localisation can be destroyed is by raising the temperature which increases the frequency of phase-randomising inelastic collisions. In the experiments considered here, weak localisation was removed by applying magnetic

field whose time-reversal symmetry destroys the interference between clockwise and anticlockwise paths.

Following the weak-localisation peak, both resistance sweeps of figure 3.2 showed positive magnetoresistance and the onset of the quantum mechanical regime ($\omega_c\tau_{ei} > 1$) indicated by the presence of Shubnikov de-Haas (SdH) oscillations. At higher electron density, where the electron mobility is high, SdH oscillations appeared at lower B. The symmetry of the curves around zero-field line indicated homogenous electron distribution within the 2DEG. Hall resistance curves showed expected linear behaviour (inset to figure 3.2).

Figure 3.3 shows longitudinal thermovoltage (U_{xx}) measured at $n_s = 3.41 \times 10^{15}\text{m}^{-2}$, with applied heating currents in the range 0.33 to 0.67mA. It immediately becomes apparent that U_{xx} is magnetic field independent in the classical regime ($\omega_c\tau_{ei} < 1$), with field dependence emerging in the quantum regime ($\omega_c\tau_{ei} > 1$). Field dependence was reflected by the oscillatory thermovoltage which arose due to the quantisation of energy into Landau levels.

An increase in zero-field U_{xx} with increasing heating current was observed (inset to figure 3.3), and was measured as 0.09μV for $I_h = 0.33$mA, and $0.35\mu V$ for $I_h = 0.67$mA. As the inset also shows, detection of such small voltages led to the pick-up of an unwanted noise component. Using the dependence of zero-field thermovoltage on heating current, zero-field thermopower was calculated. Since thermopower is defined as the ratio of voltage drop to temperature drop between two contacts, a way of calculating the temperature drop from I_h was required. The starting point was to define ΔT_L as the increase in the lattice temperature at the heating line. It was calculated by assuming that all Joule dissipation sinks in the lattice through the volume occupied by the 2DEG in the Hall cross,

$$\Delta T_L = \frac{P_h \tau_{ep}}{C_p \rho_d V}. \tag{3.9}$$

The heating power, P_h was given through $P_h = I_h^2 R$, where $R = \rho(l/w)$ is the resistance of the active region of the Hall cross (l and w the widths of the Hall channel and probe channel, respectively). The heat capacity C_p and density ρ_d of GaAs were taken as $0.335 J/g\ deg$ and $5.36 gcm^{-3}$, respectively. The volume of the 2DEG, V, was calculated by assuming a finite thickness of the 2DEG layer

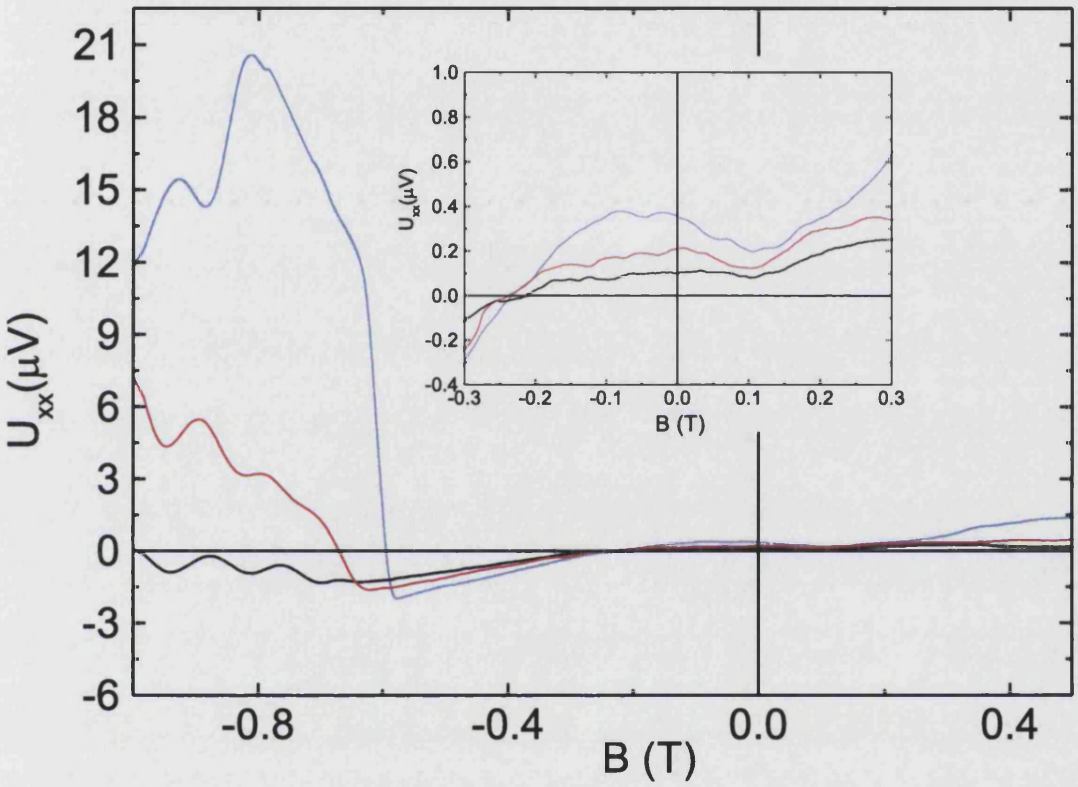

Figure 3.3: Longitudinal thermovoltage measured in unmodulated two-dimensional electron gas sample at $n_s = 3.41 \times 10^{15} m^{-2}$ and with $I_h = 0.33$mA (black curve), 0.47mA (red curve) and 0.67mA (blue curve). U_{xx} is finite and field independent in the classical limit ($\omega_c \tau_{ei} < 1$), and field dependent in the quantum limit ($\omega_c \tau_{ei} > 1$). The inset shows an increase in the value of U_{xx} with increasing I_h.

(10nm).

To calculate the increase in lattice temperature at the Hall cross 1000μm away from the heater (probe pair (11-3) in figure 2.6, assuming probe pair (12-2) is used as the heater), U_{xx} was measured between contacts 1000 and 2000μm away from it (probe pairs (11-10) and (10-9), respectively). The voltage drop was seen to fall by a factor of 10, and assuming exponential decay, increase in lattice temperature at (11-3) was estimated as $\Delta T_L/10$. Using this value, zero-field thermopower was calculated as $101\mu V/K$, comparable to the theoretical estimate $S^g = (\Lambda v)/(\mu_{ep}T) \sim 150\mu V/K$.

As figure 3.4 shows, the Nernst-Ettinghausen coefficient is also independent of magnetic field in the classical limit. Unlike in the longitudinal case, however, transverse thermovoltage did not exhibit linear dependence on heating power. Moreover, the zero-field value became more negative with increasing power, therefore, an accurate value of $S_{xy}(B = 0)$ could not be extracted from the data.

In the quantum limit, $\omega_c\tau_{ei} > 1$, the U_{xy} component also exhibited field dependent behaviour. The precise mechanism for the observed oscillations is not known, however, the onset of such behaviour was observed at the same magnetic field as in longitudinal magnetoresistance and magnetothermopower cases.

3.3.2 Theory

The experiments just reported were performed on highly degenerate 2DEGs in which electrons occupied a single subband. Miele *et al.* [35] considered such a system and derived the expression for phonon-drag thermopower in the classical limit, based on the Boltzmann equation. The main points of that work are given here.

In a system in which both impurity and phonon scattering effects are important, and which is subject to static electric and magnetic fields, the electron distribution function $f_k(\mathbf{r})$ is given by the solution of equation 3.10.

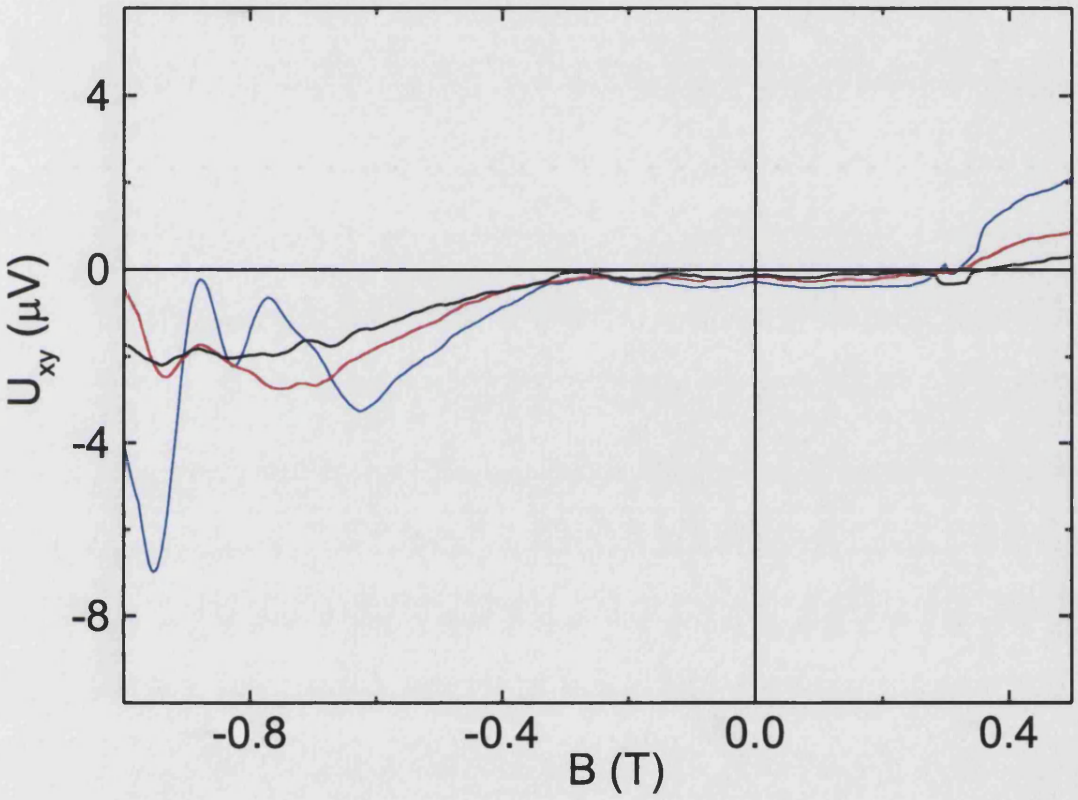

Figure 3.4: Transverse thermovoltage (Nernst-Ettinghausen coefficient) measured in unmodulated two-dimensional electron gas sample at $n_s = 3.41 \times 10^{15}\mathrm{m}^{-2}$ and with $I_h = 0.33\mathrm{mA}$ (black curve), 0.47mA (red curve) and 0.67mA(blue curve). In the classical limit $\omega_c \tau_{ei} < 1$, U_{xy} is field independent.

$$\mathbf{v_k}.\nabla f_k - \frac{e}{\hbar}(\mathbf{E} + \mathbf{v_k} \times \mathbf{B}).\nabla_k f_k = \frac{\partial f_k}{\partial t}\bigg|_{imp} + \frac{\partial f_k}{\partial t}\,|_{ph} \tag{3.10}$$

Equation 3.10 is a steady-state Boltzmann equation, and the term which governs the scattering of electrons by impurities is equivalent to equation 1.4. If an incoming electron with a wavevector $\mathbf{k}$ is scattered by a phonon with wavevector $\mathbf{q}$, the resultant electron wavevector is $\mathbf{k}'$, where $\mathbf{k}' = \mathbf{k} + \mathbf{q}$. The rate at which electron distribution changes as a result of phonon scattering is given by

$$\frac{\partial f_k}{\partial t}\bigg|_{ph} = \sum_{k'}[f_{k'}(1 - f_k)P_{k',k} - f_k(1 - f_{k'})P_{k,k'}]\,. \tag{3.11}$$

The probability of an electron being scattered from state $\mathbf{k}$ to state $\mathbf{k}'$ is given by the usual Fermi Golden Rule expression

$$P_{k,k'} = \frac{2\pi}{\hbar}\sum_{Q}|M_{k,k'}(Q)|^2\left[N_Q\delta(\epsilon_{k'} - \epsilon_k - \hbar\omega_Q) + (N_{-Q} + 1)\delta(\epsilon_{k'} - \epsilon_k + \hbar\omega_Q))\right], \tag{3.12}$$

where Q is phonon wave-vector representing the parallel and perpendicular components of 3-D vector $\mathbf{Q}$ to the 2DEG ($Q_{\|}$ and $Q_{\perp}$, respectively). In order to determine the detailed form of the electron-phonon matrix element, $M_{k,k'}$, the acoustic phonon deformation potential and the piezoelectric interactions in GaAs/AlGaAs must be known. Assuming that the non-equilibrium phonon occupation number is N_Q, then the first term in the square brackets on the right hand side of equation 3.12 corresponds to the absorption of a phonon by the electron system, whereas the second term corresponds to phonon emission from the system.

The solution of equation 3.10 is given by Cantrell and Butcher [36] and Miele [35] as

$$f_k(\mathbf{r}) = f_k^{le}(T(\mathbf{r}), \mu(\mathbf{r})) - \frac{\partial f_k^0}{\partial \epsilon_k}\Phi_k, \tag{3.13}$$

where f_k^0 is the equilibrium electron distribution at a temperature T and chemical potential μ, f_k^{le} is the local equilibrium distribution of electrons, ε_k is the energy and $\frac{\partial f_k^0}{\partial \varepsilon_k}\Phi_k = f_k(1 - f_{k'})$.

In order to investigate the coupling between electron and phonon systems, knowledge of the phonon distribution is also required. The steady state Boltzmann equation for phonons has a similar form as equation 3.10, with the f_k term replaced by N_Q. The total rate of change of phonon distribution is the sum of the drift and collision terms. Assuming the equilibrium distribution is given by the Bose-Einstein statistics expression, $N_Q^0 = (e^{\beta\hbar\omega_Q} - 1)^{-1}$, the solution of the Boltzmann equation for phonons is

$$N_Q = N_Q^{le} - \frac{\partial N_Q^0}{\partial(\hbar\omega_Q)} G_Q, \tag{3.14}$$

where N_Q^{le} is the local equilibrium distribution of phonons and G_Q is the phonon non-equilibrium distribution. Now that both phonon and electron distribution functions are known, substituting 3.13 and 3.14 into equation 3.10 gives the linearised Boltzmann equation as shown in 3.15.

$$\mathbf{v_k}.\nabla T \frac{\partial f_k^0}{\partial T} - e\mathbf{v_k}.\mathbf{E}' \frac{\partial f_k^0}{\partial \varepsilon_k} + \frac{e}{\hbar}\mathbf{v_k} \times \mathbf{B}.\nabla_k \Phi_k \frac{\partial f_k^0}{\partial \varepsilon_k} = \frac{\partial f_k}{\partial t}\bigg|_{imp} + \frac{\partial f_k}{\partial t}|_{ph} \tag{3.15}$$

In the equation above, $\mathbf{E}'$ is the effective electric field and can be thought of as the gradient of the electrochemical potential, $(\mathbf{E} + (\nabla\mu/e))$. Since it is only the scattering of electrons by phonons which contributes to phonon-drag thermopower, only the second term on the right hand side of equation 3.15 is considered now. There are two contributions to this term, $\partial f_k/\partial t|_{ph1}$ which represents the scattering of non-equilibrium electrons by the thermal distribution of phonons, and $\partial f_k/\partial t|_{ph2}$ which represents the acceleration of electrons due to collisions with non-equilibrium phonons. Since the first term returns the electrons to equilibrium, it is only the second term which contributes to phonon-drag thermopower. For completeness of the argument, the $\partial f_k/\partial t|_{ph1}$ term is responsible for the resistivity due to phonon scattering. If the phonon non-equilibrium distribution is

written as

$$G_Q = -\frac{\hbar\omega_Q}{T}\tau_{ph}\mathbf{v}_{ph}(Q).\nabla T, \tag{3.16}$$

where $\mathbf{v}_{ph}(Q)$ is the phonon velocity and τ_{ph} is the phonon relaxation time, then the term driving the electrons from equilibrium due to phonon collisions is

$$\partial f_k/\partial t\Big|_{ph2} = \sum_{k',Q} G(Q)[\Gamma_{kk'}(Q) - \Gamma_{k'k}(Q)]\,. \tag{3.17}$$

Terms $\Gamma_{kk'}(Q)$ and $\Gamma_{k'k}(Q)$ are the scattering rates given by the Fermi Golden Rule approach. After some algebra [35], equation 3.17 can be written as

$$\frac{\partial f_k}{\partial t}\Big|_{ph2} = \frac{\partial f_k^0}{\partial \varepsilon_k}\sum_{\lambda}\frac{m^* s_\lambda \Lambda_\lambda}{\tau_{ep}^{\lambda}(\varepsilon)}\mathbf{v_k}.\frac{\nabla T}{T}\,. \tag{3.18}$$

In equation 3.18, the sum is over the polarisation index λ of the phonon mean free path Λ_λ and the sound velocity s_λ.

Since an applied temperature gradient gives rise to an electric field ($\mathbf{E} \propto \nabla\mathbf{T}$), the effect on the non-equilibrium electron distribution is exactly the same as the effect of an actual field $\mathbf{E}'$. Equation 3.6 showed that in the case of 3D non-degenerate semiconductors, phonon-drag contribution to current density was proportional to ∇T, which is also true in the 2DEG case. By defining a phonon-drag field $\mathbf{E_{ph}}$,

$$\mathbf{E_{ph}}(\varepsilon) = \sum_{\lambda}\frac{m^* s_\lambda \Lambda_\lambda}{e\tau_{ep}^{\lambda}(\varepsilon)}\frac{\nabla\mathbf{T}}{T}, \tag{3.19}$$

the phonon-drag contribution is given by the energy average of the phonon-drag field, $\mathbf{J}_{ph} = \sigma(B) < \mathbf{E}_{ph} >$. Since impurity conductivity at low magnetic fields depends weakly on energy, this dependence was neglected. Combining the expression for $\mathbf{J}_{ph}$ with equation 3.19, and remembering that $\sigma(B) < \mathbf{E}_{ph} >= -\varepsilon^{\mathbf{g}}\nabla T$, the thermoelectric tensor is defined as

$$\epsilon^{g}(B) = -\sum_{\lambda} \frac{m^* s_\lambda \Lambda_\lambda}{eT} < \frac{1}{\tau_{ep}^{\lambda}} > \sigma(B). \tag{3.20}$$

Mathematically, phonon-drag thermopower is defined as $S^g(B) = \sigma^{-1}\epsilon^{g}(B)$, and by combining this with equation 4.11, the extended form of phonon-drag thermopower is given as

$$S^g = -\sum_{\lambda} \frac{m^* s_\lambda \Lambda_\lambda}{eT} < \frac{1}{\tau_{ep}^{\lambda}} > . \tag{3.21}$$

The magnetic field dependence of the phonon-drag tensor arises from the field dependence of the conductivity tensor. However, the thermoelectric tensor is also proportional to $\sigma(\mathbf{B})$, and combining expressions 3.20 and 3.3, the conductivity tensors cancel. This means that the phonon-drag thermopower is given by equation 3.21 with no dependence on magnetic field, i.e. $\mathbf{S}^{g}(B) = S^{g,0}\mathbf{I}$. Furthermore, phonon-drag is a diagonal tensor given by

$$\mathbf{S}^{g} = \begin{bmatrix} S^{g,0} & 0 \\ 0 & S^{g,0} \end{bmatrix}. \tag{3.22}$$

In terms of experimentally measurable quantities, expression 3.22 suggests that the longitudinal phonon-drag thermopower is finite and independent of magnetic field, at least in the low-field regime where $\omega_c \tau_{ei} < 1$. The transverse, (Nernst-Ettingshausen) coefficient should be zero and independent of the field. This is precisely what was observed in the case of longitudinal thermovoltage (figure 3.3). The transverse component, however, was not zero, and a probable reason for that is the superposition of electrical noise onto the measured thermopower signal. Nevertheless, there is good agreement between the theoretical prediction and the experimental results.

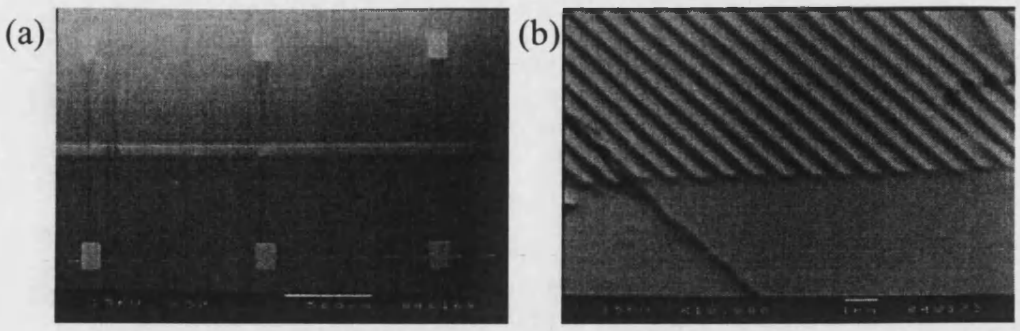

Figure 3.5: Electron micrographs showing (a) three Hall crosses and (b) the detail of the 1000nm period dysprosium superlattice.

3.4 Phonon-drag thermopower of periodically modulated 2DEGs

Intuitively, one may reasonably expect that a one-dimensional superlattice potential, applied to a system such as a 2DEG, will give rise to anisotropic effects. However, since resistance and diffusion thermopower tensors are isotropic around zero-field, they are inadequate tools in the measurements of such anisotropy. Furthermore, as shown in the previous section, phonon-drag thermopower is independent of the magnetic field in unmodulated 2DEGs, and the question remains whether commensurability effects might be observed when a periodic potential is applied.

In order to allow a definitive comparison of results, devices used in the experimental work described in this section were fabricated from the same GaAs/AlGaAs wafer as the devices used in measurement of phonon-drag in unmodulated 2DEGs.

Both longitudinal and transverse magnetoresistance components in superlattice samples have been investigated previously, particularly by Ye *et al.* [22] who also fabricated the superlattice from dysprosium. Figure 3.5 shows electron micrographs of the devices used in this experiment. Part (*a*) shows the three Hall crosses of the sample and part (*b*) shows the detail of the 1000nm period grating.

Longitudinal resistance was measured by passing 0.1μA excitation current (oscillating at 30Hz) through the Hall bar. Commensurability (Weiss) oscillations in R_{xx} were observed to become more pronounced as the electron density was

increased incrementally by successive illuminations with an infra-red LED. In the case of 500nm period device, R_{xx} was measured in the range $n_s = 1.56 - 3.10 \times 10^{15}\text{m}^{-2}$, while in the 1000nm period device, the range was $n_s = 1.88 - 3.33 \times 10^{15}\text{m}^{-2}$. The oscillations observed in magnetoresistance arise because of the presence of two length scales in the system - the period of the superlattice, a, and the cyclotron radius of the electron in the presence of applied magnetic field, R_c. When the cyclotron diameter is equal to the integer multiple of period a, within a phase factor ϕ, the electron orbit begins to drift in the direction parallel to the superlattice. The drift of the orbit leads to an increase in diffusion in the direction parallel to the superlattice (δD) which results in the increase in resistivity in the direction perpendicular to the superlattice.

The condition for the appearance of commensurability oscillations, given by equation 3.23, was proposed by Weiss *et al.* [7], and a theoretical explanation of the effect was given by Gerhardts *et al.* [21], Winkler *et al.* [24] and Beenakker [9].

$$2R_c = 2\frac{\hbar k_F}{eB} = (\lambda + z)a \tag{3.23}$$

In equation 3.23, k_F is the Fermi wavevector, B is the externally applied magnetic field and e is the charge of the electron, and λ is the integer commensurability oscillation index. Figure 3.6 shows the longitudinal magnetoresistance of the 500nm period sample measured at various electron densities.

In the case of the sample with the wider period superlattice, commensurability oscillations were also observed to be more pronounced at higher electron densities. The reason for this is that an increase in electron density increased the mean free path of electrons ($l = v_F \tau_{ei}$). This meant that electrons were predominantly scattered by the superlattice potential.

Commensurability oscillations were analysed by plotting the oscillation index against the inverse magnetic field at which the oscillation minima were observed. The resulting graph has a fan-like appearance, with each branch corresponding to a different electron density, as shown in figure 3.7. The gradient of individual branches ($\hbar k_F/ea$) was found to be proportional to square root of the electron density, therefore knowledge of the period of the superlattice allowed the calculation of electron density. Intercept on the λ-axis determines the nature of

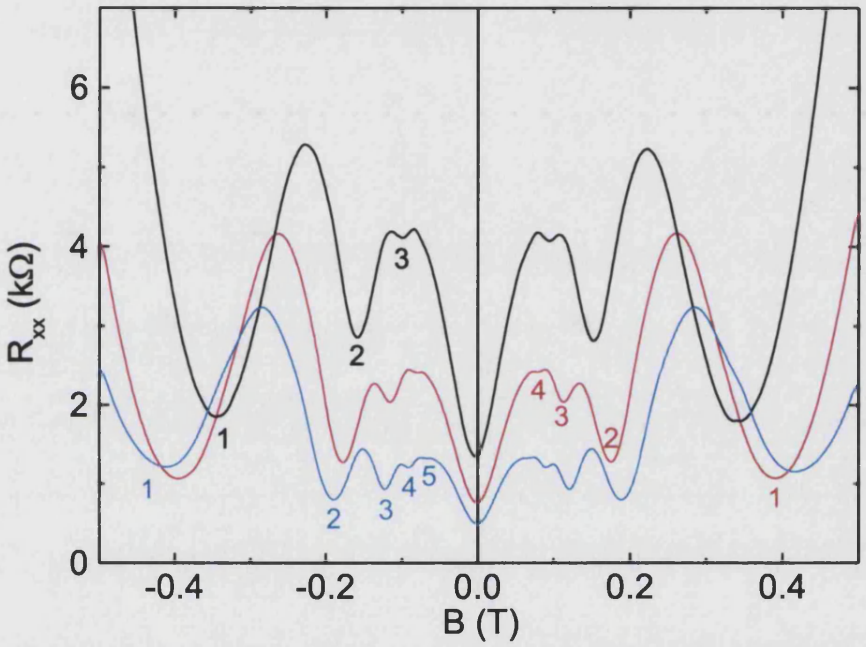

Figure 3.6: Longitudinal magnetoresistance of the 500nm period sample measured at $n_s = (1.49, 2.19, 3.10) \times 10^{15}\mathrm{m}^{-2}$ (top curve corresponds to lowest n_s and the bottom to highest). The commensurability oscillations, inversely periodic in B, became more pronounced as the density was increased. Values of λ at resistance minima are shown.

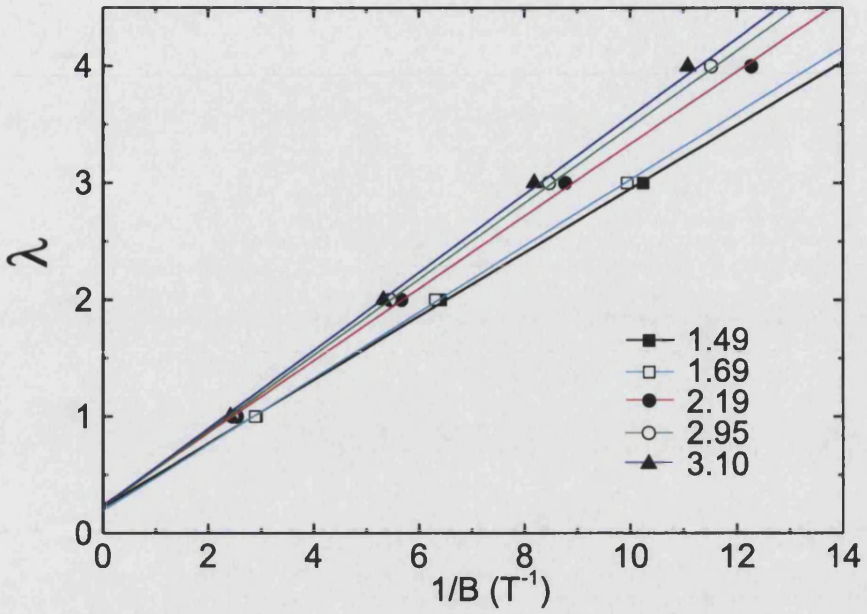

Figure 3.7: The oscillation index, λ, of minima in R_{xx} plotted as a function of 1/B for $n_s = (1.49, 1.69, 2.19, 2.95, 3.1) \times 10^{15}\mathrm{m}^{-2}$. Data was taken form the R_{xx} curves of figure 3.6. The intercept (+0.2), common to all lines, shows that the modulation is predominantly electrostatic.

modulation of the electron layer: electrostatic, magnetic or a mixture of the two. If the intercept is -0.25 (phase factor $z = 0.25$ in equation 3.23), the modulation is magnetic, and if the intercept is +0.25 ($z = -0.25$) the modulation is electrostatic.

As figure 3.7 shows, the intercept for the oscillations observed in the 500nm period device is +0.2 which suggests that the modulation was predominantly electrostatic. However, some mixing between electrostatic and magnetic modulation was occurring since intercept is not exactly +0.25. There were two possible reasons why electrostatic modulation was dominant. One is that dysprosium and GaAs have different thermal expansion coefficients, and the other is that dysprosium oxidises quickly if left exposed to air [37]. These two effects combined to give rise to piezoelectric strain between the two layers which clearly resulted in electrostatic modulation [38]. If the modulation had been magnetic, the only difference would have been the position of the minima in R_{xx} but the oscillations would still have been present.

The theoretical interpretation of the effects leading to the observation of com-

mensurability effects in longitudinal resistance was proposed by various groups. The quantum mechanical approach of Winkler, Kotthaus and Ploog [24] and Gerhardts, Weiss and Klitzing [21], although correct in the sense that it reproduced experimental observations, did not give any insight into the underlying physics. Winkler's group concluded that the oscillatory behaviour was a result of the formation of Landau bands in the 2DEG under the influence of the periodic potential. Similarly, Gerhardt's group concluded that the oscillatory dependence of the bandwidth of modulation-broadened Landau levels on the band index leads to an oscillating contribution to the conductivity tensor.

The semiclassical approach of Beenakker [9], based on the Boltzmann equation, gave the simplest explanation of the effect. Here a sinusoidal form ($V(x) = V_0 sin(2\pi x/a)$) of the periodic potential is considered, with the guiding centre (X,Y) of an electron orbit centered at the position (x, y). The velocity components of an electron at a point x,y are v_x in the direction perpendicular and v_y in the direction parallel to the superlattice. Since the superlattice potential is a function of x, the electric field in this direction is $E(x)$, and the time derivatives of the guiding centre are $dX/dt = 0$ and $dY/dt = E(x)/B$. This is the $E \times B$ drift and refers to the guiding centre motion which is parallel to the superlattice (parallel to the y-axis). No motion in the direction perpendicular to the superlattice (parallel to the x-axis) is induced. This situation is represented schematically in figure 3.8.

At low magnetic fields ($\omega_c \tau_{ei} < 1$), the cyclotron radius of an electron encompasses multiple periods of the superlattice ($R_c \gg a$), and the electric field oscillates rapidly under the orbit. However, the drift acquired by the guiding centre due to the field averages out at all points apart from at the points $X \pm R_c$ in figure 3.8. Depending on whether the field has the same or opposite sign at these two points, the orbit can be either resonant or non-resonant. If the orbit is resonant, the guiding centre acquires a drift in the direction parallel to the superlattice and an additional component to 1D diffusion, δD_{yy}, given by

$$\delta D_{yy} = \tau_{ei} < v_{drift}^2 >, \tag{3.24}$$

where v_{drift} is the drift velocity of the guiding centre. In the non-resonant case, the magnitude of the field at the two extremities is the same (different sign) and

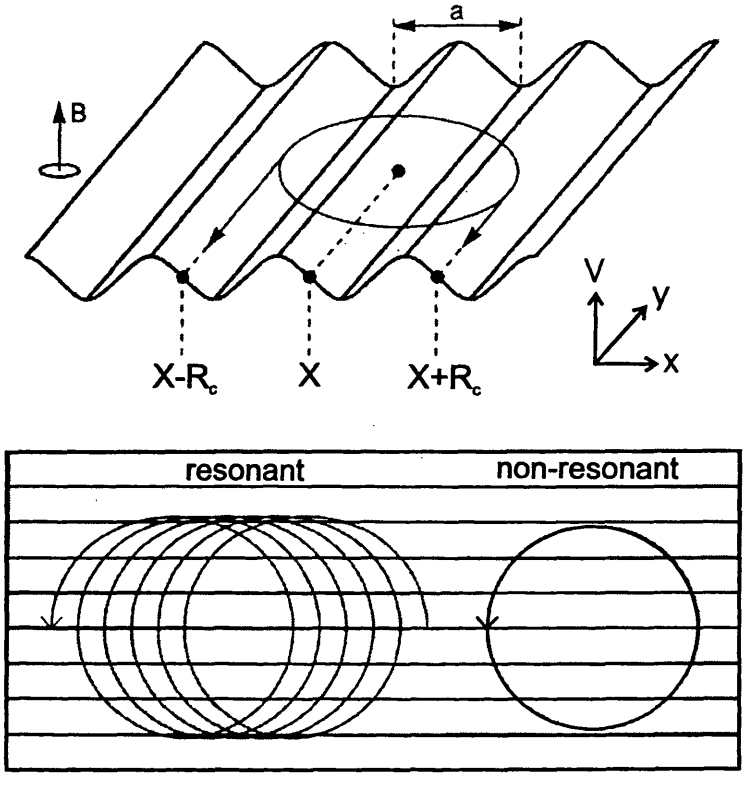

Figure 3.8: Sinusoidal form of the potential caused by the superlattice. The orbit superimposed on the potential moves parallel to the y-axis in the resonant case and does not drift in the non-resonant case. The lower part of the figure shows the resonant and non-resonant orbits superimposed on the equipotential lines (y-axis is parallel to the equipotential lines in this part of the figure). Taken from reference [9].

the electron orbit turns on itself (lower part of figure 3.8) Therefore, there is no drift of the guiding centre, although the orbit may be swept away by an electric field applied through the conductor.

The increase in diffusion parallel to the superlattice is added to the yy-element of the unperturbed diffusion tensor $\mathbf{D_0}$. Once $\mathbf{D_0}$ has been calculated, the resistivity tensor ρ can be obtained from the Einstein relation $\rho = \mathbf{D}^{-1}/e^2\rho(E_F)$, where $\rho(E_F)$ is the two-dimensional density of states. The yy enhancement in diffusion predominantly modifies the xx-component of resistivity, and equation used to calculate ρ_{xx} is given in equation 3.25.

$$\rho_{xx} = \frac{1+K}{2\sigma_1(1+K)} \tag{3.25}$$

In equation 3.25, K is given by

$$K = \frac{\eta^2(ql)}{2(1+(\omega_c\tau)^2)L}, \tag{3.26}$$

where $\eta = eV_0/E_F$, $q = 2\pi/a$ and l is the electron mean-free path. The correct solution of term L involves complex-order Bessel functions, however, since the Bessel functions are well approximated by their asymptotic expansion in the field range in which commensurability oscillations were observed ($|qR_c| \gg 1$), it was possible to simplify the calculation without making the result inaccurate. Equation 3.27 gives the correct and the approximate forms of L term.

$$L = \frac{2}{ql}\frac{\frac{sinh(\frac{\pi}{\omega_c\tau})}{(\frac{\pi}{\omega_c\tau})}}{J_{\frac{i}{\omega_c\tau}}(qR_c)J_{\frac{-i}{\omega_c\tau}}(qR_c)} \sim \frac{sinh(\frac{\pi}{\omega_c\tau})sgn(B)}{cos^2(|qR_c| - \frac{\pi}{4}) + sin^2(\frac{\pi}{2\omega_c\tau})} - \frac{2}{ql} \tag{3.27}$$

Equation 3.25 was solved with the starting conditions obtained from experimental data, and as figure 3.9 shows, agreement between the measured and calculated values of resistance is good. However, three points need to be raised here. Firstly, the theory does not account for the quantisation of energy into Landau levels, and therefore the calculated R_{xx} trace does not exhibit Shubnikov – de Haas oscillations which occur in the measured resistance at fields above |0.4|T. The

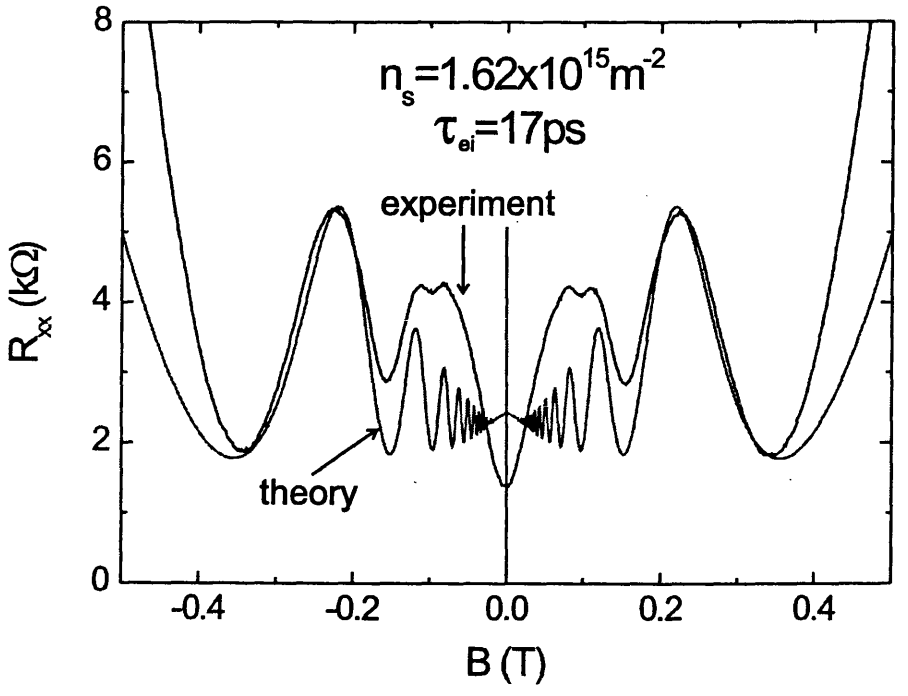

Figure 3.9: The calculated and measured curves showing the longitudinal resistance of a 500nm period device. The measurement was performed at $n_s = 1.62 \times 10^{15}\text{m}^{-2}$, the value used subsequently in the calculation of R_{xx}.

second and third points concern the low field regime in which the model fails to reproduce the exponential damping of commensurability oscillations caused by the finite mean free path [39], or the positive magnetoresistance due to the channelling of open orbits in the direction parallel to the wire.

Thermovoltage measurements in the modulated devices were carried out in the same manner as the ones in the unmodulated case. Figure 3.10 shows the dependence of thermovoltage measured at various heating powers for one value of electron density in 500nm period samples (similar was observed in 1000nm period sample). Immediately one striking feature of this figure becomes apparent: thermovoltage is **not** independent of magnetic field in the classical limit, unlike in the case of an unmodulated 2DEG.

In order to extract a value of zero-field phonon-drag thermopower, the dependence of U_{xx} on heating power was studied. Figure 3.10 shows the increase in zero-field longitudinal thermovoltage of the 500nm period device as the heating current (I_h) was increased. A plot of $ln(I_h)$ against $ln(U_{xx}(B = 0))$ easily verified that this increase was proportional to the square of the heating current, as expected.

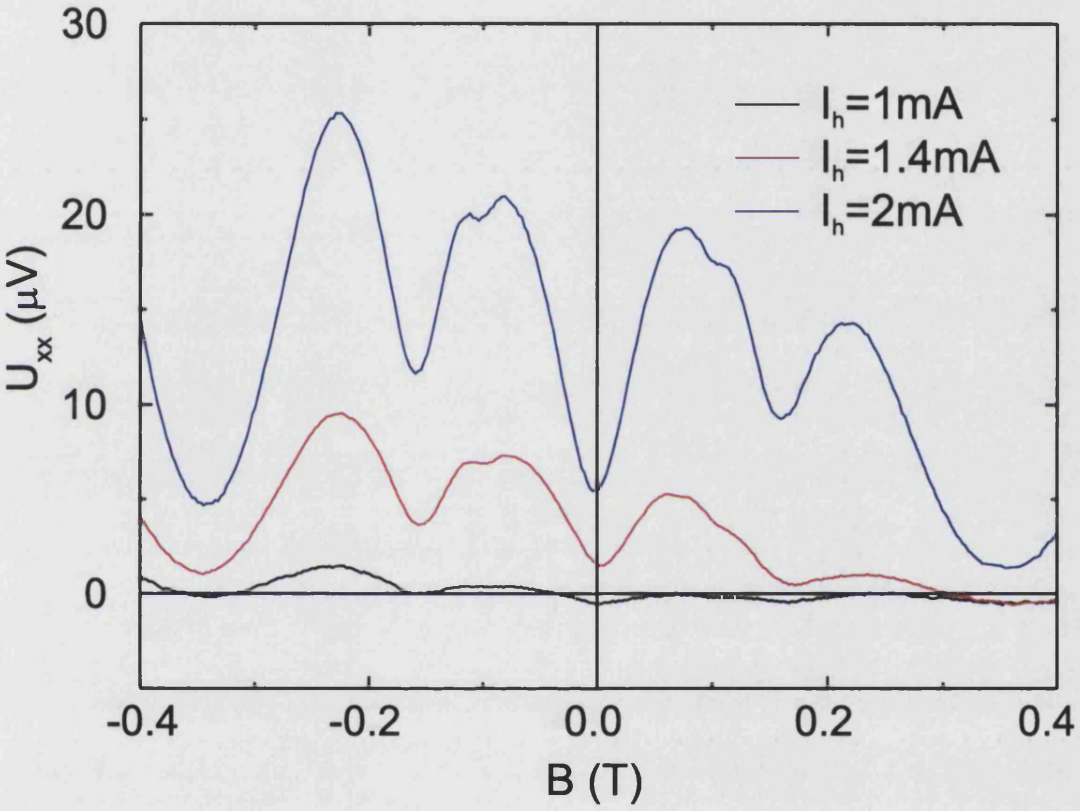

Figure 3.10: Thermovoltage of 500nm period sample at various heating currents measured at $n_s = 1.69 \times 10^{15}\mathrm{m}^{-2}$. The sweeps clearly show oscillations, which indicates that the thermovoltage is not independent of magnetic field.

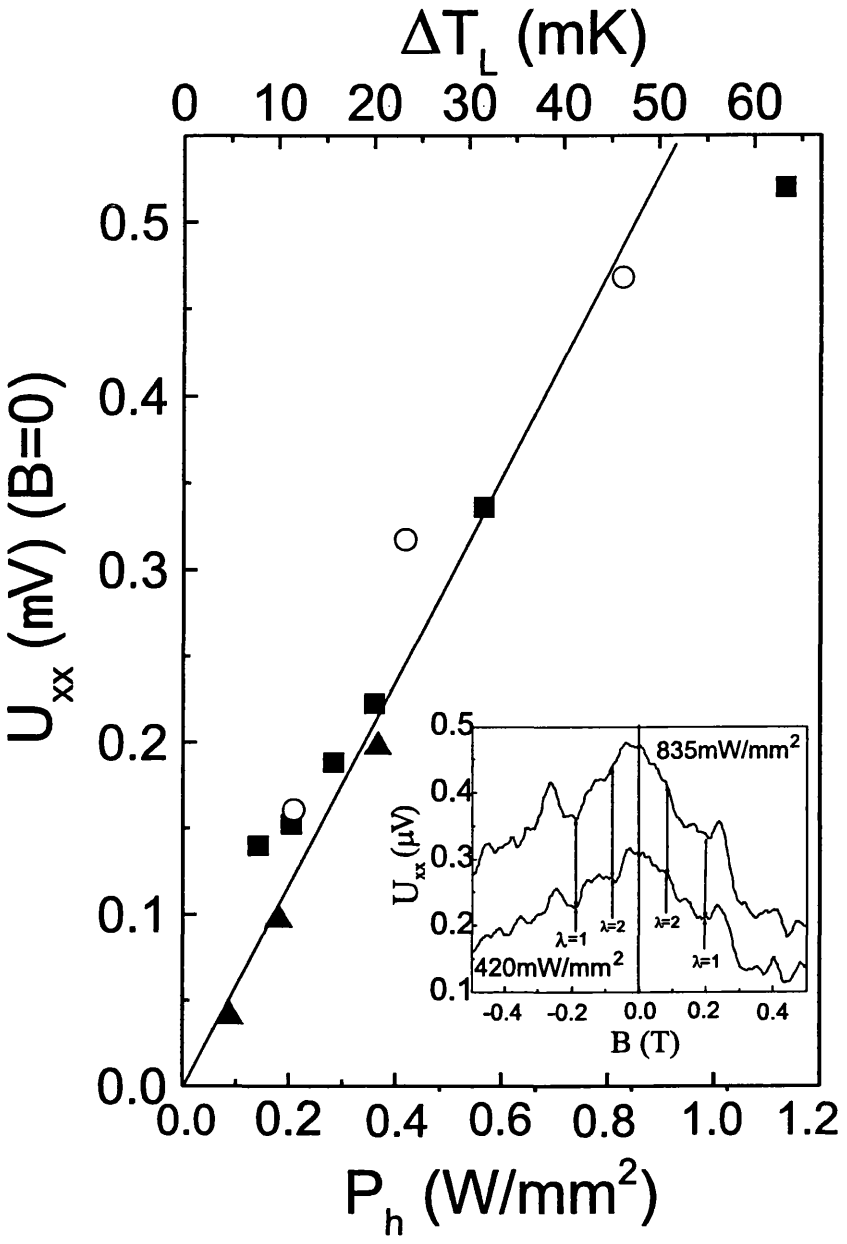

Figure 3.11: Dependence of zero-field thermovoltage of three separate devices on the Joule power dissipated per unit area of the heating line. Filled triangles correspond to 500nm period sample ($n_s = 1.49 \times 10^{15}\mathrm{m}^{-2}$), open circles to the same sample after scribing the 2DEG between heating node 2-8 and voltage node 3-7, and filled squares to the 1000nm period sample ($n_s = 1.9 \times 10^{15}\mathrm{m}^{-2}$). Inset shows that commensurability oscillations are still observed in two U_{xx} after scribing the Hall channel in 500nm period sample.

The gradient of the line in figure 3.11 was calculated as $S^g(B = 0) = 110 \pm 40\mu$V/K, which agrees well with the range of phonon-drag values, $S^g(B = 0) = 95 - 110\mu$V/K, published for similar 2DEGs [35, 40, 41], and 150μV/K calculated in the unmodulated 2DEG section. This result was also compared to the published values [40] of diffusion thermopower and it was found that it is about 10 times larger, certainly outside of the scope of experimental uncertainty, and thus proving that phonon-drag was the dominant component of thermopower measured.

The inset to figure 3.11 shows longitudinal voltage drop measured when the Hall channel between the heater node (2-12) was electrically insulated from the first voltage node (3-11) (refer to 2.6). Insulation was achieved by scribing the channel and allowed complete suppression of the contribution of electron diffusion to thermopower measurement. As it can be seen, U_{xx} still shows a dependence on magnetic field, furthermore, oscillations were observed at $B = 0.07$T ($\lambda = 2$), and $B = 0.19$T ($\lambda = 1$), roughly corresponding to field values at which oscillations were observed in longitudinal resistance (0.08 and 0.17T, respectively). The reason the oscillations were much more damped than in the uncut case is that the channel was cut using a diamond-tipped scriber. This method of electrically isolating the heater from the voltage probes not only suppressed electron flow but also attenuated the flow of surface phonon modes. Nevertheless, by completely eliminating the diffusion contribution to thermopower, the inset shows that the phonon-drag can be the only possible explanation for the observed commensurability oscillations.

There were two additional reasons which led to the conclusion that phonon-drag was the dominant contribution. The first of these was the design of the sample itself: the separation between the voltage probes (nodes) was 1000μm (two voltage probes were used as the heating node). Since the energy relaxation length l_{er} for electrons was evaluated from [42]

$$l_{er} = \pi\sqrt{\frac{\mu\tau_{ep}k_BT}{3e}}, \tag{3.28}$$

and was found to be $\sim 120\mu$m (assuming $\tau_{ep} \sim 10^{-9}s$ [43]), it immediately became apparent that thermally excited electrons were not reaching the voltage

probes. The second reason was the strength of the heating current applied to the heating line. This was always in the range $500 - 2000\mu$A, far larger than the heating current used in diffusion thermopower measurements previously [44, 45, 46], particularly in the work of Taboryski *et al.* [8], who used heating currents of $\sim 1\mu$A in their work on commensurability oscillations in diffusion thermopower.

The dependence of thermovoltage on electron density in the 2DEG was also investigated in 500 and 1000nm period devices. Although the resistance was measured in the field range $\pm$1T, the measurement of thermovoltage was restricted to the range $-0.45 \leq B \leq 0.45$T because of the increasing out-of phase voltage component detected outside of this range.

Figure 3.12 shows the dependence of thermovoltage oscillations in 500nm superlattice on electron density. As n_s was increased, the commensurability oscillations became more pronounced, and up to about 4 oscillation minima were seen for the highest densities investigated. Careful analysis shows that thermovoltage oscillations at low electron density are exactly in phase with resistance oscillations. This was additional proof that phonon-drag, and not diffusion, was measured here since Taboryski *et al.* [8] found a 90° phase shift between corresponding resistance and diffusion thermopower oscillations.

An interesting case occurred when n_s values were close to the saturation of the 2DEG. As the curve taken at $n_s = 1.7 \times 10^{15}\text{m}^{-2}$ shows, a small antisymmetric component in U_{xx} begins to develop around $B = 0$. At saturation density of the 2DEG ($n_s = 2.45 \times 10^{15}\text{m}^{-2}$), this component became large enough for U_{xx} to change phase by 180° around the zero-field line.

The phase change was accompanied by dramatic quenching of the zero-field value of U_{xx}. At the lowest n_s value, $U_{xx}(B = 0) = 23\mu$V, whereas at saturation, $U_{xx}(B = 0) \sim 0$. Although it is true that an increase in electron density decreased the resistance of the 2DEG and therefore reduced the heating power dissipated, leading to a smaller temperature gradient, this was not sufficient to explain the observed drop. Between the same values of electron density, the resistance traces show a drop in $R_{xx}(B = 0)$ of only about 1/3 ($R_{xx}(n_s = 1.3) = 2600\Omega$ and $R_{xx}(n_s = 2.45) = 430\Omega$). Therefore such a large drop in the $U_{xx}(B = 0)$ value must be attributed to the decrease in the phonon-drag thermopower (PDTP) with increasing electron density. The robustness of the phase changing behaviour was

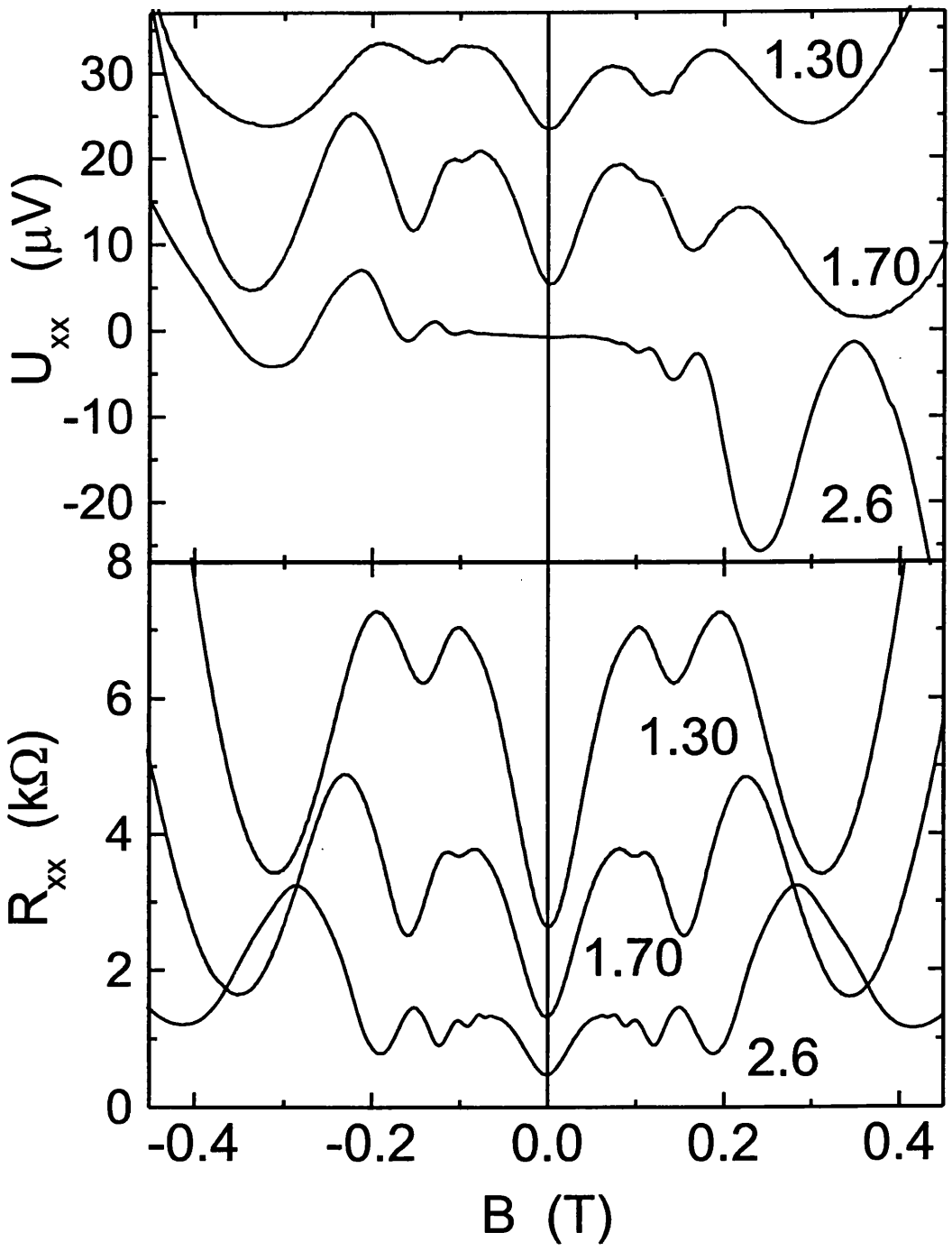

Figure 3.12: Longitudinal thermovoltage and resistance measured in 500nm period sample at three values of electron density shown ($\times 10^{15}\mathrm{m}^{-2}$). At the lowest n_s value, the thermopower commensurability oscillations (TCOs) are exactly in phase with resistance commensurability oscillations (RCOs). As the density was increased, small antisymmetrical component develops and at the saturation density becomes large enough that the phase of thermopower oscillations changes by 180° through $B = 0$.

investigated against both, the thermal cycling between 4.2K and room temperature, and temperature gradient reversal, achieved by moving the heating line between any of the 5 contact pairs contacting the Hall channel. Since no apparent difference was noticed in these tests, it was concluded that the asymmetry is an intrinsic physical property of the periodically modulated 2DEG.

Quite clearly, two main conclusions may be reached from the results presented in this section. Firstly, phonon-drag thermopower was seen to be magnetic-field dependent in the classical limit ($\omega_c\tau_{ei} < 1$), an unexpected observation based on the theory developed for PDTP in unmodulated 2DEGs. Secondly, it was observed that PDTP becomes antisymmetric around zero-field when the electron density of the 2DEG is increased to saturation. This observation is puzzling since it cannot be separated into the sum of symmetrical oscillations and linear magnetic field dependence [15]. Sample imperfections and inhomogenous electron density, which has been observed before, have been ruled out since the resistance oscillations are completely symmetric even at saturation density. Therefore, this antisymmetry was interpreted as a property intrinsic to the PDTP of modulated 2DEGs, even though it seems to violate Onsager symmetry relations [47] which state that the diagonal elements of a transport matrix should be symmetric and the off-diagonal elements antisymmetric (cf. longitudinal and transverse resistance). It is therefore appropriate to develop a theory for these novel thermopower commensurability oscillations (TCOs), and this is presented in the following section.

3.5 Isotropic and anisotropic electron-phonon scattering

Experimental results presented in the previous section provide evidence that the presence of a periodic potential on top of the 2DEG imposes field dependence of PDTP in the classical limit. Theoretically, the effects of the potential on magnetoresistance were found to be well reproduced by assuming an additional diffusion component which modified the longitudinal component of resistivity. Therefore, the calculation the resistivity (or conductivity) tensor modified to take into account the effect of the potential, seems like an obvious starting point in the theoretical analysis of PDTP in modulated 2DEGs.

Choosing an arbitrary set of coordinates, the temperature gradient was assumed to be applied along the superlattice potential $V(y) = V_0 cos(qy)$, where $q = 2\pi/a$. Electron–phonon scattering rate responsible for phonon-drag thermopower in unmodulated 2DEGs, in which the scattering is isotropic, was given by equation 3.18 as

$$\frac{\partial f_k}{\partial t}\bigg|_{ph} = \frac{\partial f_k^0}{\partial \varepsilon_k} \sum_{\lambda} \frac{m^* s_\lambda \Lambda_\lambda}{\tau_{ep}^{\lambda}(\varepsilon)} \mathbf{v_k} . \frac{\nabla T}{T} \ . \tag{3.29}$$

An electron on the Fermi surface moves in the direction $\mathbf{u_1} = (cos\phi, sin\phi)$ ($n = 1$ component of the vector $\mathbf{u_n} = (cosn\phi, sinn\phi)$) with a velocity $v(y)$. It is subject to phonon-drag W^0 given by the integral of isotropic scattering rate over the Fermi surface

$$W^0(y,\phi) = \int_0^\infty dkk \frac{-2e}{4\pi^2} \frac{\partial f}{\partial t}\,|_{ph} = -\frac{v(y)}{2\pi} \frac{\sigma_0 S_0}{D_0} \mathbf{u_1}.\nabla \mathbf{T}. \tag{3.30}$$

In equation 3.30, σ_0 is the Drude conductivity ($= n_s e^2 \tau_{ei}/m^*$), D_0 is the diffusion constant ($= (1/2) v_F^2 \tau_{ei}$), and S_0 is the isotropic PDTP defined by equation 3.21. The thermoelectric current is given by $\mathbf{j}_{th} = \int_0^a (dy/a) \int_0^{2\pi} d\phi f^0(y,\phi) v \mathbf{u_1}$ where f^0 is the charge distribution function given by the solution of Boltzmann's equation

$$\mathcal{L} f^0 = \{v(y)\mathbf{u_1}.\nabla_\mathbf{r} + [v'(y)cos\phi + \omega_c]\frac{\partial}{\partial \phi} + \frac{1}{\tau_{ei}}[1 - \int_0^{2\pi} \frac{d\phi}{2\pi}]\} f^0(y,\phi) = W^0(y,\phi). \tag{3.31}$$

In equation 3.31 $\mathcal{L}$ is the Liouville operator. The superlattice potential is introduced into the system through a function $F^0(y,\phi)$ which has to satisfy $\mathcal{L} F^0 = eE(y)/\epsilon_F$. This is defined as

$$2\pi f^0(y,\phi) = -\frac{v(y)\tau_{ei}}{D_0} S_0 \mathbf{u_1} \sigma_1^0 \nabla \mathbf{T} - F^0(y,\phi)\sigma_1 S_0 [\omega_c \tau_{ei} (\nabla T)_x + (\nabla T)_y]. \tag{3.32}$$

Since the coordinate system was chosen arbitrarily, the periodic electric field is in the y-direction in this case (it was in the x-direction in the analysis of commensurability oscillations), and is given by $E(y) = -dV(y)/dy$. The unperturbed conductivity tensor of order $n(=1,2,3..)$ is $\sigma_{\mathbf{n}}^{\mathbf{0}}$, with components $\sigma_{xx} = \sigma_{yy} = \sigma_n$ and $\sigma_{xy} = -\sigma_{yx} = -n\omega_c\tau_{ei}\sigma_n$, where $\sigma_n = \sigma_0/[1 + (n\omega_c\tau_{ei})^2]$. Fourier expansion in $cos\phi$ and $sin\phi$ of F^0 allows the calculation of the current integrals. Combining the Fourier-expanded F^0 term and $\mathcal{L}F^0 = eE(y)/\epsilon_F$ gives

$$\int_0^a \frac{dy}{a} \int_0^{2\pi} \frac{d\phi}{2\pi} v(y) F^0(y,\phi) \mathbf{u_1} = K(\omega_c\tau_{ei}, -1). \tag{3.33}$$

Equation $\mathcal{L}F^0 = eE(y)/\epsilon_F$ can be solved to first order in $\eta(= eV_0/E_F)$ since the amplitude of the potential $V_0 \ll E_F$. The solution is the same as in the resistivity calculation, and gives the value of K derived in 3.26 and 3.27. Inserting equations 3.32 and 3.33gives the simple result $\mathbf{j}_{th} = -S_0\sigma_1\nabla\mathbf{T}$ where

$$\sigma_1 = \sigma_1 \begin{bmatrix} 1 + K(\omega_c\tau_{ei})^2 & -[1-K](\omega_c\tau_{ei})^2 \\ [1-K](\omega_c\tau_{ei}) & [1-K] \end{bmatrix}. \tag{3.34}$$

This tensor describes conductivity in a periodically modulated 2DEG. Note that if K is set to zero (unmodulated case), the expression for Drude conductivity is recovered.

The thermoelectric tensor is identified as $\epsilon_1 = S_0\sigma_1$. Since $\sigma_1\mathbf{E} = \epsilon_1\nabla\mathbf{T}$, and $\mathbf{E} = S\nabla\mathbf{T}$, the phonon drag thermopower in the presence of the superlattice potential is

$$\mathbf{S_1} = \sigma_1^{-1}\epsilon_1 = S_0\mathbf{I}. \tag{3.35}$$

The B-dependent conductivity tensors cancel giving the same result as in the thermopower section at the start of this chapter. Therefore, in terms of the current theoretical picture, the superlattice has no effect on PDTP and the longitudinal component of thermopower is still independent of magnetic field in the classical limit.

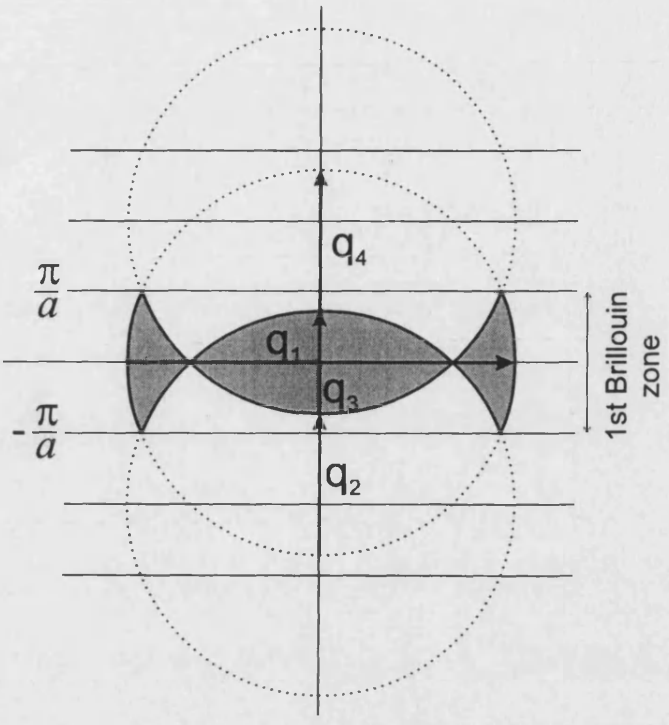

Figure 3.13: Fermi surface in the presence of a superlattice potential modulation. Phonons with wavevectors q_n mediate electron transitions between opposite edges of the Fermi surface.

The result leads to a conclusion that an important factor was not included in the initial assumptions made when deriving the expression for PDTP in the presence of a superlattice. For example, the formation of Brillouin minizones as a result of the periodicity of the superlattice potential, was assumed to have no effect on the scattering rate. The folding of energy dispersion curves shown in figure 3.13, which is the result of the presence of periodic potential, fractures the Fermi surface into a complex pattern of arcs of circle exhibiting two-fold symmetry.

According to the Fermi Golden Rule, the probability of a collision between an electron with wavevector $\mathbf{k}$ and a phonon with wavevector $\mathbf{q}$, is proportional to the matrix element $| < k'|H|k > |^2$, where $\mathbf{k}'$ is the final state of the electron ($\mathbf{k}' = \mathbf{k} + \mathbf{q}$). Figure 3.13 shows electron jumps across opposite sides of the Fermi surface caused by phonon scattering. Since phonons have different wavevectors ($\mathbf{q_1}, \mathbf{q_2}, \mathbf{q_3}, \mathbf{q_4}$), the probability of scatter along x- and y-directions is not equal. This leads to a conclusion that some degree of angular anisotropy in scattering between electron and phonon systems exists, and since scattering is strongly

dependent on the density of available states on the Fermi surface, the anisotropy must be passed onto the scattering rate. It is plausible to assume that Kohn anomalies (divergent density of states) increase the probability of electron-phonon scatter in the direction of the periodic potential where electron transitions are mediated by small wavevector phonons [40].

Anisotropy in electron-phonon scattering was theoretically proposed by P. N. Butcher and M. Tsaousidou [48] in order to account for the difference between the theoretically predicted and experimentally observed transverse coefficient of phonon-drag. Robin Fletcher and co-workers [41] measured thermopower in very low mobility ($0.13m^2/Vs$), very high electron density ($n_s = 3.6 \times 10^{16}\mathrm{m}^{-2}$) GaAs/AlGaAs heterostructures as a function of perpendicularly applied magnetic field in the field range $0 \leq B \leq \pm 8T$ and in the temperature range $0 < T \leq 200K$. They observed that the longitudinal component, although smaller than predicted, was well explained by the theory. The problem, however, arose in the value of the Nernst-Ettinghausen coefficient. The experiment showed that the measured value was 18.5 times larger than the predicted value, however, they offered no explanation for the constant factor 18.5.

The theory introduced here is limited to the low field regime ($\omega_c \tau_{ei} < 1$) and the density of states at the Fermi level is assumed to be unaffected by the magnetic field, since the Landau levels have not been formed. This suggests that the electron-phonon anisotropy is independent of magnetic field [49], and that the scattering rate should be expanded according to its angular harmonics as

$$\frac{1}{\tau_{ep}} = \frac{1}{\tau_{ep}^0}\left[\frac{a_0}{2} + \sum_{n=1}^{\infty} a_n cos(n\phi) + b_n sin(n\phi)\right]. \tag{3.36}$$

A schematic plot of equation 3.36 is given in figure 3.14. The anisotropy in the scattering rate is obvious, furthermore, in $k_x - k_y$ space, the shape of the curve resembles a dumb-bell.

Using the scattering rate given by equation 3.36 and equation 3.30, the driving term $W(y, \phi)$ becomes

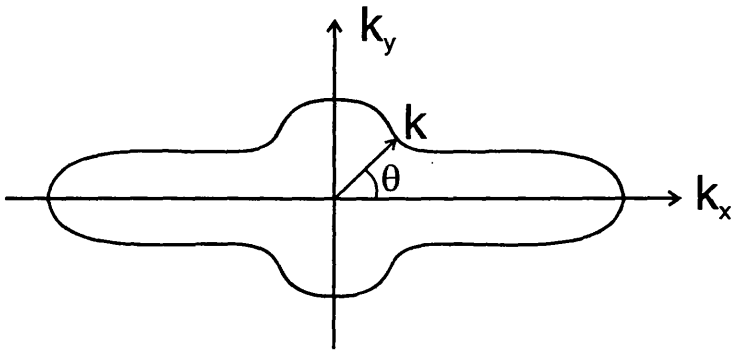

Figure 3.14: A schematic plot of the anisotropic scattering rate in $k_x - k_y$ space.

$$
\begin{aligned}
W(y,\phi) \;=\; & -\frac{v(y)}{2\pi}\frac{\sigma_0 S_0}{D_0}\Big[\frac{a_0}{2}\mathbf{u_1}.\nabla\mathbf{T} \\
& +\frac{1}{2}\left[cos\phi(a_2(\nabla T)_x + b_2(\nabla T)_y) + sin\phi[b_2(\nabla T)_x - a_2(\nabla T)_y]\right] \\
& +\frac{1}{2}\sum_{n=2}^{\infty} cos(n\phi)[(a_{n+1}+a_{n-1})(\nabla T)_x + (b_{n+1}-b_{n-1})(\nabla T)_y] \\
& +sin(n\phi)[(b_{n+1}+b_{n-1})\times(\nabla T)_x - (a_{n+1}-a_{n-1})(\nabla T)_y]\Big], \qquad (3.37)
\end{aligned}
$$

where $S_0 \propto 1/\tau_{ep}^0$. Solution of $\mathcal{L}f(y,\phi) = W(y,\phi)$ appears to be a sum of partial electronic responses to each angular harmonic in $W(y,\phi)$, and, taking advantage of the linearity of the Lioville operator ($f(y,\phi) = f_1^0 + f_1 + \sum_{n=2}^{\infty} f_n$), each harmonic independently contributes to the thermoelectric current and thermopower tensor. Distribution function f_1^0, which corresponds to the first term of equation 3.37, is obtained by substituting the tempearture gradient $\nabla\mathbf{T}$ in equation 3.32 by $(a_0/2)\nabla\mathbf{T}$. Similarly, f_1 is obtained by substituting $\nabla\mathbf{T}$ by $(a_2(\nabla T)_x + b_2(\nabla T)_y, b_2(\nabla T)_x - a_2(\nabla T)_y)$ in equation 3.32. Therefore, the thermopower contribution from the terms with $n \leq 1$ is given by

$$
\mathbf{S_1} = \frac{S_0}{2}\begin{bmatrix} a_0 + a_2 & b_2 \\ b_2 & a_0 - a_2 \end{bmatrix}. \qquad (3.38)
$$

Electronic responses given by the higher n are governed by equation 3.39.

$$\mathcal{L}f_n(y,\phi) = -\frac{v(y)}{2\pi}\frac{\sigma_0 S_0}{D_0}\frac{1}{2}[cos(n\phi)\times[(a_{n+1}+a_{n-1})(\nabla T)_x+(b_{n+1}-b_{n-1})(\nabla T)_y] + sin(n\phi)[(b_{n+1}+b_{n-1})(\nabla T)_x-(a_{n+1}-a_{n-1})(\nabla T)_y] \quad (3.39)$$

The velocity of the electron travelling at the Fermi surface is given by $v(y) = v_F\sqrt{1+\eta cos(qy)} \sim v_F + v_F(\eta/2)cos(qy) + O(\eta^2)$. As before, a function F_n is defined so that

$$2\pi f_n(y,\phi) = -\frac{v(y)\tau}{D_0}S_0\mathbf{u_n}\sigma_\mathbf{n}^\mathbf{0}\nabla\mathbf{T}' - \sigma_n S_0 F_n(y,\phi). \quad (3.40)$$

The effective temperature gradient $\nabla\mathbf{T}'$, discussed in detail later in the chapter, is given by equation 3.41.

$$\nabla\mathbf{T}' = \frac{1}{2}\begin{bmatrix} a_{n+1}+a_{n-1} & b_{n+1}-b_{n-1} \\ b_{n+1}+b_{n-1} & -a_{n+1}+a_{n-1}\end{bmatrix}\nabla\mathbf{T} \quad (3.41)$$

The condition placed on F_n is that it has to satisfy

$$\mathcal{L}F_n = \frac{eE(y)}{\epsilon_F}\frac{1}{2\sigma_n}\left[\frac{n+1}{n-1}\frac{\partial\mathbf{u_{n-1}}}{\partial\phi}+\frac{n-1}{n+1}\frac{\partial\mathbf{u_{n+1}}}{\partial\phi}\right]\sigma_\mathbf{n}^\mathbf{0}\nabla\mathbf{T}'. \quad (3.42)$$

Inserting the expansion of $F_n(=(\eta/v_F\sum_{m=-\infty}^{\infty}\psi_m e^{i(qy+m\phi)}+constant))$ into equation 3.42 gives the recursion formula $\alpha_m\psi_m = \psi_{m+1}-\psi_{m-1}+\beta_m$. This reduces the differential equation 3.39 into an infinite set of coupled algebraic equations, whose solution is given by the complex roots ψ_1 of a fourth-order characteristic polynomial [50]. Once ψ_1 has been calculated, the thermoelectric current can be written as

$$\mathbf{j} = -\sigma_n S_0\int_0^a\frac{dy}{a}\int_0^{2\pi}\frac{d\phi}{2\pi}F_n(y,\phi)v(y)\mathbf{u_1}. \quad (3.43)$$

Solving equation 3.43 then gives the x- and y-components of current

$$j_x = -\sigma_n S_0 \frac{\eta^2}{4} Re[\psi_1], \tag{3.44}$$

and

$$j_y = \sigma_n S_0 \frac{\eta^2}{4} Im[\psi_1]. \tag{3.45}$$

Term ψ_1 is a non-linear function of the temperature gradient $\nabla \mathbf{T}$ and as such, the tensor notation is invalid in expressing the quantities derived from it (namely current density). In experimental situations, however, the temperature gradients are only applied in either the x- or y-directions and not in both simultaneously, and therefore the j_x and j_y components can be represented in tensor form. This means that the expression for the thermoelectric tensor ϵ becomes

$$\epsilon_3 = \sigma_3 S_0 \frac{\eta^2}{4} \begin{bmatrix} Re(\psi_1[(\nabla T)_x = 1, (\nabla T)_y = 0]) & Re(\psi_1[(\nabla T)_x = 0, (\nabla T)_y = 1]) \\ -Im(\psi_1[(\nabla T)_x = 1, (\nabla T)_y = 0]) & -Im(\psi_1[(\nabla T)_x = 0, (\nabla T)_y = 1]) \end{bmatrix}. \tag{3.46}$$

The contribution to thermopower from this component of the thermoelectric tensor is

$$\mathbf{S_3} = \sigma_1^{-1} \epsilon_3. \tag{3.47}$$

The total thermopower is given by the sum of the contributions from two thermoelectric tensors, ϵ_1 and ϵ_3 as shown in equation 3.48.

$$\mathbf{S_T} = \mathbf{S_1} + \mathbf{S_3} = \frac{S_0}{2} \begin{bmatrix} a_0 + a_2 & b_2 \\ b_2 & a_0 - a_2 \end{bmatrix} + \sigma_1^{-1} \epsilon_3 \tag{3.48}$$

The first component $\mathbf{S_1}$ is independent of magnetic field and is equal to the thermopower in the isotropic scattering regime. The second component, $\mathbf{S_3}$ is field dependent and it is this component that gives rise to the oscillatory na-

ture of phonon-drag thermopower. Figure 3.15 shows the result of theoretical modelling of thermopower in the presence of a 500nm period superlattice. The model assumes a unit temperature gradient in the direction perpendicular to the stripes of the superlattice (y-direction) and no gradient in the other direction, $[(\nabla T)_x = 0, (\nabla T)_y = 1]$. The best fit was obtained for $a_0 = a_2 = 40 \pm 20$, where the positive value of a_2 coefficient indicates acoustic phonon scattering enhancement in the direction of the potential, which clearly supports the argument on Kohn anomalies made earlier. All other parameters in the calculation were obtained by experimental measurement on an unmodulated 2DEG, or were given by GaAs/AlGaAs structural parameters.

The term b_2 was set to 0 in the modelling which sets the principal axes of anisotropy to be along the x- and y-directions. The magnitude of the oscillations observed in theoretical S_{yy} trace is proportional to the a_0 term, and if the principal axis of scattering is along the x-axis, the S_{yy} sweep oscillates in phase with resistance.

Although there is good agreement between theory and experiment, the theoretical model does not completely account for the observed features. For example, channelling of open electron orbits is not considered, similar to the case of theory derived to explain magnetoresistance (figures 3.9 and 3.15). This is the reason why calculated curves show a maximum rather than a minimum at zero-field. A more accurate model could be developed in which the real electrostatic potential is calculated, and in which the angular harmonics of higher order than just a_2 are calculated. This should make the agreement between the theory and experiment much better.

3.5.1 Antisymmetric commensurability oscillations

The effect leading to the asymmetry of thermovoltage around zero field [42], observed at high electron densities, is discussed here.

In a periodically modulated system, two principal axes of anisotropy exist. These refer to the directions parallel and perpendicular to the superlattice, and applying the temperature gradient along one such axis results in symmetric thermovoltage around zero-field. Mathematically, this is represented by finite diagonal and zero

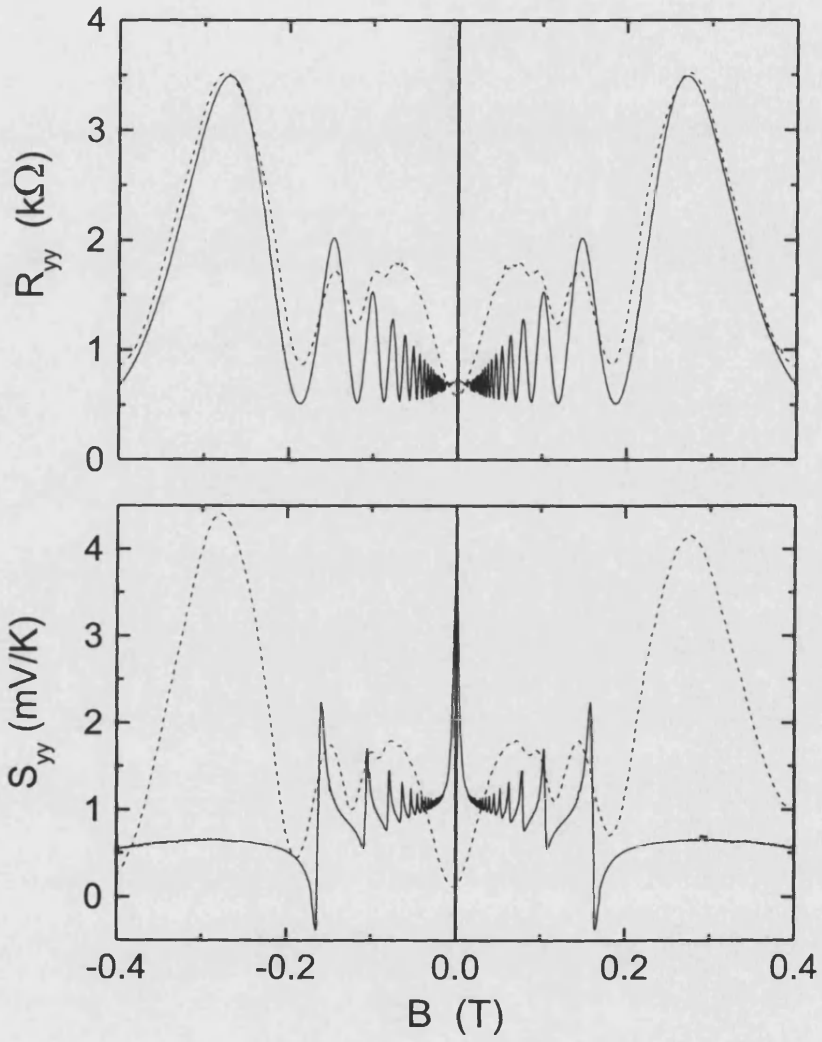

Figure 3.15: Theoretical (full line) and experimental (dotted line) resistance (top) and phonon-drag thermopower (bottom) of a 500nm superlattice. Fitting parameters were $a_0 = a_2 = 40 \pm 20$ and $(b_2 = 0)$. Electron density of the sample was $n_s = 2.45 \times 10^{15} m^{-2}$, scattering time was assumed as 35.6ps and the amplitude of potential was taken as $V_0 = 1\text{mV}$.

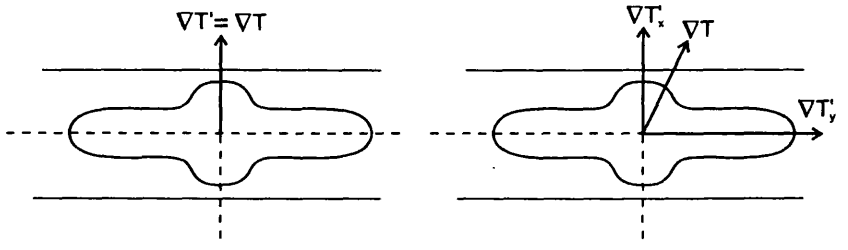

Figure 3.16: (a) The effective and applied temperature gradients act in the same direction whenever ∇T is applied along one of the principal axes of anisotropy (dashed lines). (b) The effective temperature gradient is given by the x- and y-components $\nabla T_x'$ and $\nabla T_y'$ whenever ∇T is rotated away from the principal axes of anisotropy.

off-diagonal ($b_2 = 0$) terms of the $\nabla \mathbf{T}'$ matrix given by 3.41.

If the temperature gradient is applied at an angle to one of the principal axes of anisotropy, both diagonal and off-diagonal ($b_2 \neq 0$) terms in 3.41 are finite. This gives rise to an effective temperature gradient and an asymmetric component of thermovoltage [51]. Figure 3.16 shows schematically the cases when the temperature gradient is (a) aligned with, and (b) at an angle to the anisotropy axes.

The burden of anisotropy was imposed on the temperature gradient tensor rather than the thermopower because it is easier to understand $\nabla T'$ as a projection of ∇T along the principal axis of anisotropy. However, even if the burden was placed on the thermopower tensor, the results of the calculation would be the same since the main parameter is still ∇T. A systematic study of the effect of a finite b_2 term on the symmetry of S_{xx} is presented in figure 3.17.

The symmetry of thermovoltage trace is obvious for the case $b_2 = 0$. As this term was increased, corresponding to the increase in the misalignment between the gradient and the superlattice (shown by the inset), the asymmetric component also increased. A most surprising result was that the traces became completely anti-symmetric for very small angles of misalignment ($\sim 6°$).

Since experimental data showed the increase in asymmetric U_{xx} component with increasing electron density, it might seem incorrect to attempt to theoretically explain the effect in terms of temperature gradients misaligned with respect to the

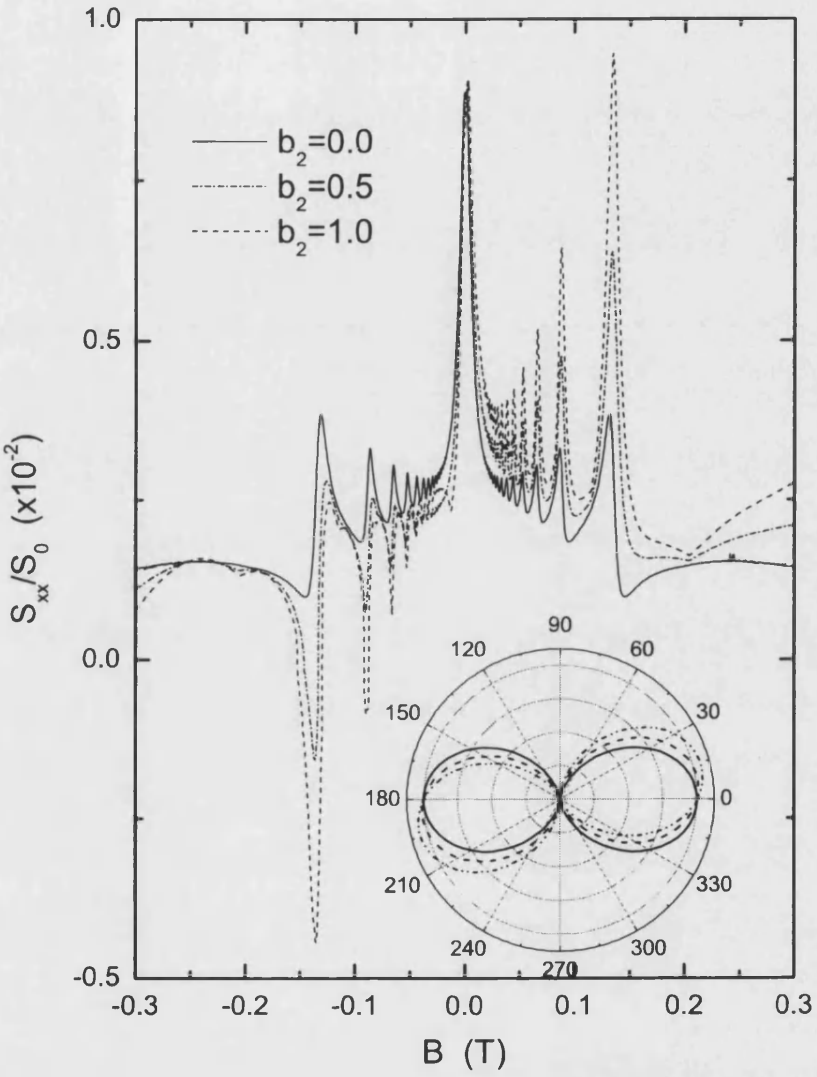

Figure 3.17: The effect of variation of the b_2 term on the symmetry of the phonon-drag thermopower around zero-field. Inset shows the effect of b_2 variation on the electron-phonon scattering rate ($0° - 180°$ line is the superlattice direction).

superlattice. However, the effect of induced gradient is amplified at high n_s (large electron mean free path), and this is the reason why asymmetry was not observed at low n_s where the misalignment was still present. In order to prove this, S_{xx} was studied for a constant finite value of $b_2 = +11$ as a function of varying electron density, as shown in figure 3.18. The lower part of the figure shows high symmetry of longitudinal resistance but increasing asymmetry of longitudinal thermopower. A comparison between this figure and the experimental results in figure 3.12 shows good agreement, however, the asymmetry of the theoretical trace at $n_s = 1.3 \times 10^{15} m^{-2}$ is higher than that of the experimental.

3.5.2 Experimental study of asymmetric thermopower

In order to experimentally investigate the results of theory predicting the origin of antisymmetric oscillations, samples were prepared which contained four independent heaters not connected to the Hall channel (to exclusively measure phonon-drag). An electron micrograph of one such sample with a 500nm periodic dysprosium superlattice is shown in figure 3.19.

The idea was to apply different heating currents to each heater, resulting in temperature gradients which are angles with respect to the superlattice. Clearly, this would resemble the variation of the term b_2 in the model, and would allow the comparison of theoretical and experimental results. Some preliminary results were obtained before the end of the project and the main results is shown in figure 3.20.

As shown above, antisymmetry is reproduced in the two heater samples. The lack of commensurability oscillations in all but one sweep is a problem, however, they might be very damped as the longitudinal resistance also showed damped oscillations. More work is clearly needed in this area, but the preliminary results look promising.

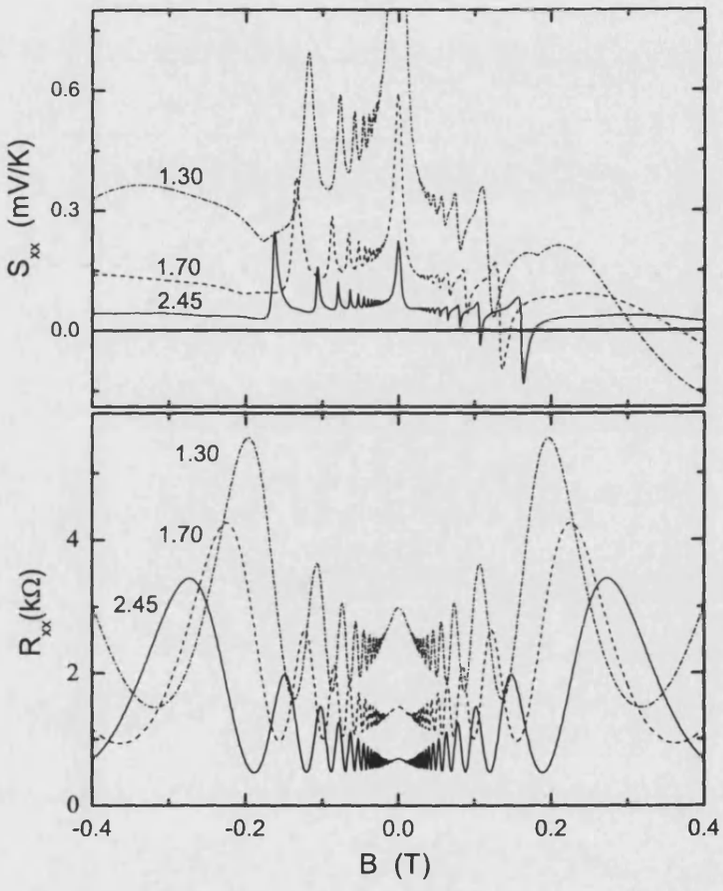

Figure 3.18: The PDTP solution of the Boltzmann equation for $a = 500nm$ sample. The electron-phonon scattering rate is anisotropic in the plane of the 2DEG with Fourier components $a_0 = a_2 = +45$ and $b_2 = +11$. The modelling parameters were $\tau_{ei} = 14, 21$ and $38ps$ for $n_s = 1.3, 1.7$ and $2.45 \times 10^{15}\mathrm{m}^{-2}$ respectively. $S^0 = 110\mu VK^{-1}$. Taken from reference [42].

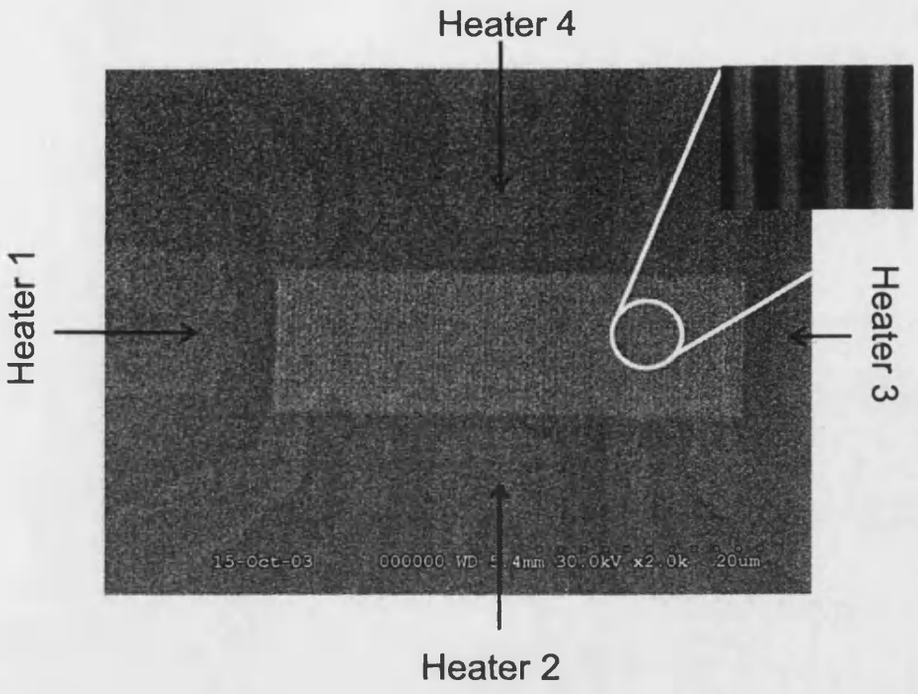

Figure 3.19: The electron micrograph of a sample with two heaters (four heaters present on the sample but only two used at any one time), fabricated in order to test the postulate behind the antisymmetric commensurability oscillations.

3.6 Summary

The first section of this chapter outlined the theory of phonon-drag thermopower in isotropic electron-phonon scattering regime. It was shown that the PDTP is a magnetic field independent quantity, and the experiments performed on unmodulated two-dimensional electron gases prove this. However, deviations from this model occurred when a superlattice inducing electrostatic modulation of the 2DEG was applied. It was observed that the PDTP was no longer field independent but that it displayed commensurability oscillations associated with $\mathbf{E} \times \mathbf{B}$ resonance of the cyclotron guiding centre. The observation that PDTP oscillations were exactly in phase with resistance oscillations at low electron density meant that they could be distinguished from diffusion thermopower commensurability oscillations. These were observed to be 90° out of phase with resistance [8]. The zero-field value of $S \sim 110\mu V/K$ also points to the fact that the measured quantity was almost exclusively due to the phonon drag.

Anisotropy in electron-phonon scattering was used in an attempt to explain the

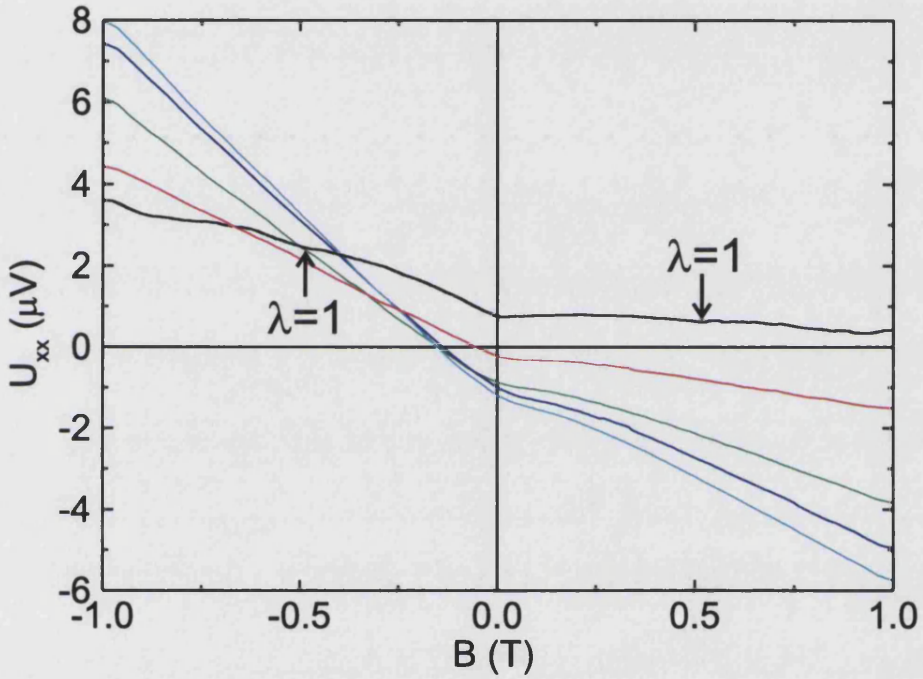

Figure 3.20: The thermovoltage measured in a sample modulated by a 500nm period Dy superlattice with a $\sim$ 6mA heating current applied to heater 1. Heater 2 was connected in series with heater 1 and a variable resistor. Black curve: 6mA current applied only to heater 1. Resistance on variable resistor was 0 (red curve), 20kΩ (green), 40kΩ (blue), 60kΩ (light blue).

experimental observations. It was assumed that such anisotropy breaks the compensation between the thermoelectric and the drift currents (which occurs in isotropic scattering regime) and that this causes the observation commensurability oscillations. The results of mathematical modelling completely support the assumptions made, as shown earlier. Finally, the observation that the commensurability oscillations become antisymmetric at high electron densities was explained in terms of an effective temperature gradient which is induced whenever the applied temperature gradient is not aligned with the principal axis of anisotropy (when it is neither parallel nor perpendicular to the superlattice). The reason why this effect was only observed at high electron densities was that high n_s (and therefore large mean free path) increases the effect of the induced transverse gradient.

Chapter 4

Diffusion thermopower of Sinai billiards

4.1 Introduction

In this chapter, the results of the study of diffusion thermopower in Sinai billiards are presented. The first section contains the background and motivation for the project, followed by the discussion of experimental results obtained. The theoretical model, based on the Landauer-Büttiker formalism, is introduced in the last section.

This work was performed in collaboration with A. G. Pogosov and the Institute of Semiconductor Physics in Novosibirsk.

4.2 Background, motivation and diffusion thermopower

The ability to experimentally distinguish between stable and chaotic orbits in a predominantly chaotic system has prompted an extensive study of magneto-transport coefficients of such systems. In two-dimensional electron gases, chaotic

electron motion can be induced by the application of electrostatic or magnetic potentials in the form of anti-dots, magnetic pillars and disks, stadia and billiards. In 1997, Weiss, Lutjering and Richter [10], published a review paper which dealt with chaotic electron motion in anti-dot lattices. It was a collection of the most important theoretical and experimental results from various works dealing with the subject of dynamic chaos, and it outlined the frontiers of understanding which have been reached.

To date, most experimental studies of dynamic chaos have been centred on magnetoresistance measurements. In light of the recent work in which thermopower of point-contacts [52], quantum dots [46] and Coulomb blockade devices [53, 54] was studied, the investigation of diffusion thermopower of caterpillar-like Sinai billiards was proposed, and is the subject of the present chapter. It was believed that measurements of electron diffusion would reflect new aspects of dynamic chaos undetectable through magnetoresistance measurements.

Sinai billiards are, effectively, one-dimensional forms of the anti-dot array considered by Weiss. Therefore, a brief summary of the dynamic chaos in anti-dot arrays is given as an introduction to the subject. In the majority of systems studied, the mean free path of electrons, l_e, is larger than the period of the lattice a, but shorter than the Fermi wavelength of the electrons, λ_F. This means that the systems can be considered as two-dimensional crystals with semi-classical electron dynamics. The fact that the mean free path is longer than the period of the lattice means that electrons are predominantly scattered by the potential rather than the impurities.

Figure 4.1 is an example of a Poincaré surface of a section of phase space, and it shows that the distribution of regular stable orbits resembles an island surrounded by a sea of irregular chaotic ones. Magnetotransport measurements on a system with such a chaotic/regular distribution gives insight into the difference between the two types of orbits. For example, stable orbits are formed by electrons which become pinned to the hard walls of the potential and ones which 'hop' through the array, whereas chaotic ones are formed by randomly scattered electrons. In terms of physics, both regular and chaotic orbits explain for the observed magnetoresistance features is as follows. Orbits pinned to the potential and the ones which are commensurate with a certain number of anti-dots are trapped. They cannot contribute to transport, thus resulting in a magnetoresistance peak. En-

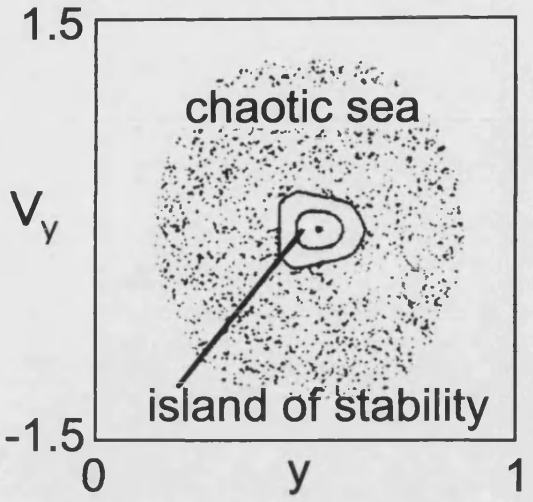

Figure 4.1: Phase space map showing an island of stable electron orbits surrounded by a sea of chaotic ones. (Taken from reference [10].)

hanced conductivity, and consequently a decrease in resistance, was explained in terms of the 'hopping' or run-away trajectories in which electrons were guided through the wire. Surprisingly perhaps, Fleishmann, Geisel and Ketzmerick [55] found that chaotic trajectories trapped in the vicinity of the island of stability also contributed to observed anomalies. Such orbits were formed by electrons which whirl around single or multiple antidots.

In the next section, a brief introduction of the concept of diffusion thermopower is given. It is intended as a basis for the postulate that this transport coefficient should provide further insight into dynamic chaos.

Diffusion thermopower

Diffusion component of thermopower results from the diffusive motion of electrons thermally excited by the application of a small temperature gradient to a conductor. Thermalisation of electrons is achieved by their motion away from the hotter and towards the colder regions, similar to the motion of phonons in the case of phonon-drag thermopower. Schematically, diffusion thermopower can be thought of as excitation of hot electrons (term used to define energetic electrons) to a region outside the Fermi sphere. These energetic electrons return back inside the Fermi sphere through horizontal and vertical processes, as shown in figure

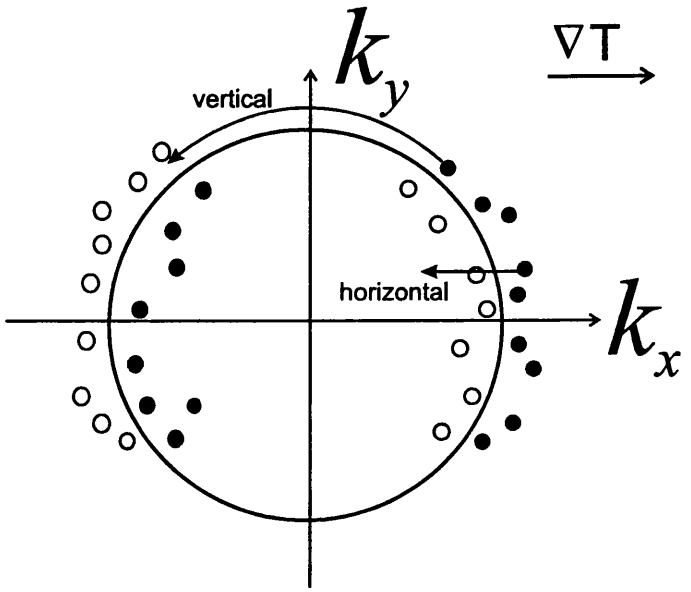

Figure 4.2: The excitation of hot electrons (black circles) from inside to outside of the Fermi sphere. Electrons return to the Fermi sphere through horizontal and vertical processes shown.

4.2.

As figure 4.2 shows, the Fermi surface is not shifted from equilibrium when diffusion thermopower is measured. This is in contrast to resistance and phonon-drag thermopower, where the shift is proportional to the product of electron-impurity scattering time and the electric field, and to the ratio of electron-impurity and electron-phonon scattering times, respectively.

The mathematical expression for diffusion thermopower is obtained as follows. Consider an electron in an energy level E_i in a conductor with a chemical potential μ. Ascribing $\sigma(E_i)$ to that system, the expression for diffusion thermopower becomes [56]

$$S^d = -\frac{1}{|e|T}\frac{\sum_i (E_i - \mu)\sigma(E_i)}{\sum_i \sigma(E_i)}. \tag{4.1}$$

The corresponding result in the Boltzmann semi-classical approach is

$$S^d = -\frac{1}{|e|T}\frac{\int_0^\infty (E-\mu)\sigma(E)(\frac{df_k^0}{dE})dE}{\int_0^\infty \sigma(E)(\frac{df_k^0}{dE})dE}, \tag{4.2}$$

which suggests that diffusion thermopower is closely related to the energy dependence of conductivity. If $\sigma(E)$ was constant, diffusion would be zero since df_k^0/dE is symmetric about μ. Such a situation would arise if the electrical current due to the diffusion of hot electrons from hotter to colder regions was exactly equal to the diffusion of cold electrons in the opposite direction. The sign of diffusion thermopower is influenced not only by the sign of charge carriers but also by conductivity which increases with increasing energy. Consequently, diffusion thermopower coefficient of two-dimensional hole systems is positive.

In the case of degenerate electrons, a good approximation to equation 4.2 is obtained by Taylor expansion of conductivity about the Fermi energy, as shown in equation 4.3. This is allowed since df_k^0/dE decreases rapidly to zero outside the energy range range $E_F \pm k_B T$.

$$\sigma(E) = \sigma(E_F) + \frac{d\sigma}{dE}\Big|_{E_F}(E-E_F) + \frac{1}{2}\frac{d^2\sigma}{dE^2}\Big|_{E_F}(E-E_F)^2 \tag{4.3}$$

Only the first three terms of Taylor expansion of $\sigma(E)$ shown in 4.3 are antisymmetric in E and contribute to $\sigma(E)$. Combining equations 4.2 and 4.3 gives the expression for S^d as

$$S^d = -\frac{1}{|e|T}\frac{1}{\sigma}\frac{d\sigma}{dE}\Big|_{E_F}\int_0^\infty (E-E_F)^2\frac{df_k^0}{dE}dE\,, \tag{4.4}$$

where the integral has the constant value $\frac{(\pi k_B T)^2}{3}$. Clearly, diffusion thermopower is proportional to the energy derivative of conductivity evaluated at the Fermi energy. This makes it a more sensitive tool in the studies of magnetotransport compared to resistance which is proportional to conductivity only, and justifies the postulate made at the start of this chapter that the measurements of electron diffusion in Sinai billiard-modulated 2DEGs should provide further information about dynamical chaos. Through the dependence on conductivity, diffusion ther-

mopower is magnetic field dependent even in the classical limit, $\omega_c \tau_{ei} < 1$.

A convenient way of expressing S^d, proposed by Mott and consequently known as the Mott formula, is shown below.

$$S = -\frac{\pi^2}{3}\frac{k_B}{|e|}\frac{k_B T}{E_F}\frac{dln\sigma}{dlnE}|_{E_F} \tag{4.5}$$

In the derivation of equation 4.2, the conductivity was assumed to be a function of energy only. However, if electrons scatter inelastically off phonons for example, electron energy changes sufficiently to make equation 4.2 invalid. On the other hand, the Mott formula takes into account the slow variation of conductivity on the energy scale $k_B T$, and offers a good approximation to S^d even in the case of inelastic scattering.

4.3 Caterpillar devices

The devices were fabricated from a GaAs/AlGaAs heterostructure with a 2DEG embedded 24nm below the surface, by a combination of electron beam lithography and plasma etching. The electron density and mobility were varied in the range $(1-3) \times 10^{15}\mathrm{m}^{-2}$ and $60 - 80\mathrm{m}^2/\mathrm{Vs}$, respectively. The billiard was formed by patterning and dry-etching of two parallel chains of anti-dots at the opposite edges of the ballistic (1.5μm wide) Hall bar. Each chain consisted of six anti-dots with a lithographic diameter $2d = 0.35\mu$m, period $a = 0.6\mu$m and chain-separation 0.75μm.

Temperature gradient in the system was established by Joule heating technique, similar to the one described in chapter 3 for phonon-drag thermopower. The main difference between the two cases was the amount of current passed through the heating line. In the phonon-drag case, large heating currents were used in order to induce phonons in the lattice, whereas in diffusion case, it was important to apply small heating currents ($\sim 0.4\mu$A) and only increase the temperature of the electron system. This local heating technique works because the time between electron-electron interactions is shorter than the time between electron-phonon

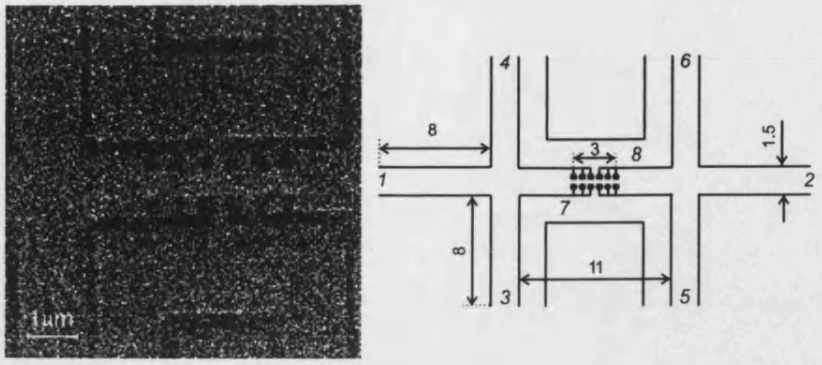

Figure 4.3: An electron micrograph showing the experimental device and the position of the billiard within the Hall channel. The heating line used was between probes (3-4) in the schematic diagram on the left. The numbers in italics are used to label the current/voltage probes. The sample and feature dimensions are expressed in micrometers, and black lines correspond to etched areas of the wafer.

interactions, resulting in a faster spread of the heating power over the electron compared to the phonon system.

Referring to the sample layout shown in figure 4.3, the heating current was applied between probes (3-4) at a frequency *f*, and the voltage drop was measured across the device at a frequency *2f*, as a function of magnetic field applied perpendicularly to the plane of the 2DEG.

4.4 Commensurability effects in diffusion thermopower

Complementary measurements of magnetoresistance, both longitudinal (R_{xx}) and transverse (R_{xy}), were performed on the system by employing the standard four-terminal technique. The experiments were performed in a liquid helium cryostat capable of achieving a base temperature of 4.2K, and incorporating a superconducting coil magnet with magnetic field range $-1 < B_{ext} < 1$T.

Figure 4.4 shows the longitudinal magnetoresistance measured at three values of electron density as a function of magnetic field. As the field was increased from

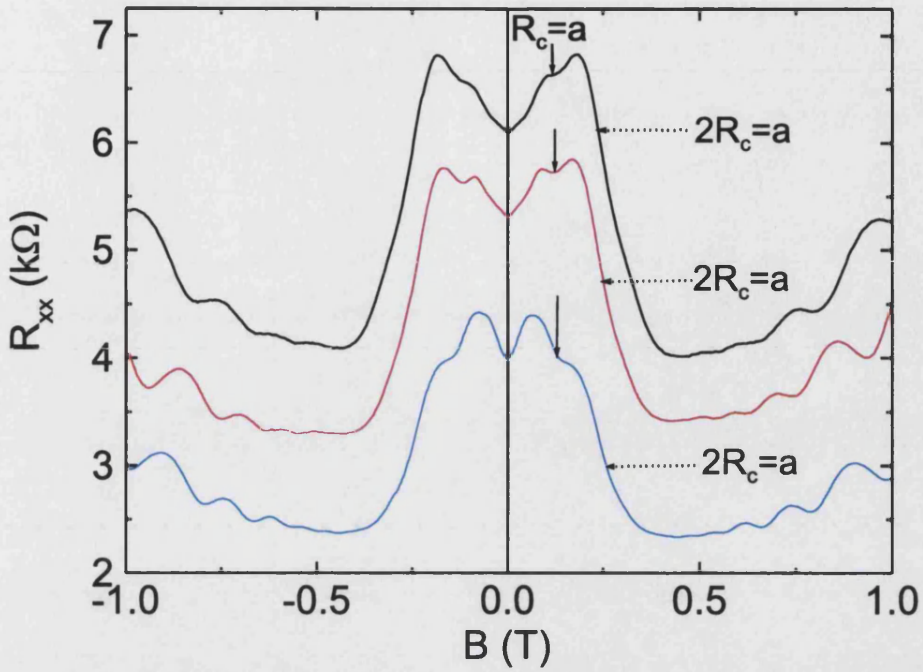

Figure 4.4: The longitudinal resistance measured at n_s = 1.75, 1.94 ,2.07 × $10^{15}\mathrm{m}^{-2}$ (top to bottom curve). Decrease in R_{xx} following the positive magnetoresistance after zero-field and a sharp decrease in R_{xx} at higher field was observed when commensurability conditions $R_c = a$ and $2R_c = a$ were satisfied.

zero, all three traces exhibit positive magnetoresistance due to the backscattering of electron orbits. Further increase in the field resulted in the observation of two regions of negative separated by a region of positive magnetoresistance. The sharp decrease in magnetoresistance [57, 58] was due to the formation of stable run-away electron trajectories at magnetic fields satisfying the commensurability conditions $R_c = a$ and $2R_c = a$, respectively. The region of positive magnetoresistance between the two negative regions is due to the chaotic electron orbits. At field values which do not satisfy the commensurability conditions, electrons are diffusely scattered by the potential, and the resistance increases since they become trapped. In the quantum limit ($B > 0.45$T), the traces exhibit Shubnikov–de Haas oscillations.

The plateaus in the transverse resistance traces shown in figure 4.5 also occurred at field positions which satisfy the commensurability conditions $R_c = a$ and $2R_c = a$. These plateaus occurred because the number of current-carrying electrons was reduced. Such a reduction is a result of magnetic focussing and guiding of electrons by the chains, and a similar observation was made by Weiss *et al.* [10]

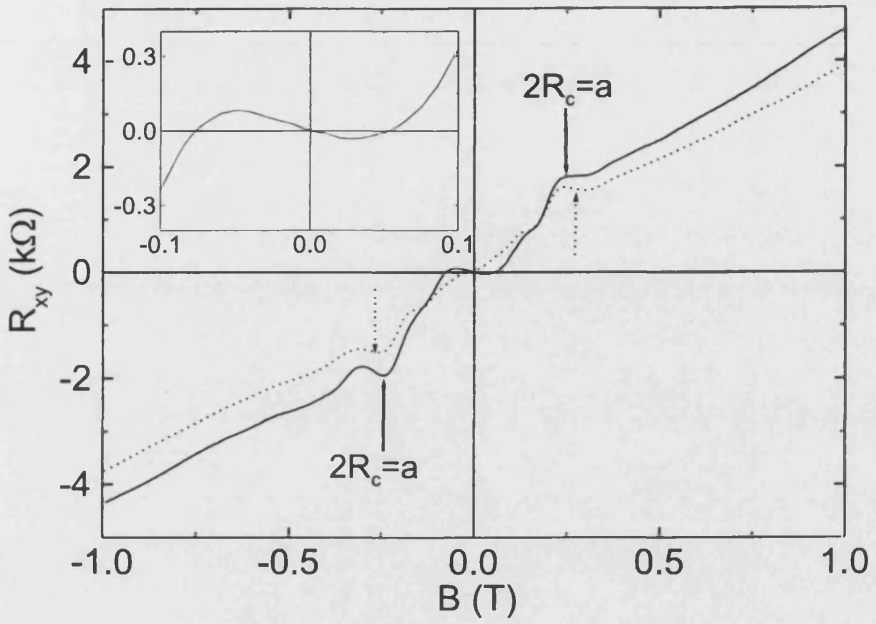

Figure 4.5: Hall resistance showing plateaus at the commensurability condition $2R_c = a$. The inset shows the quenching and negative Hall resistance resulting from electron being scattered in the direction opposite to the direction of Lorentz force. The measurements were performed at $n_s = 1.4$ (solid line) and $1.6 \times 10^{15}\mathrm{m}^{-2}$ (dashed line).

in the anti-dot array case. The 'pinball model', based on Drude conductivity and developed by Weiss *et al.* [59], correctly reproduced this observation. However, another effect seen here and in the anti-dot array samples, could not be explained by the 'pinball model'. As the inset to figure 4.5 shows, the Hall resistance 'oscillates' and is quenched around zero-field. Quenching of Hall resistance is usually associated with ballistic electron systems, however, there must be an additional explanation in the case of anti-dots. The array is macroscopic (size of the array is much larger than the mean free path of electron), and the quenching of the Hall resistance arises due to channelling trajectories confined over many anti-dot cells. The Lorentz force moves these trajectories towards one row of anti-dots from which they are scattered in the direction opposite to the Lorentz force [10]. This is an additional effect giving rise to the negative Hall resistance observed in the Sinai billiards.

Electron orbits which are responsible for the main commensurability effects observed in R_{xx} and R_{xy} are schematically shown in figure 4.6. The condition

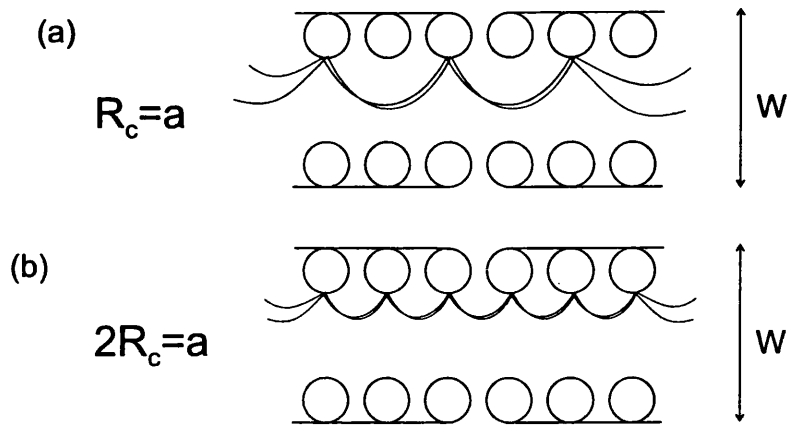

Figure 4.6: Stable electron trajectories at which electrons bounce off every second anti-dot (part a), and every anti-dot (part b) in the chain.

$R_c = a$ is satisfied when the electron bounces off every second anti-dot in the chain, whereas in the condition $2R_c = a$ the electron bounces off every anti-dot in the chain. The formation of chaotic orbits is much easier to envisage. The region of 2DEG which exists between adjoining anti-dots is a good trapping site for electrons. Also, at low fields at which the radius of electron orbit is large, the electron is more likely to be backscattered by the anti-dots in the opposing chain since the channel is finite in width ($1.5\mu m$). Both of these processes contribute to the increased magnetoresistance.

The features observed in thermopower at the fields satisfying commensurability conditions were much more pronounced than the effects observed in resistance. Figure 4.7 is a comparison between $U_{xx/xy}$ and $R_{xx/xy}$, measured at the same value of electron density. The heating current used to obtain the thermopower curves was 0.4μA. The main commensurability effect was observed at $2R_c = a$, where a large amplitude peak in U_{xx} was accompanied by sign reversal in U_{xy}. Similar sign reversal in U_{xy} was observed near zero-field, where Hall resistance was quenched and had become negative.

Longitudinal thermopower exhibits additional structure not observed in longitudinal resistance. The two small amplitude peaks which appear to the left of the large amplitude ($2R_c = a$) peak correspond to the commensurability conditions $R_c = a$ and $2R_c = 3a$. According to the earlier arguments in which the backscattering of large radius orbits was considered, the orbits satisfying $2R_c = 3a$ condition should not have been observable. However, it is plausible to assume that

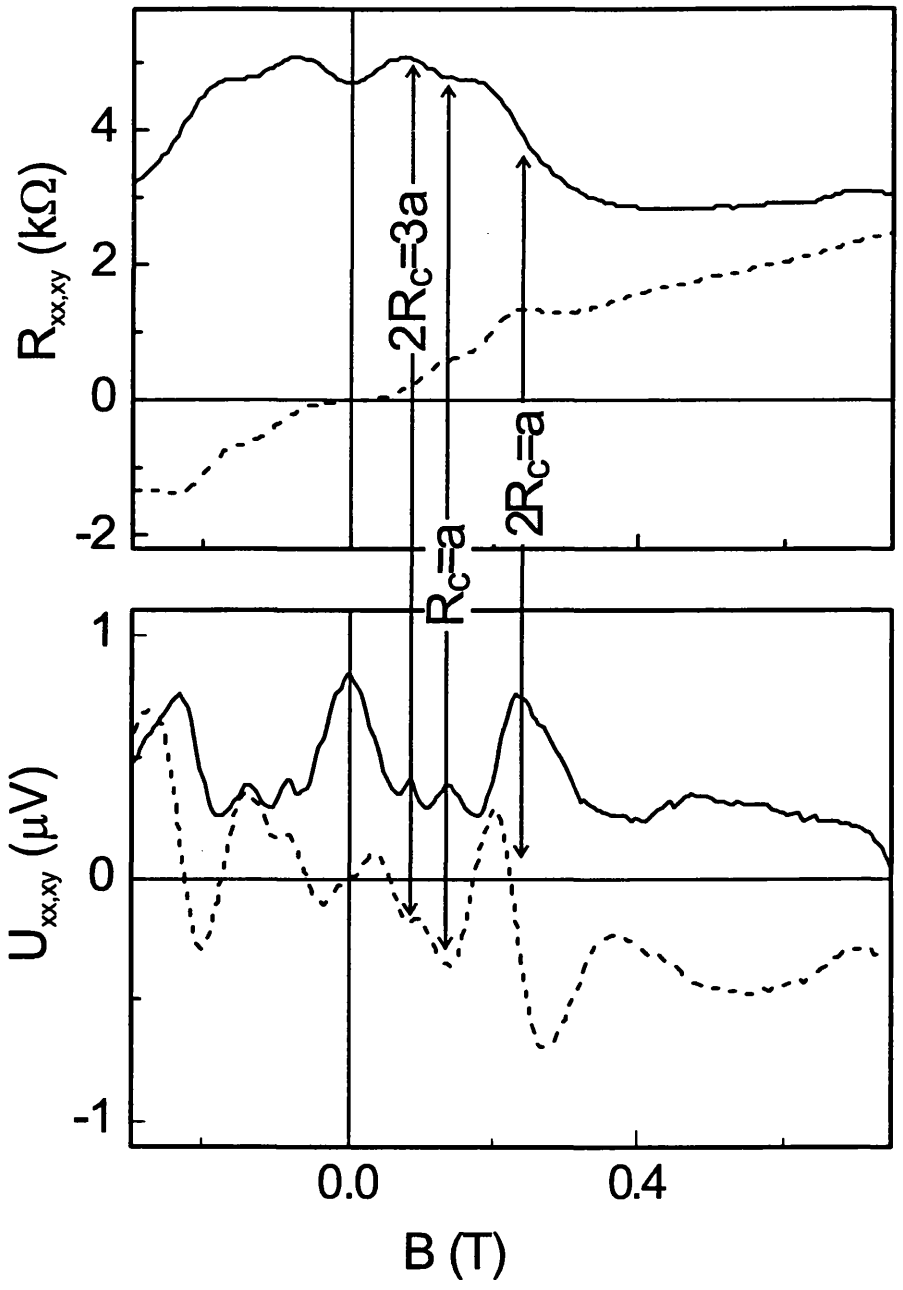

Figure 4.7: The longitudinal (solid lines) and transverse (dashed lines) components of diffusion thermopower compared to longitudinal resistance.

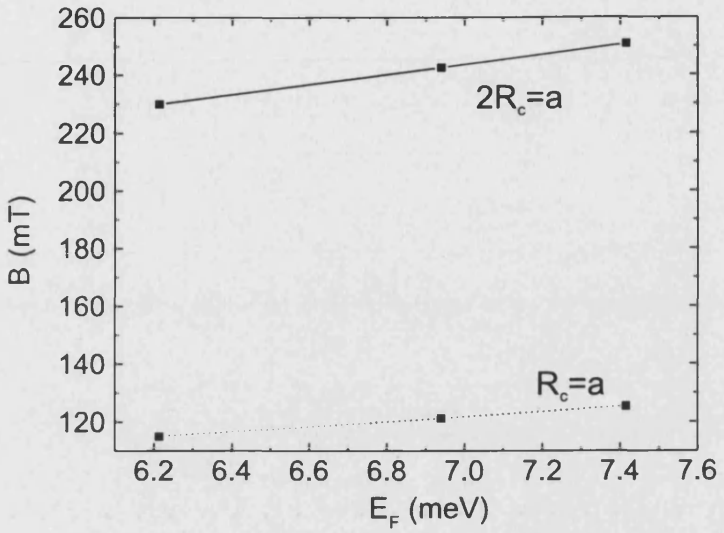

Figure 4.8: The dependence of commensurability conditions $2R_c = a$ and $R_c = a$ on Fermi energy.

a small proportion of these orbits misses the anti-dots in the opposite channel leading to the observed small-amplitude peak. As figure 4.7, both of these effects were less pronounced in the U_{xy} traces.

By calculating the magnetic fields at which commensurability conditions are satisfied as a function of electron density, a plot of the Fermi energy against B was constructed, as shown in figure 4.8. The change in the field values is relatively small with changing E_F, and that is the reason why in figure 4.4 the peaks and minima of oscillations do not seem to vary by a large amount. It should also be noted here that the measurements were performed after a few cycles between room temperature and 4.2K, therefore, the dependence of zero-field resistance on n_s is not a linear function.

4.5 Magnetothermopower tensor in the Landauer-Büttiker formalism

A theoretical model, based on the Landauer-Büttiker formalism [52], has been developed in order to study the effects which led to observed experimental fea-

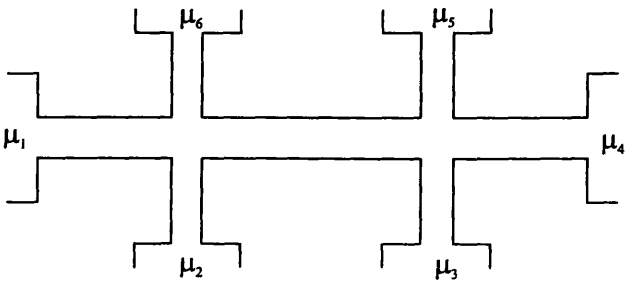

Figure 4.9: Schematic diagram used in the Landauer-Büttiker analysis of a multiprobe ballistic conductor. μ_n are the chemical potentials of the respective leads.

tures. In Landauer-Büttiker approach, which is a usual starting point in the analysis of transport phenomena in multiprobe ballistic conductors, the sample is considered as a conductor attached to perfect phase-randomising reservoirs through ideal leads. Such leads serve as current or voltage probes. A schematic of a diagram used in L-B analysis of a multiprobe system is shown in figure 4.9.

The multiprobe geometry assumes that the current and voltage probes in the system are distinct, giving the total probability of transmission from a reservoir β to reservoir α as

$$T_{\beta->\alpha} = \sum_{n=1}^{N_\beta} \sum_{m=1}^{N_\alpha} |t_{\alpha\beta,mn}|^2, \tag{4.6}$$

where N_α and N_β are the total number of propagating modes connected to reservoirs α and β respectively. The probability of transmission from mode m leaving reservoir β to mode n going into reservoir α is $t_{\alpha\beta}$.

In order to keep the same notation as reference [44], α is replaced by i, β by j, and N_α by M_i in equation 4.6. In the linear response regime, the net current flowing into probe i is

$$I_i = \frac{e}{h}\left[T_{ij} - M_i\delta_{ij}\right](\mu_j - \mu_0) = \frac{e}{h}t_{ij}(\mu_j - \mu_0). \tag{4.7}$$

In equation 4.7, μ_j is the chemical potential (above E_F) of probe j, and μ_0 is the reference chemical potential below which the states with negative and positive

velocities are filled and zero net current flows in each lead. No current flows between the probes when the system is in equilibrium, therefore,

$$\sum_j t_{ij} = 0, M_i = \sum_j T_{ij}. \tag{4.8}$$

The reference chemical potential was arbitrarily chosen as being the potential of probe n. This is permitted since the currents flowing into probe i are independent of μ_0, allowing equation 4.7 to be rewritten as

$$I_i = \frac{e^2}{h}\tilde{t_{ij}}\Delta V_j = \tilde{g_{ij}}\Delta V_j, \tag{4.9}$$

where $\tilde{g_{ij}}$ represents the minors of the matrix of conductance coefficients. The voltage drop between voltage probes j and n is $\Delta V_j = (\mu_j - \mu_n)/e$, and the equation is only true as long as $i \neq n$ and $j \neq m$.

In order to measure thermopower, temperature gradient was introduced across the conductor. Assuming that the temperature difference between probes j and n is $\Delta T = T_j - T_n$, and generalising the two-probe result of Sivan and Imry [60] to the multi-probe geometry considered here, the thermoelectric current was defined as

$$I_i = \tilde{g_{ij}}\Delta V_j + \tilde{\epsilon_{ij}}\Delta T_j. \tag{4.10}$$

The thermoelectric tensor of equation 4.10 is defined in equation 4.11.

$$\epsilon_{ij} = \frac{\pi^2}{3}\frac{ek_B^2 T}{h}\frac{\partial t_{ij}}{\partial E}\,|_{E_F} \tag{4.11}$$

In the first section of chapter 3, total thermopower of a system was defined as the constant of proportionality between the electric field set-up across the conductor and the temperature gradient causing the electric field, $E = S\nabla T$. Theory also specified that current density in a conductor must be zero, therefore,

in the equilibrium regime when all $I_i = 0$, diffusion thermopower of a multiprobe conductor can be written as

$$\mathbf{S} = \mathbf{g}^{-1}\epsilon = \frac{\pi^2}{3}\frac{k_B^2 T}{e}\frac{\partial ln\mathbf{t}}{\partial E}|_{E_F}\,, \tag{4.12}$$

where k_B is the Boltzmann constant and T is the average temperature of the probes, in experimental terms, this is the temperature of the sample bath.

The coefficients of transmission between probes were calculated by taking probe 1 of figure 4.3 as the reference probe. This allowed the definition of transmission probabilities from probe 1 into probe 2 as $T_{21} = T_F$, from 1 to 8 as $T_{81} = T_L$, from 1 to 7 as $T_{71} = T_R$ and from 7 to 8 as $T_{87} = T_{LR}$. Referring to figure 4.3, T_F corresponds to electrons flowing through the channel without deviation, and T_L and T_R correspond to electron being deflected into probes 8 and 7, possibly as a result of perpendicularly applied magnetic field. Clearly, this allows the relations $T_L(B) = T_R(-B)$ and $T_{LR}(B) = T_{LR}(-B)$ to be written. Using the transmission coefficients, the thermoelectric current flowing between the corresponding probes is defined as

$$\begin{pmatrix} I_F \\ I_L \\ I_R \end{pmatrix} = \frac{e^2}{h} \times \tag{4.13}$$

$$\begin{pmatrix} -(T_F+T_L+T_R) & T_L & T_R \\ T_R & -(T_L+T_R+T_{LR}) & T_{LR} \\ T_L & T_{LR} & -(T_L+T_R+T_{LR}) \end{pmatrix} \begin{pmatrix} \Delta V_F \\ \Delta V_L \\ \Delta V_R \end{pmatrix}.$$

No current flows between probes 7 and 8 and therefore there is no I_{LR} component in the expression above. As equation 4.12 shows, thermopower is related to the energy derivatives of the transmission coefficients evaluated at the Fermi energy. However, thermopower was measured as a function of magnetic field, thus, a relation between dT_{ij}/dE and dT_{ij}/dB is required. Considering the billiard as "hard-wall" potential [57], the probability of transmission from probe j into probe i is given by the product of the Fermi wavevector and a function $f(R_c)$ which

is determined by the device geometry, and is itself a function of the cyclotron radius at a field B. This allows the relation between dT_{ij}/dE and dT_{ij}/dB to be defined as

$$\frac{dT_{ij}}{dE}|_{E_F} = \frac{T_{ij}}{2E_F} - \frac{B}{2E_F}\frac{dT_{ij}}{dB}. \tag{4.14}$$

The increase in temperature of the electron system was calculated in a similar way to the case of phonon-drag thermopower described in chapter 3. The power dissipated in the heating line, P_h, resulting from the heating current I_h, is related to the increase in electron temperature at the heater. If the increase in the temperature of the heater is defined as T_h, and assuming that at the opposite end of the sample the temperature is equal to the bath temperature (4.2K in this case), the difference in temperature between those points is $\Delta T_F \sim T_h$. Considering the sample layout, the difference in temperature between probes (1-8) and (1-7) across which voltage drop was measured can be taken as 1/2 of ΔT_F. Heater temperature was estimated using $T_h = P_h/\kappa$, where κ is the heat conductance, as $\sim 150mK$ for a $0.4\mu A$ heating current considered in figure 4.7.

Numerically, individual transmission coefficients ($\mathbf{t}$) were calculated by means of Monte-Carlo simulations. This is based on the approach of Baranger *et al.* [53] who considered classical transmission coefficients in a ballistic structure by using a semiclassical approximation to the quantum Green function

$$|t_{ij,ba}| = \hbar\sqrt{v_b v_a}\left|\int dy_i \int dy'_j \chi_b(y_i)\chi_a(y'_j) \times G^+_\epsilon(x_i, x'_j)\right|. \tag{4.15}$$

Term $t_{ij,ba}$ is the transmission coefficient from mode a in probe j to mode b in probe i. Longitudinal velocities of modes a and b at the Fermi surface are given by v_a and v_b, respectively.

The geometry of the billiard assumed in the definition of $f(R_c)$ term is shown in figure 4.6. Superimposed on the anti-dot chains are the dynamically stable electron orbits responsible for the main commensurability features observed in thermopower. Impurity scattering length, $l_i = 3\mu$m, which smoothes each quantum conduction channel, was included in the model in order to make it more

realistic. Equation 4.16 is the exact solution of the thermopower tensor, and the longitudinal and transverse components obtained from it are shown in figure 4.10.

$$\tilde{\mathbf{S}} = -\frac{\pi^2}{6}\frac{k^2T}{eE_F}\frac{d(ln(\tilde{\mathbf{t}}/B))}{d(lnB)} \tag{4.16}$$

Comparing the experimental and theoretical curves, it is easily concluded that the main commensurability features are correctly reproduced by the model.

The peak in S_{xx} occurring at $2R_c = a$, as well as the smaller amplitude peaks to the left of it, were observed. The only apparent failing of the theory was noticed in the vicinity of zero-magnetic field. The experimental trace of S_{xx} showed a peak in this region, whereas the theoretical curve showed a decrease. The reason for the deviation is that the model assumed a "hard-wall" model, whereas the anti-dot chains generated a "soft" electrostatic potential. In the "hard-wall" model, the Fermi energy is constant between the anti-dots leading to well-defined circular orbits, however, this does not hold if the potential is "soft".

Since the exact calculation of $\mathbf{S}$ represents the sum of several terms, only the dominant terms were considered in order to determine the effect of individual coefficients on the thermopower components. This reduced equation 4.16 into

$$S_{xx} \approx -\frac{\pi^2}{6}\frac{k^2T}{eE_F}G_{xx}B\frac{dT_F}{dB}, \tag{4.17}$$

$$S_{xy} \approx -\frac{\pi^2}{6}\frac{k^2T}{eE_F}G_{xy}B\frac{dT_L}{dB}, \tag{4.18}$$

where G_{xx} and G_{xy} are given by the transmission coefficients as shown below.

$$G_{xx} = \frac{T_L + T_R + 2T_{LR}}{det|\tilde{\mathbf{t}}|}$$

$$G_{xy} = \frac{T_L + T_F}{2det|\tilde{\mathbf{t}}|}$$

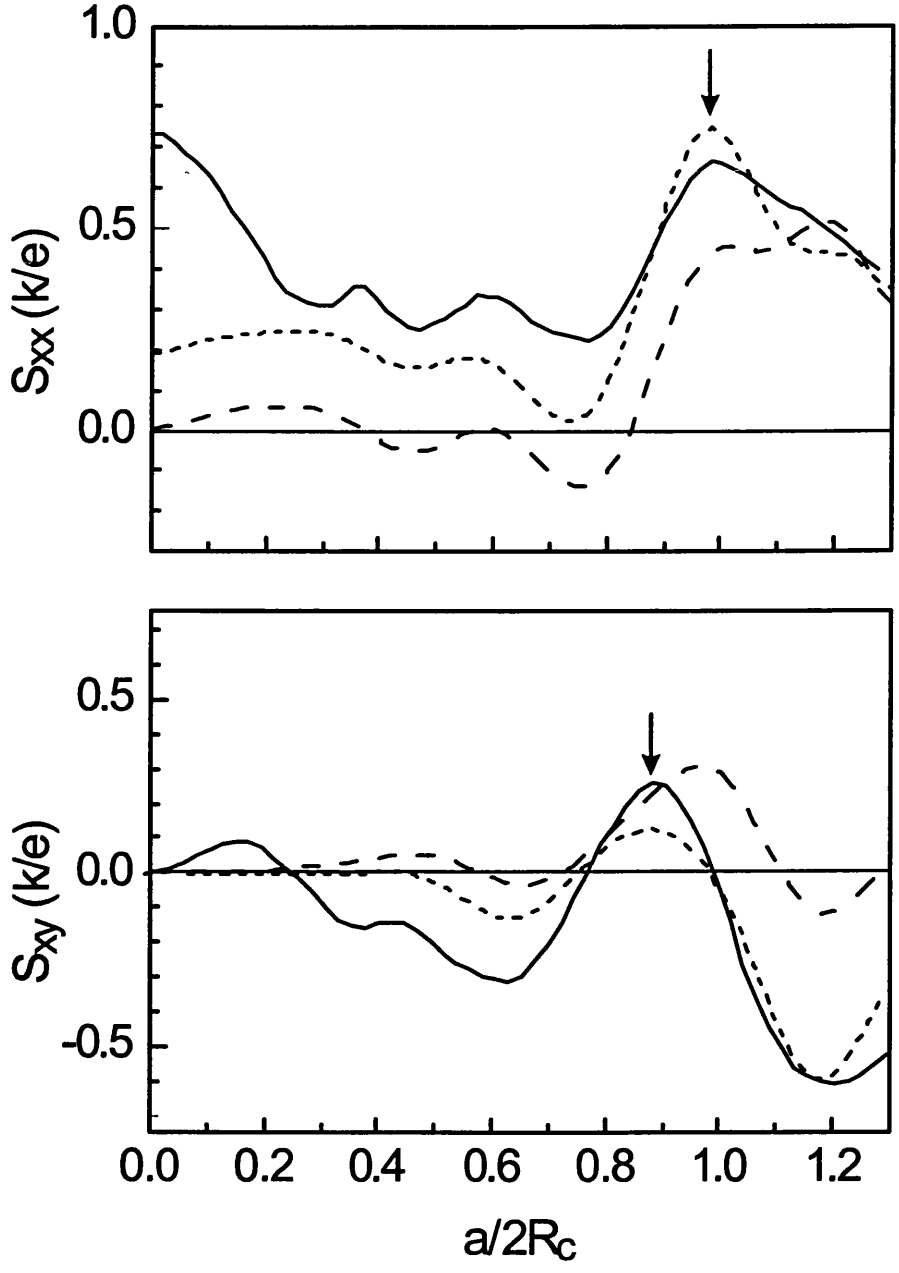

Figure 4.10: Comparison of the measured (solid line) and calculated (dotted line) components of thermopower. Longitudinal component is shown in the top part and the transverse in the bottom part. Impurity scattering length was assumed to be $3\mu m$ and the anti-dot period $0.26\mu m$. The dashed line shows the approximate solution which assumes that S_{xx} is proportional to dT_F/dB and $S_{xy} \propto dT_L/dB$.

Since G_{xx} and G_{xy} are almost magnetic field independent [44], it can be concluded that the main features of S_{xx} are due to magnetic field derivative of T_F, and the main features of S_{xy} to magnetic field derivative of T_L, as shown in equations 4.17 and 4.18. The results of the reduced equations for thermopower are plotted in figure 4.10. The fact that they also reproduce the features at the main commensurability conditions support the theoretical results.

4.6 Summary

In summary, this chapter has outlined the observation of stable orbits in caterpillar-like Sinai billiards. The main effects in both resistance and thermopower were observed at field values at which the cyclotron diameter was equal to the period of the anti-dot chains. Quenching and inversion of Hall resistance near zero-magnetic field was attributed to long electron trajectories scattered by the anti-dots in a direction opposite to the action of Lorentz force.

Theoretical model based on the Landauer-Büttiker approach was developed and solved numerically by Monte Carlo simulations. Experimental observations were correctly reproduced by the model, apart from the low-field regime in which the "hard-wall" model of the potential assumed in the theory breaks down since the real potential in the samples is "soft".

Chapter 5

Magnetotransport in mesoscopic magnetic dots/antidots

5.1 Introduction

The subject of chaotic electron systems, introduced in the previous chapter, is further analysed here. Results of magnetoresistance measurements performed on two-dimensional electron gases modulated by lateral surface dots and anti-dots are presented, along with a semi-classical model developed to explain the observations.

5.2 Periodic electron orbits

Magnetoresistance of anti-dot lattices [61, 62], elliptical anti-dots [63, 64] and magnetic stadia [65], which acquire non-integrable electron dynamics in the presence of a magnetic field, has been the subject of much interest recently. Chaotic electron orbits in these systems arise as a result of electrons colliding with the periodic array of anti-dots [10], an effect not seen in conventional conductors in which electrons collide predominantly with randomly distributed impurities. Systems, such as circular billiards, in which pinned/runaway orbits are replaced by single/multiperiodic orbits, are the subject of the present chapter. An electron

orbit which returns to the point of departure after just one revolution around a billiard is singly periodic, while the one which returns to the point of departure after a few revolutions is multi periodic. The difference between singly periodic orbits is the number of bounces taken to return to the point of departure.

It was the aim of this study to determine the effect magnetic dots and anti-dots have on the magnetoresistance (longitudinal, transverse and bend) of a narrow 2DEG wire. In a magnetically modulated 2DEG, electrons confined to an area between two regions of differing magnetic field move in snake and cycloid orbits [27, 66]. If the sign of the magnetic field is different in the two regions, the electrons will move in snake orbits since the direction of the Lorentz force depends on the sign of the field. This is shown in figure 5.1(a). The application of a magnetic field perpendicularly to the plane of the 2DEG complicates this simple picture. If the case of a thin magnetic stripe (shaded region of figure 5.1(b)) is considered, where the field under the stripe is B_{m1} and outside the stripe $-B_{m2}$, electrons will move in snake orbits only until the externally applied field (B_{ext}) becomes larger than $-B_{m2}$. This is because the external field B_{ext} is superimposed onto the field generated by the stripe, and when $B_{ext} > |B_{m2}|$, the sign of the Lorentz force is the same in both regions. In this regime, electrons move in cycloid-states, as shown in figure 5.1(b).

Considering now the case in which magnetic modulation has a circular profile, snake and cycloid states are forced to revolve around the profile making this an excellent system in the study of single/multi-periodic orbits. An electron which moves in the vicinity of the dot may become trapped by the dot's magnetic potential, and once this occurs such an electron can no longer contribute to transport. However, a small change in the starting conditions may result in the electron being untrapped, in which case it can contribute to transport. Intuitively, such a trapping/untrapping mechanism should result in oscillatory longitudinal magnetoresistance.

Theoretical studies of lateral dot and anti-dot modulated 2DEGs were performed by Peeters *et al.* [67, 68, 69, 70], Sim *et al.* [71, 72], Takagaki and Ferry [73], and Bending *et al.* [74], with only a few experimental studies by Bending *et al.* [75], and Geim *et al.* [76]. The work of Novoselov *et al.* [12] on ballistic electrons modulated by a cylinder of dysprosium is conceptually closest to the work described here, however, two distinguishing features exist. In the devices

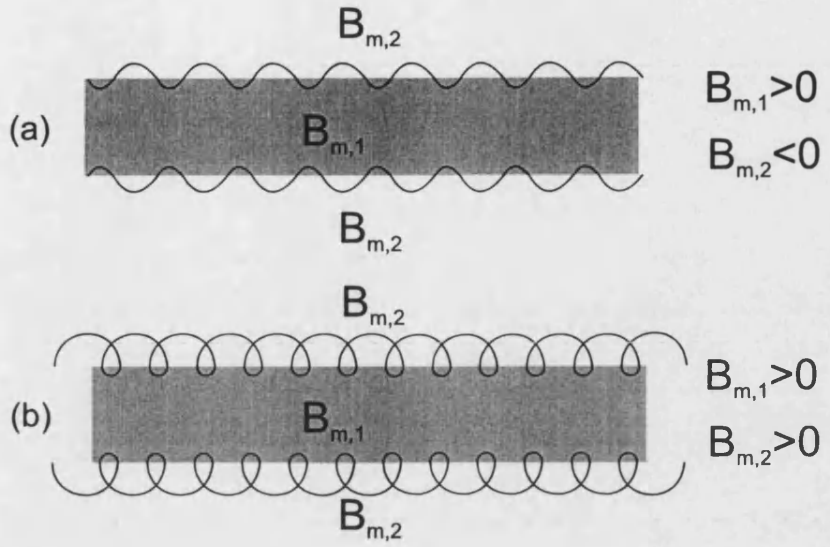

Figure 5.1: (a) Electrons move in snake-like orbits when the sign of the magnetic field resulting from the stripe has different sign on under the stripe and outside the stripe. (b) Applying a perpendicular magnetic field to the system which is larger than the magnetic field outside the stripe ($B_{applied} > B_{m2}$ causes electrons to move in cycloid orbits. Perpendicular magnetisation of the stripe (out of paper) is assumed in this figure.

used here, the distance between the edge of the largest ($4\mu m$ diameter) dot and the edge of the Hall bar was larger than the cyclotron diameter at the values of magnetic field of interest. This meant that the snake and cycloid orbits were not scattered by the edges of the channel, and the effect of the dot could be investigated at low fields as well as high fields. The other main difference is the aspect ratio of disk diameter to disk thickness. Novoselov *et al.* fabricated 1.5μm high cylinders of dysprosium on top of the wire, whereas only thin disks (75, 150 and 225nm thick) were fabricated here. The pillars generate a rectangular-like magnetic field profile in which the magnitude of stray field outside the central area is much smaller than the magnitude of the stray field outside the central area of a thin disk. Therefore, in a pillar geometry, the magnetoresistance effects are related to the presence of a finite-size spot of magnetic field, whereas in the case of a disk, the effects are dominated by the edges of the dot. The comparison of the field profiles generated by a 1μm radius-1.5μm high pillar and a 1μm radius-0.15μm thick disk is shown in figure 5.2.

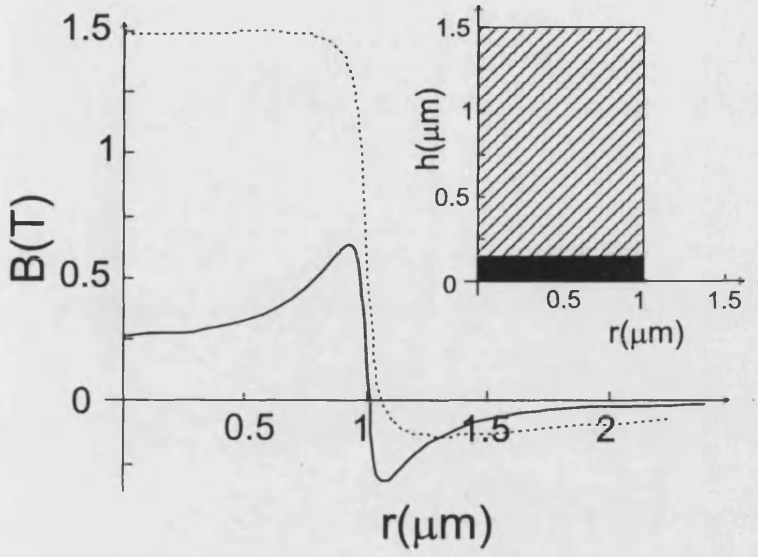

Figure 5.2: The z-component of magnetic field profile generated by a 1.5μm thick Dy pillar (dotted line) and 0.15μm thick Dy disk (solid line) fabricated on top of a 30nm deep 2DEG. The inset shows the size aspect ratios of the pillar and the disk.

5.3 Experimental results

Longitudinal, transverse and bend magnetoresistance was measured in the temperature range 300–600mK (using a He^3 cryostat) at the High Magnetic Field Laboratory in Grenoble, and at T=4.2K at the University of Bath. Magnetic field was applied perpendicularly to the plane of the 2DEG in both cases, and a 200nA excitation current, oscillating at 30Hz, was used throughout the experiment. Prior to the start of experiments, the 2DEG was illuminated by an infra-red LED placed above the sample which had the effect of saturating the electron density to the saturation values given in table 2.1. The application of a gate bias then allowed the density and mean free path to be changed incrementally.

An electron micrograph of a device used in this study is shown in figure 5.3. In part *a* of the figure, the 2DEG is modulated by thin dots of dysprosium, and in part *b* by thin dysprosium anti-dots. The micrographs were taken prior to the fabrication of the Ti:Au gate layer.

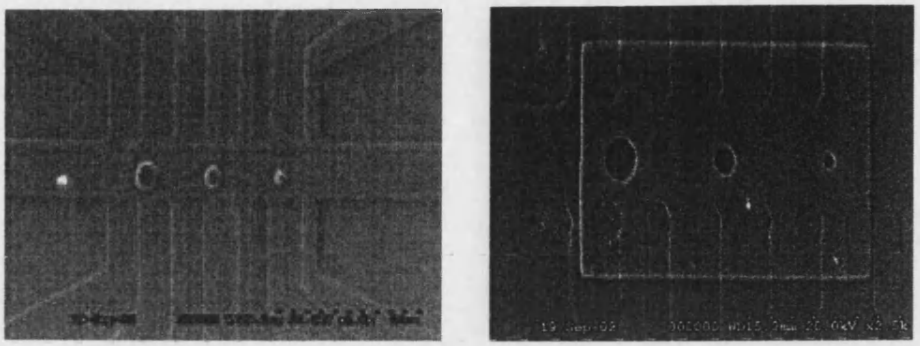

Figure 5.3: Electron micrographs showing the dot (a) and anti-dot (b) structures fabricated in the middle of a Hall bar.

5.3.1 Oscillations in the longitudinal magnetoresistance

The longitudinal magnetoresistance was measured across all three dots of different radii. Figure 5.4 shows the dependence of R_{xx} on gate voltage of the $2\mu m$ diameter, 75nm thickness, dysprosium dot. At negative gate bias (not shown), R_{xx} sweeps were very asymmetric around zero magnetic field and did not exhibit any oscillatory behaviour. The application of positive gate bias, on the other hand, symmetrises the traces and R_{xx} begins to show clear oscillatory behaviour at $V_g = +0.12\text{V}$ ($n_s = 10.06 \times 10^{15}\text{m}^{-2}$). The oscillations appearing in the range $0V < V_g < +0.12V$ ($8.98 < n_s < 10.06 \times 10^{15}\text{m}^{-2}$) are irregular, with some of the peaks merging together. Oscillations at $V_g > +0.12V$ have a small amplitude, and importantly, they appear to be periodic in B.

At saturation electron density ($V_g = +0.24\text{V}$, $n_s = 10.7 \times 10^{15}\text{m}^{-2}$), oscillations are very pronounced with 25mT period, compared to 32mT at $V_g = +0.12V$. In the range of gate voltages ($0.14 < V_g < 0.24\text{V}$) at which R_{xx} oscillations are visible, Shubnikov - de Haas oscillations are also present. Figure 5.5 plots the resistance trace measured at a gate voltage at which the electron density was saturated along with the second derivative of resistance with respect to field. B-periodic behaviour is clearly visible in this figure.

This plot shows that oscillatory behaviour extends from $B = 0$ to the onset of Landau quantisation at $B = 0.6\text{T}$, field much greater than the maximum field obtained outside the dot (-0.066T). The origin of the observed oscillations is clearly not due to geometrical resonances or from quantum interference effects such as

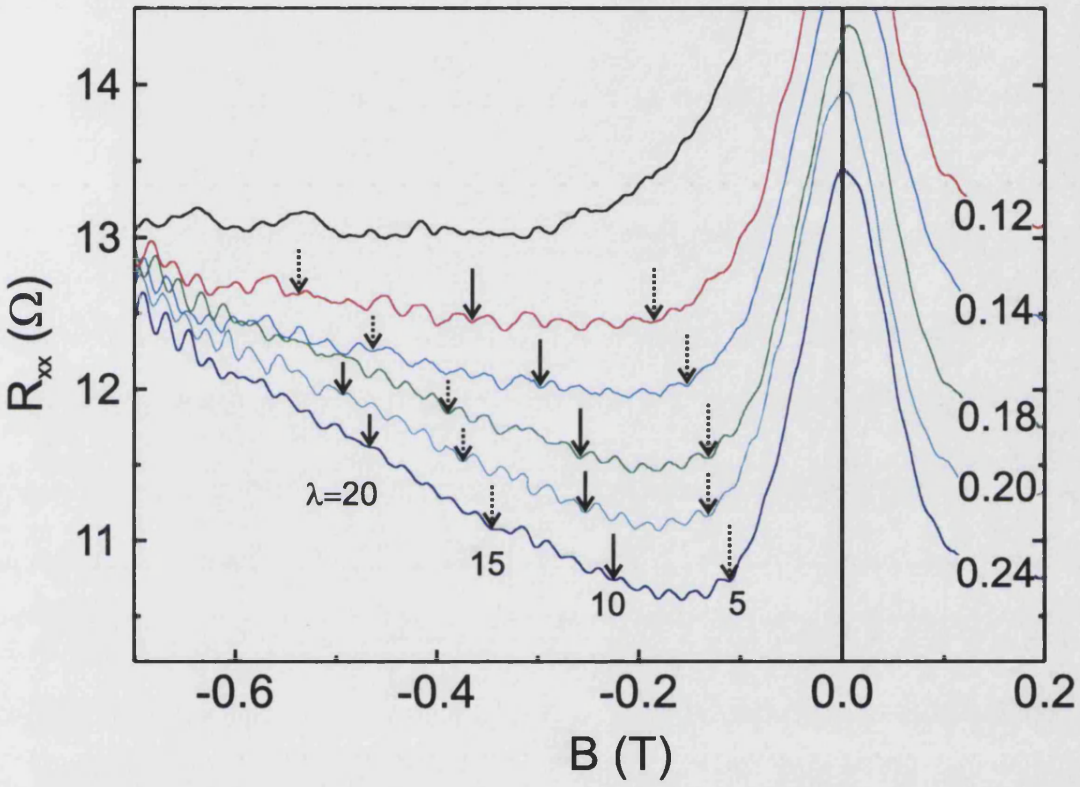

Figure 5.4: Longitudinal magnetoresistance of a $2\mu m$ diameter, 75nm thick dysprosium dot as a function of applied gate voltage (given in the figure in Volts), measured at 4.2K. The corresponding range of electron densities is $10.06 \times 10^{15} < n_s < 10.70 \times 10^{15}\mathrm{m}^{-2}$. The resistance minima are labelled by oscillation indices λ.

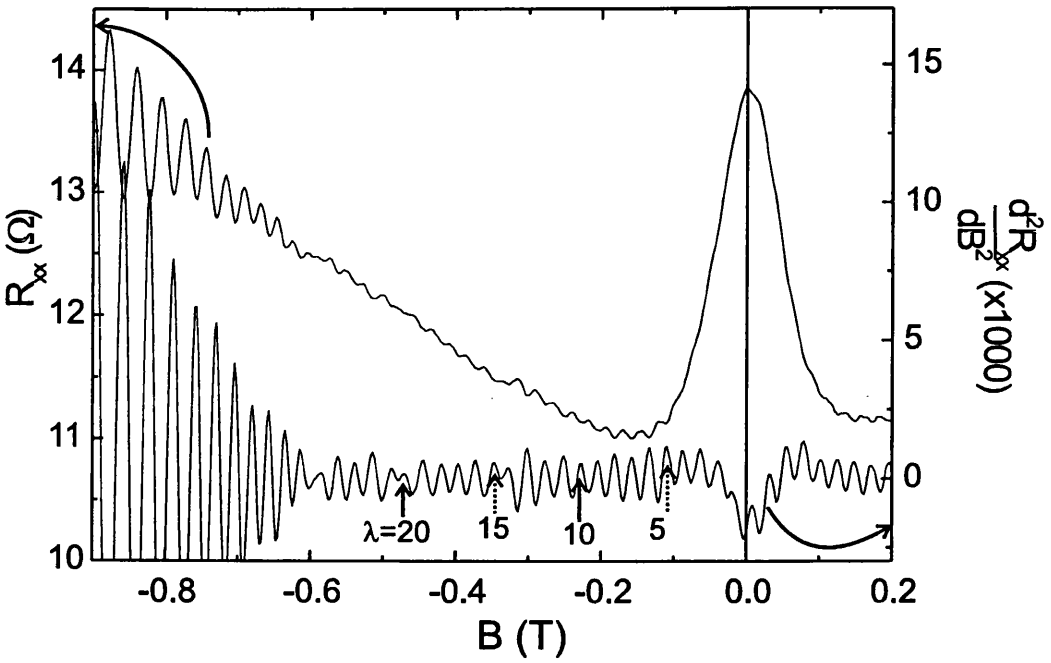

Figure 5.5: Magnetoresistance measured at high n_s and the second derivative of a 2μm diameter dysprosium *dot* (thickness 75nm) calculated for the trace measured at $n_s = 10.70 \times 10^{15}\text{m}^{-2}$.

the Aharonov-Bohm effect. The latter might appear as a logical explanation, however, the 1.7μm [77] thermal length at 4.2K is too short to allow such effects. In support of this claim goes the fact that the calculated period of AB oscillations in a ring of similar size to the dot would be $\sim 0.38mT$, about 60 times smaller than the observed period at the saturation electron density (25mT). The most likely explanation is that, although this system has a chaotic-orbit background, some are stable enough to form singly periodic orbits around the dot. The observation of a monotonic resistance variation across non-patterned sections of the 2DEG also proves that the effect indeed originates within the dot itself.

At vanishing magnetic fields, the field generated by the dot at the centre of the Hall bar is strong enough to backscatter electrons or to trap them in regions of zero field. Both of these effects contribute to longitudinal resistance, thus explaining the appearance of negative magnetoresistance at fields below -0.12T. The positive magnetoresistance seen in the region $-0.6T < B_{ext} < -0.12T$ is due to the electron orbits being small enough ($2R_c = 2.9\mu m$) to pass through the gap between the dot and the edge of the Hall channel ($\sim 3\mu m$).

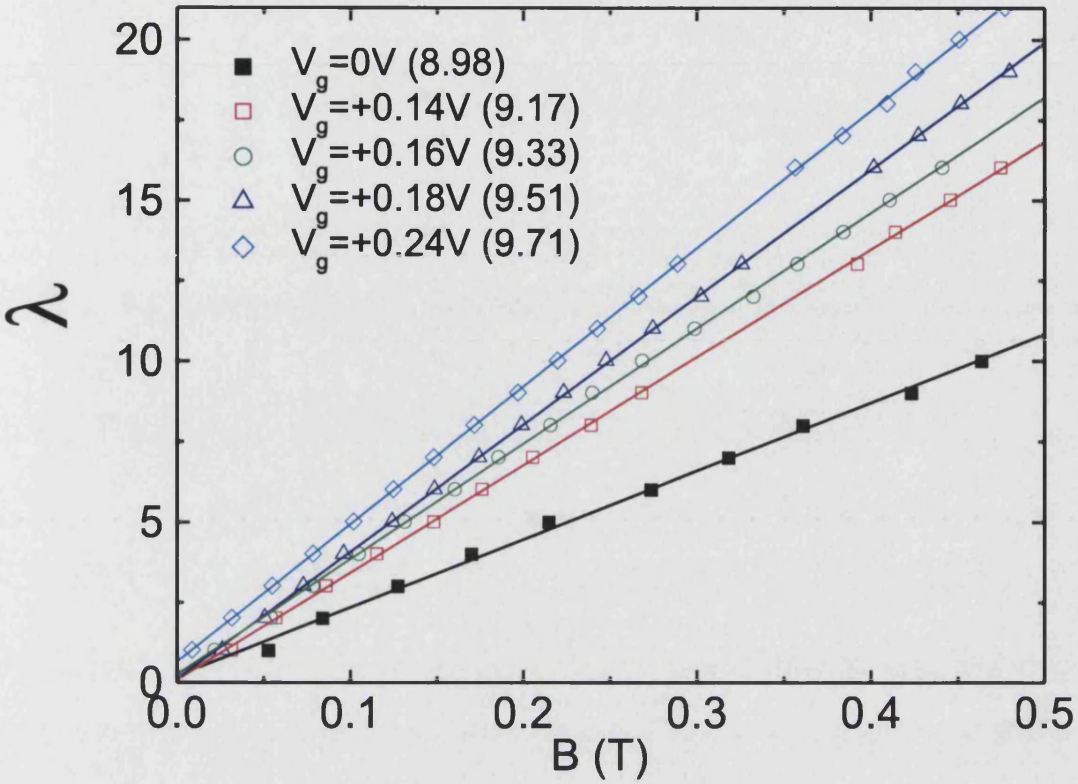

Figure 5.6: Plot of oscillation index λ against external field B for a $2\mu m$ diameter dysprosium dot. The numbers in the brackets refer to the electron density at the corresponding gate voltages. Straight lines are a linear interpolation of each branch.

In the similar way to the analysis of experimental results in chapter 3, magnetoresistance oscillations observed in R_{xx} were labelled by index of oscillation λ, and plotted against B value at which they appeared. This was done in order to demonstrate the B-periodicity and to deduce the dependence of the oscillation period on electron density. Unlike in the commensurability case, however, here the oscillations were numbered from zero-field and plotted against B, as shown in figure 5.6 for the magnetoresistance oscillations of figure 5.5.

Clearly, the gradient of the $\lambda - B$ traces in this fan-like diagram increased with increasing electron density. Also, as expected, no bounces were observed when the external field was zero (apart from the $V_g = 0.24$V curve which suggests that λ was offset by 1 in this case). The gaps in the experimental data exist due to the difficulty in distinguishing between random noise oscillations and true oscillations of sweeps taken at certain gate voltages.

The dependence of oscillation amplitude on the strength of modulation was investigated by measuring R_{xx} across the 75, 150 and 225nm thick dysprosium disks of same diameter dots. Expressed as a percentage of bare 2DEG resistance, oscillation amplitude was seen to increase with increasing disk thickness: 0.75%, 1% and 4% in 75, 150 and 225nm thick disks respectively.

Magnetoresistance was also measured across the larger (3 and $4\mu m$) diameter dots. Figure 5.7 shows the longitudinal resistance measured across a $4\mu m$ diameter dot as a function of gate voltage. Even at the saturation values of n_s, the magnetoresistance of the $4\mu m$ diameter dysprosium dot does not exhibit any oscillatory behaviour (apart from the usual Shubnikov - de Haas oscillations). The same was observed in the $3\mu m$ dot measured at 4.2K. However, oscillatory behaviour was recovered in large radius dots when magnetoresistance was measured in the temperature range 300-600mK. This suggests that the mean free path of electrons plays an important role in trapping of electrons. At 4.2K, the mean free path is shorter than at mK temperatures, and, since the dot perimeter over which electron moves is larger in larger radius dots, the probability that it will be scattered by an impurity while orbiting around the dot is higher. Therefore, there are more chaotic electron orbits at 4.2K compared to 300mK.

5.3.2 Oscillations in the bend resistance

Bend resistance ($R_B = V/I$) measurements were performed on both dot and anti-dot modulated systems. Because of the geometry involved in the measurement of R_B, it is very sensitive to inhomogeneities present in the centre of the Hall cross [78]. Figure 5.8 shows the experimental set-up employed.

Since the magnetic dots or anti-dots were centred on the Hall crosses, effects observed in R_B must be attributed to their presence. Figure 5.9 shows the bend resistance measured across $3\mu m$ diameter dysprosium anti-dot as a function of gate voltage.

B-periodic oscillations are clearly visible in figure 5.9, and they become more pronounced at high gate voltages. The period of oscillations increases with increasing electron density, behaviour opposite to that seen in the case of longitudinal magnetoresistance of the 2μm diameter dot. A plot of oscillation index λ against the

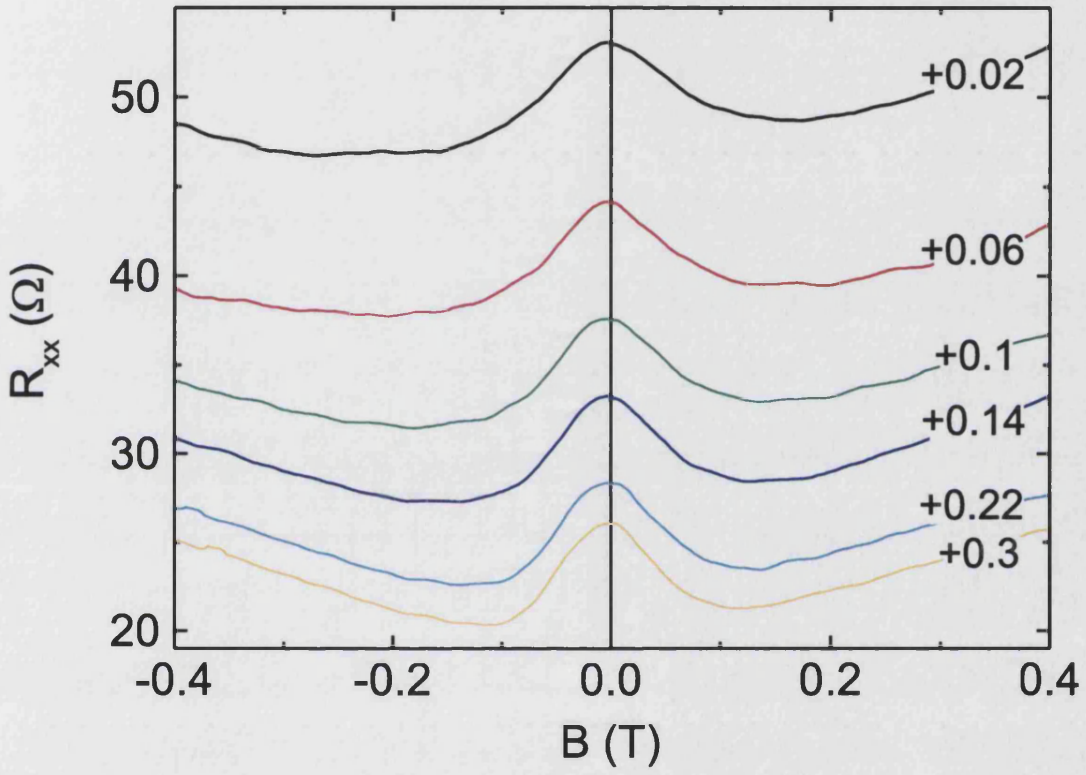

Figure 5.7: R_{xx} measured across a $4\mu m$ diameter dysprosium dot as a function of gate voltage (expressed in Volts in the figure). The corresponding electron densities were $n_s = 5.68$, 6.24, 6.86, 7.50, 8.62 and $9.65 \times 10^{15}\mathrm{m}^{-2}$, respectively. Even at saturation electron density, no oscillations were seen.

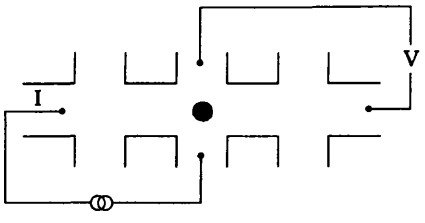

Figure 5.8: The experimental set-up involved in measuring bend resistance.

magnetic field B is shown in figure 5.10.

Measurements of bend resistance were also performed on Hall crosses uniformly covered with a film of dysprosium. This was done in order to determine whether the oscillations observed were indeed due to the presence of the anti-dot or due to the unintentional inhomogeneities in the Dy film. Figure 5.11 shows the bend resistance measured across an anti-dot (part a), and across a channel uniformly covered with dysprosium (part b). The figure was made by defining $B_0 = (mv_F)/(2eW)$ and $R_0 = (h\pi)/(4e^2k_FW)$ ($2W$ is the width of the voltage probe) in order to compare the experimental with theoretical results of Peeters and Li [69]. For the case where $d/W = 1$ (shown), Peeters' theory does predict features in R_b appearing, but does not predict the periodic oscillations clearly visible.

In addition to the case of anti-dots, the bend resistance was also studied in the dots. B-periodic oscillations were again observed, however, they were not as pronounced as in anti-dots at 4.2K. Further experiments were performed in which three samples were cooled to 600mK in order to reduce electrical noise. One of the samples showed B-periodic oscillations in the bend and longitudinal resistance of both 2 and 3μm diameter, 75nm thick dysprosium dots, but the 4μm diameter, 225nm thick dot only showed oscillations in the longitudinal resistance. The results of the low-temperature experiments are presented in figure 5.12.

5.3.3 Non-linear transverse resistance

Transverse magnetoresistance measured across Hall crosses uniformly covered by a film of dysprosium was seen to display small non-linear effects around zero-field, as shown in the upper inset of figure 5.13. Such non-linear effects, superimposed

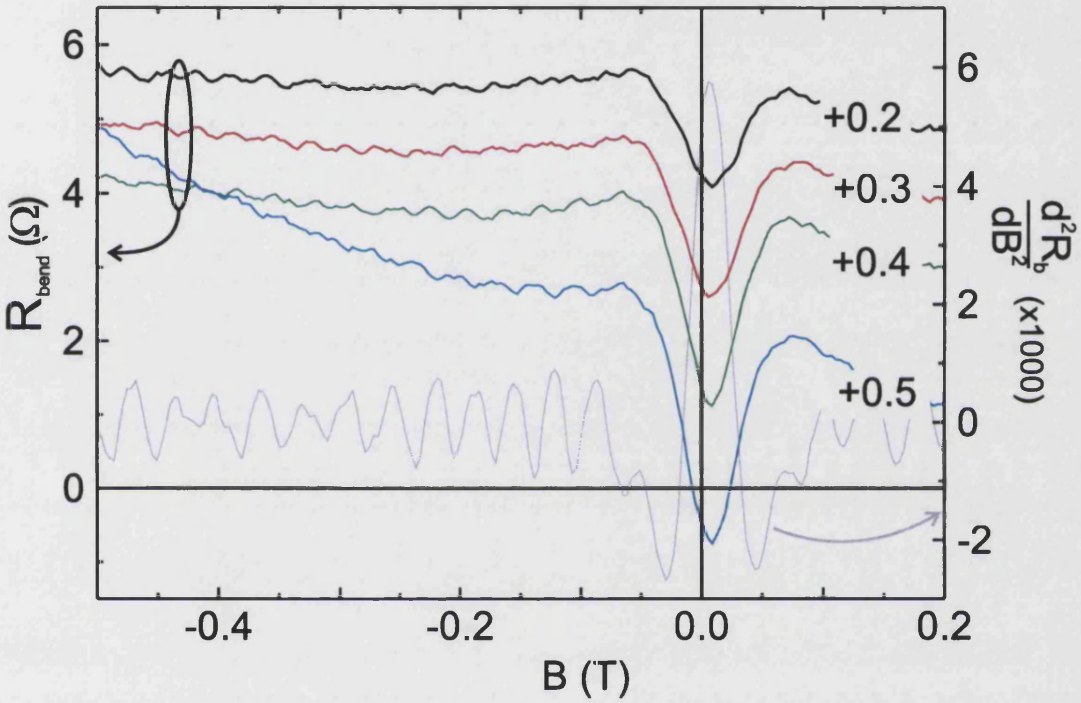

Figure 5.9: Bend resistance measured across $3\mu m$ diameter dysprosium anti-dot as a function of the gate voltage. Corresponding electron density was $n_s = 7.86$, 9.00, 9.67 and $10.36 \times 10^{15}\mathrm{m}^{-2}$, respectively. B-periodic oscillations are clearly visible, as shown in the second derivative of the $V_g = +0.5$V trace.

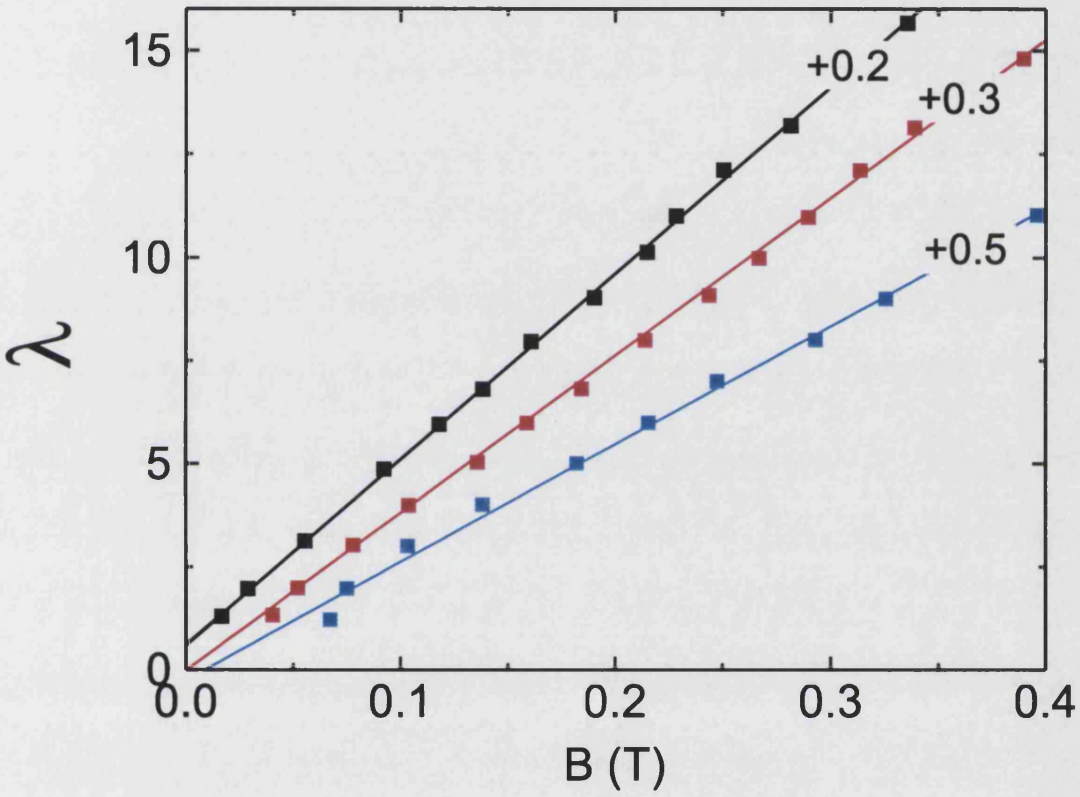

Figure 5.10: Oscillation index λ plotted against the field B at which oscillations in R_{bend} of the $3\mu m$ diameter anti-dot were observed. The period of oscillations increases with increasing electron density ($V_g = 0.2, 0.3, 0.5$V).

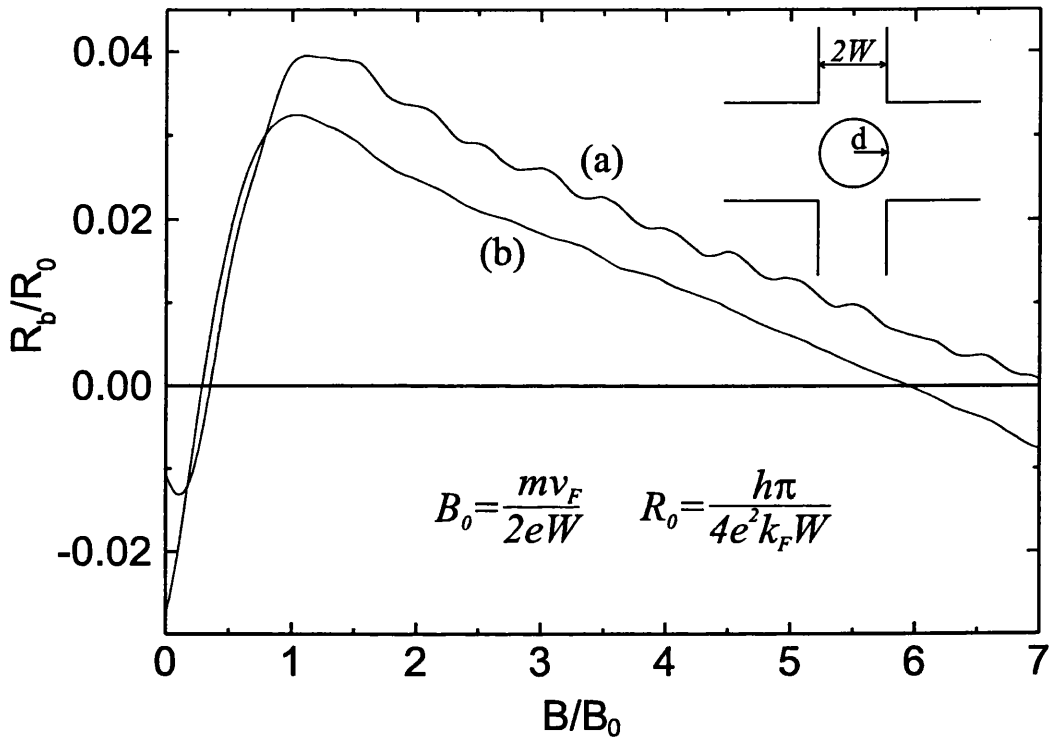

Figure 5.11: Bend resistance measured at $n_s = 10.36 \times 10^{15}\mathrm{m}^{-2}$ across (a) a $3\mu m$ diameter anti-dot, and (b) uniformly covered cross. R_0 and B_0 values were defined in order to compare this plot with the theoretical results of Peeters and Li [69]. The value of d/W was 1 in this figure.

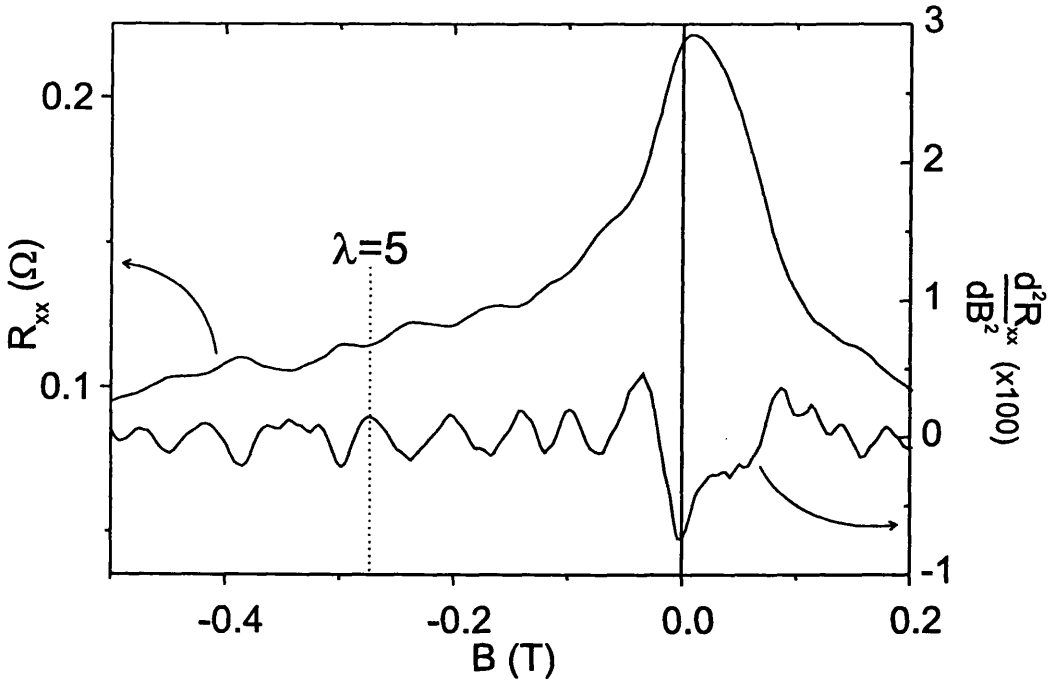

Figure 5.12: Longitudinal magnetoresistance of a 4μm diameter, 225nm thick dysprosium dot measured at 600mK and $n_s = 6.48 \times 10^{15}\text{m}^{-2}$. The presence of oscillations, clearly seen in the second derivative trace, indicates that stable electron orbits around the dot are strongly dependent on electron mean free path.

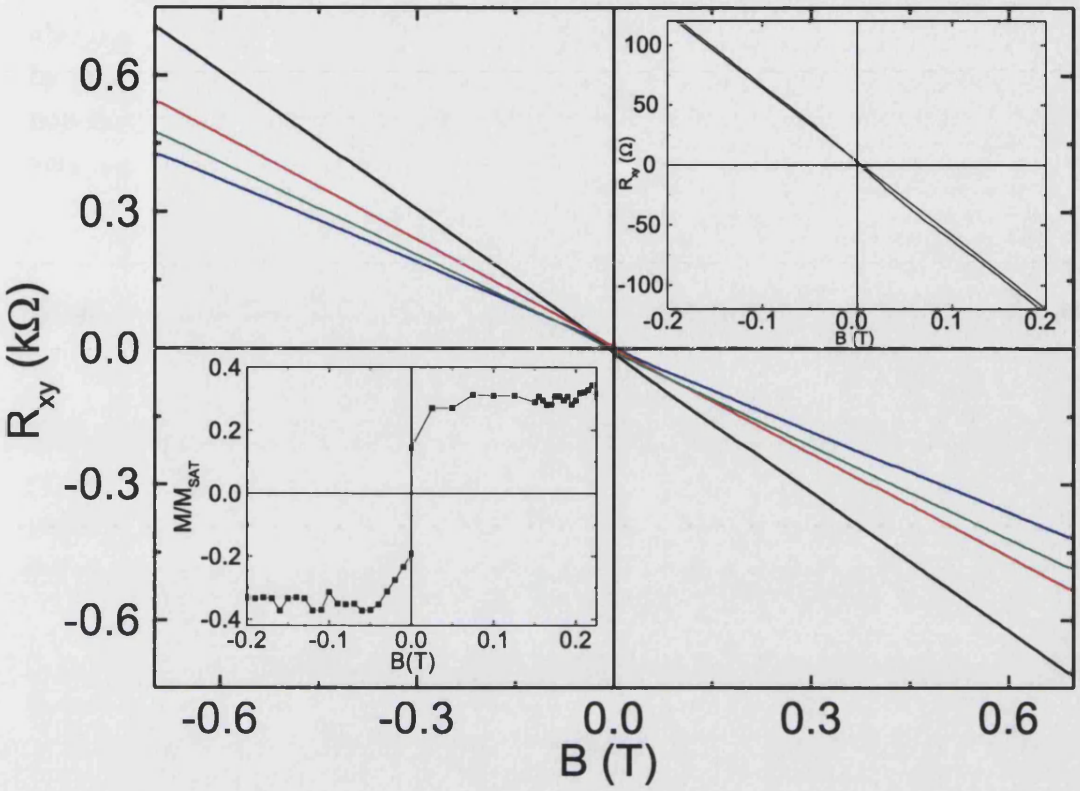

Figure 5.13: Transverse (Hall) resistance measured across a Hall cross uniformly covered with 75nm of dysprosium as a function of electron density. The top inset shows the non-linearity of the curve around zero-field. The bottom inset is the measured *magnetisation curve* of a 150nm thick dysprosium film.

on the linear background, arise as a result of the stray magnetic field of the dysprosium film. By subtracting the linear background from the measured R_H trace, the magnitude of the stray field was quantified (10.5mT at saturation). The stray field was then converted to magnetisation by calculating the stray field induced by a fully magnetised film (16mT), and taking the ratio of the two values. Since the stray field is proportional to magnetisation, a plot of M/M_{sat} was then obtained (lower inset in figure 4.5). As this plot shows, the magnetisation rises to half of the saturation value very quickly, and the further increase is much slower after that.

As expected, the non-linearity of R_H traces decreased with increasing anti-dot radius. In the limit when anti-dot radius is larger than 4.27μm (distance from the centre of the cross to the edge), the Hall cross is effectively unmodulated one, and linear Hall resistance reemerges. Measurements across dots of different radii

also showed non-linear effects. However, because the area of the cross covered by magnetic material is smaller in the case of dots compared to anti-dots, such non-linear component was very small, and magnetometry analysis proved to be very difficult.

5.4 Theoretical model

This section introduces a semiclassical theoretical model developed in order to explain experimental observations. As a starting point, the exact magnetic field profiles of the dots and anti-dots are calculated, followed by the comparison between theory and experiment.

5.4.1 Magnetic-field profiles of dots and anti-dots

Theoretical analysis of the experimental data requires the knowledge of the exact magnetic field profile generated by dots and anti-dots. Based on Craik's treatment [79] of magnetic field generated by surface distributions on a disk, equation 5.1 was derived.

$$H_z = R_d M_s \int_0^\infty J_1(\epsilon R_d) J_0(\epsilon x) sinh\left(\frac{\epsilon h}{2}\right) e^{\epsilon\left(z-\frac{h}{2}\right)} d\epsilon \qquad (5.1)$$

The radius of the dot is given by R_d, M_s is the saturation magnetisation of dysprosium ($\mu_0 M_s = 3.67$T), x is the radial distance, z is the depth of the 2DEG below the surface, h is the height of the dot, J_0 and J_1 are the zeroth and first order Bessel functions respectively, and the integral is performed over ϵ. Figure 5.14 shows the exact profile of the 2μm diameter, 75nm thick dysprosium dot fabricated on top of a 30nm deep 2DEG.

In a similar way to which equation 5.1 was obtained, an equation for the magnetic field profile of the anti-dot was derived as shown in equation 5.2.

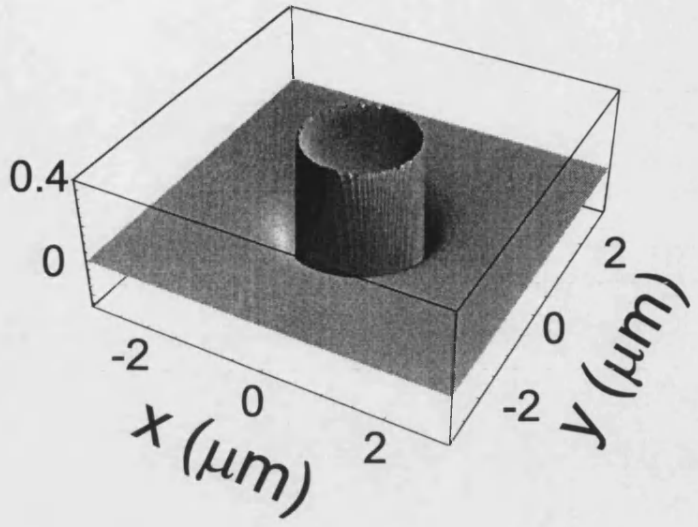

Figure 5.14: The exact field profile of a $R_d = 1\mu$m, $t = 75$nm dysprosium dot fabricated on top of a 30nm deep 2DEG.

$$H_z = \sigma \int_0^\infty J_0(\epsilon x)\left(bJ_1(\epsilon b) - R_{ad}J_1(\epsilon R_{ad})\right) sinh\left(\frac{\epsilon h}{2}\right) e^{\epsilon\left(z-\frac{h}{2}\right)} \qquad (5.2)$$

5.4.2 Orbit quantisation

A semi-classical model has been proposed [80, 81] which considers electron motion around the dot in cycloid orbits only. The reason why snake-state motion was ignored is because the value of the magnetic field outside the dot is small (~ -0.07T when $t = 75$nm), therefore, these states would only persist until external field exceeded $+0.07$T. This assumption is also justified by the observation of only three oscillations in the d^2R_{xx}/dB^2 plot of figure 5.5 for the external field values below 0.07T, thus clearly, the larger proportion of oscillations is due to cycloid-state motion.

In order to simplify the model, magnetic field generated by a dot was approximated from the exact profile to a top-hat function. This, however, does not invalidate the theoretical results since the purpose of the exact field profile was to determine whether or not the dot is capable of trapping electrons. As figure 5.14 shows, in the exact profile the strength of the field is much larger close to the edge of the dot compared to its centre, while in the top-hat profile a sin-

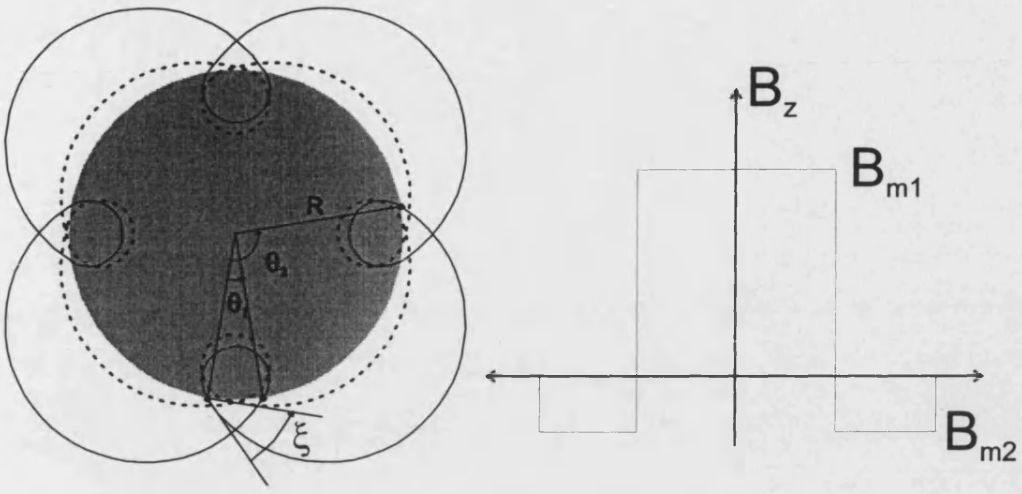

Figure 5.15: Approximate profile of the magnetic field generated by a dot of radius R. Field under the dot is B_{m1} and outside it B_{m2}. Electron trajectories are superimposed on the field profile shown on left hand side.

gle value under the dot ($B_{m1} = +0.55$T), and a single value outside the dot ($B_{m2} = -0.05$T) is assumed. The top-hat profile is shown in figure 5.15, with electron orbits superimposed on top of it.

As the starting point for the model, an electron is assumed to be outside the dot. After some time, the electron moves towards the dot and enters the region under the dot at an angle ξ relative to the tangent, as shown in figure 5.15. The magnetic field acts in the z-direction, however, it varies in the x-y plane and therefore it can be written as $\mathbf{B} = (0, 0, B(x, y))$. If the velocity of the electron is $\mathbf{v}$, the equation of motion can be written as

$$m\frac{d\mathbf{v}}{dt} = q\mathbf{v} \times \mathbf{B}, \tag{5.3}$$

where the mass of the electron is m and the charge is q=-e. The result of taking the cross product of $\vec{v}$ and $\vec{B}$ gives two differential equations for the velocity in x- and y-directions. Integrating these equations gives

$$v_x = v_F cos\left(\omega_c t + \xi\right), \tag{5.4}$$

and

$$v_y = v_F sin\left(\omega_c t + \xi\right). \tag{5.5}$$

In equations above, ω_c is the cyclotron frequency, defined in equation 1.7, and v_F is the Fermi velocity of the electron. The x- and y-coordinates of the electron as a function of time are then obtained by integrating equations 5.4 and 5.5. The electron next encounters the dot edge after a time t_A at a point A (refer to figure 5.15), and after calculating t_A, the x- and y-coordinates of point A were obtained. Simple trigonometry then allows the calculation of angle θ_1 in terms of the incident angle ξ as

$$\theta_1 = cos^{-1}\left(1 - \frac{2sin^2(\xi)}{1 + a_1^2 - 2a_1 cos(\xi)}\right). \tag{5.6}$$

Using similar arguments, the expression for θ_2 can be obtained. However, a closer look at the problem shows that, to satisfy symmetry arguments, the angle at which the electron enters the region outside the dot is $-\xi$, and since the radius of the orbit changes to R_2, it is sufficient to substitute a_1 by a_2 and ξ by $-\xi$ in equation 5.6 in order to obtain angle θ_2.

$$\theta_2 = cos^{-1}\left(1 - \frac{2sin^2(-\xi)}{1 + a_2^2 - 2a_2 cos(-\xi)}\right). \tag{5.7}$$

Full derivation of angles θ_1 and θ_2 is given in appendix B.

Since the extent of the magnetic field outside the dot is finite, there exists a threshold field which needs to be applied below which the electron would escape from the dot. Considering the dot in figure 5.15, the threshold field is the one at which the cyclotron radius outside the dot (R_2) is smaller than the radius of the dot, R_d. The field generated by the dot is superimposed on the externally applied field, so the total field under the dot is $B_{m1} + B_{ext}$ and outside $B_{m2} + B_{ext}$. This allows the definition of electron radii inside and outside the dot as $R_1 = \hbar k_F / e(B_{m1} + B_{ext})$ and $R_2 = \hbar k_F / e(B_{m2} + B_{ext})$, respectively, from which dimensionless parameters $a_1 = R/R_1$ and $a_2 = R/R_2$ follow.

Intuitively, it may be seen that in order to form singly-periodic cycloid orbits, an integral number of bounces (n) has to fit around the circumference of the dot. This imposes a quantistion condition on the angle at which electron enters the region under the dot.. In terms of the angles θ_1 and θ_2, this condition is satisfied when

$$\theta_2 - \theta_1 = \frac{2\pi}{n}. \tag{5.8}$$

For completeness, in the calculation of the quantisation condition for snake orbits, the minus sign on the left hand side of equation 5.8 would be replaced by a plus sign. The orbits of electrons entering the region under the dot at angles which do not satisfy the quantisation condition are not singly periodic and are more likely to be scattered out of the orbit by impurities. This is especially true at low electron densities of the 2DEG at which the mean free path is short.

There are two solutions which satisfy equation 5.8 for the same value of n, therefore, two electrons entering the region under the dot at different angles (ξ_1 and ξ_2), can both orbit the dot in the same number of bounces. At a particular field B_{ext}, both of these orbits are expelled simultaneously.

The lowest number of bounces an orbit can posses is 3. The reason why *n=0, n=1* and *n=2* cannot occur is that in the first case the electron is not trapped by the dot if there are no bounces. The *n=1* orbit is not permitted because the radius of the cyclotron orbit outside the dot would have to be larger than the radius of the dot itself, which as stated earlier, is not permitted. Similarly, if equation 5.8 is considered, the *n=2* orbit would have to satisfy the condition $\theta_2 - \theta_1 = \pi$, which gives $R_2 = R_d$, another forbidden case. The model works in the following way: *n=3* is the lowest orbit and is bound when the external field is $B_{ext}^{n=3}$. Increasing the field slightly untraps this orbit since the electron no longer satisfies the condition given by equation 5.8. Such an electron then performs multi-periodic orbits. The next orbit, *n=4*, gets trapped when the field is increased by an amount ΔB, which is the period of oscillations. All the higher n orbits get trapped when the field is increased even further, thus the trapping of orbit n occurs when the field is equal to

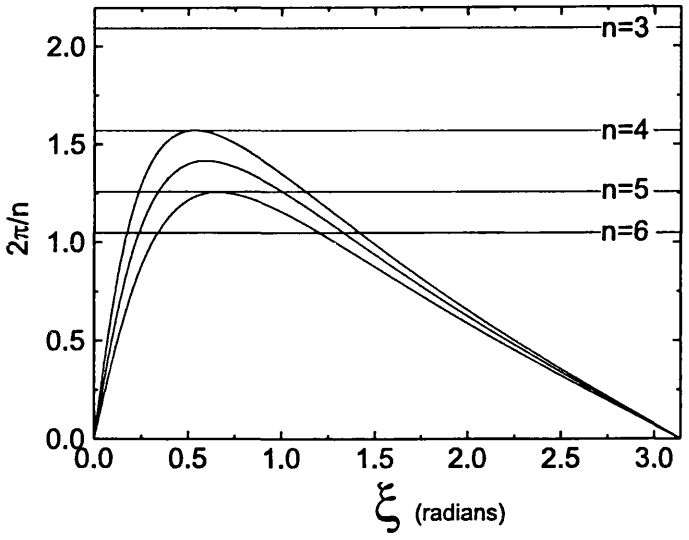

Figure 5.16: A typical graph used to obtain values of B_{ext} at which electron orbits were trapped in a dot. In this case the trapped electrons performed 4 and 5 bounces around the dot. The middle curve represents an untrapped electron (or a trapped one performing multiple orbits).

$$B_{ext} = B_{ext}^{n=3} + (n-3)\Delta B, \tag{5.9}$$

where $B_{ext}^{n=3}$ is the value of the field at which the *n=3* orbit is trapped.

Equation 5.8 was solved graphically in figure 5.16. The value of n was first calculated for a range of electron incident angles ξ between 0 and π (the range π to 2π is a mirror image of this), and then $2\pi/n$ was plotted against ξ. On the same plot, the lines corresponding to *n=3,4,5..* were also plotted, with the solutions obtained when such lines were tangents to the curve. This was performed for the values of electron density investigated in the experiment. Figure 5.16 shows one graph for $n_s = 10.236 \times 10^{15}\mathrm{m}^{-2}$ with three superimposed curves corresponding to *n=4 and 5* and one at the field at which the quantisation condition is not satisfied (curve between *n=4 and 5* lines).

The model correctly predicts, without imposing any conditions, that *n=3* is the lowest possible orbit. However, it fails to correctly predict the dependence of the orbit period on electron density. Comparing the results of the model and experiment, shown in figure 5.17, good agreement is noted at $V_g = +0.12, +0.14, +0.24V$,

corresponding to experimentally measured electron densities $n_s = 10.059$, 10.236, $11.115 \times 10^{15}\mathrm{m}^{-2}$, respectively. In order to achieve this agreement between theory and experiment, electron depletion of the 2DEG under the dot was assumed. Such depletion is not uncommon since, even though magnetic modulation dominates, there will be some electrostatic strain between dysprosium and the wafer. Additionally, because the gate was fabricated after the dots were made, it was only effective in the regions where it was in contact with the surface of the wafer [23], and the electron density measured on Hall crosses covered uniformly by the gate is not necessarily the same as the density under the dot. The densities used to calculate the n were $2.6 \times 10^{15}\mathrm{m}^{-2}$ and $5.8 \times 10^{15}\mathrm{m}^{-2}$, for comparison with experimental sweeps taken at gate voltages of 0.12 and 0.14V. The $V_g = +0.24V$ line was reproduced using the value of electron density from experiment. In this case, the theory also reproduced the slight curvature of the $\lambda - B$ line observed in the experimental results.

Ideally, it was expected that the theory would predict the same number of bounces around the dot as were observed in the experiment ($n = \lambda$). However, the best fit was obtained by shifting the theoretical lines by one, $\lambda = n + 1$. This was justified because extrapolating these lines to zero-field resulted in λ axis intercept being 0, which meant that no electrons were trapped when $B_{ext} = 0$. Theoretical lines had a cut-off at $B \sim 0.15$T (~ 0.18T in the figure) due to the suppression of ring modes ($a_2 < 1$). The dependence of oscillation period on electron density in the case of anti-dots is the same as that predicted by the theory, so no depletion of the 2DEG had to be assumed. It is believed that the different n_s dependence stems from the fact that an anti-dot is an exact inverse of the dot.

Figure 5.18 shows an orbit superimposed on the exact magnetic field profile of a $2\mu m$ diameter dot. The x- and y-coordinates of the orbit were calculated by integrating equations 5.4 and 5.5, respectively. It is a solution when the external magnetic field was $B = 0.4$ and electrons performed 18 bounces.

5.5 Summary

In summary, magnetoresistance was measured in samples modulated by disks and anti-disks of dysprosium. B-periodic oscillations were observed in both longitudi-

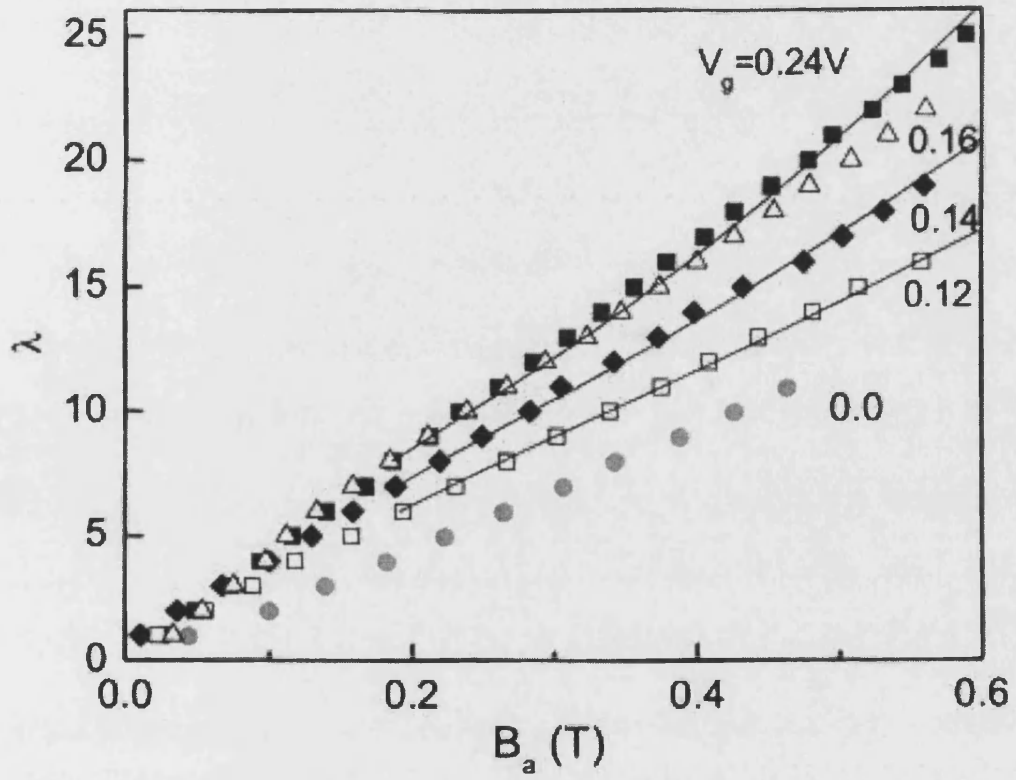

Figure 5.17: Oscillation minima plotted against field at which they appear in magnetoresistance as a function of gate voltage. The full lines correspond to a theoretical fit using the values of electron density as specified in the text. Good agreement between theory and experiment is seen for the V_g = 0.12, 0.14 and 0.24V branches.

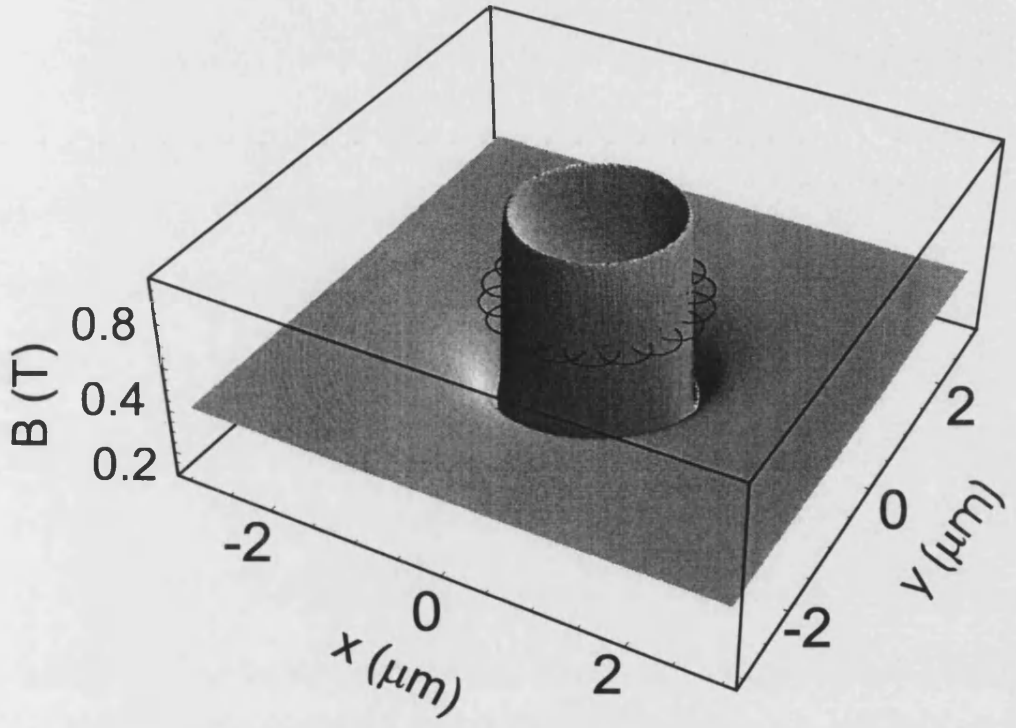

Figure 5.18: The orbit of an electron which performs 18 bounces in a singly-periodic orbit around a $2\mu m$ diameter dot. It is an exact solution of a calculation when the external magnetic field was $B_{ext} = 0.4$T.

nal and bend resistance, and transverse resistance was seen to become non-linear as a consequence of stray magnetic field. In this semi-classical systems, stable orbits were distinguished from the chaotic background because they have trajectories which return to the same point in space after a single revolution around the dot.

Chapter 6

Conclusion and future work

6.1 Conclusion

In summary, transport coefficients of two dimensional electrons gases in inhomogeneous magnetic fields and electrostatic billiards have been investigated. It has been concluded that phonon-drag thermopower changes from B-independent to B-dependent quantity in the presence of a periodic electrostatic potential. The change in field dependence of S^g is due to the anisotropic scattering between electron and phonon systems. The folding of Brillouin zones in the presence of the periodic potential clearly shows that principal axes of anisotropy exist in the system. Thermopower commensurability oscillations (TCOs) were found to have the same dependence on electron density as the well-known commensurability oscillations in resistance(RCOs), and furthermore, there was no phase difference between the two types of oscillations. This fact allowed the distinction to be made between diffusion commensurability oscillations which were 90° out of phase with resistance. However, at increasing values of electron density, small antisymmetric component was observed in TCOs. Close to saturation n_s, this became a 180° phase shift and oscillations were completely anti-symmetric around zero-field. No such antisymmetry was observed in resistance measured at the same density. This effect was explained by assuming that an effective temperature gradient was induced when the applied temperature gradient was not applied parallel to one of the principal axes of symmetry. The effect of such a gradient is amplified at high electron densities, and this is the reason why the 180° phase shift was only

observed at high n_s.

An exact solution of Boltzmann equation, driven by anisotropic scattering rate, correctly reproduced the thermopower commensurability oscillations. The anti-symmetry of theoretical curves also qualitatively agreed with experiment. Slight increase of the fitting parameter b_2, analogous to changing the angle between the applied temperature gradient and the anisotropy axis by only a few degrees, was enough to reproduce the 180° phase shift.

The work described in chapters 4 and 5 reported on the study of dynamical chaos in electron systems. In chapter 4, it was seen that diffusion thermopower of Sinai billiards is a useful tool in distinguishing between stable and chaotic orbits. Commensurability effects arising form electrons bouncing off anti-dots were observed in both longitudinal and transverse magnetoresistance. In diffusion thermopower, these effects were much more pronounced, with peaks observed in longitudinal thermopower whenever electron's cyclotron diameter was equal to the period of the anti-dot chain. At the same condition, the transverse component changed sign. A theoretical model, based on the Landauer-Büttiker treatment of a multiprobe conductor, was developed, and the results of Monte Carlo simulations agreed well with experimental observations. It was noticed, however, that the theory could be simplified by assuming that the main features of longitudinal and transverse components of thermopower were determined by magnetic field derivatives of transmission coefficients T_F and T_L respectively (refer to chapter 5 for definition of these coefficients).

Finally in chapter 4, B-periodic oscillations were seen to arise in magnetoresistance of 2DEGs modulated by a disk of ferromagnetic material. These oscillations were explained by assuming that electrons orbit the disk in cycloid states, characteristic of systems in which a magnetic gradient exists. Electrons become trapped in such states and perform n bounces around the disk, with the condition that they return to the point of departure after just one revolution. These orbits were defined as being singly-periodic and more stable than the multi-periodic ones in which the electron returns to the point of departure after more than one revolution. The condition that the electron returns to the point of departure places a quantisation condition on the angle at which it enters the region under the disk. Trapping of electrons by the potential occurs only at discrete values of magnetic field. Assuming that at field B_{ext} an electron is trapped and performs n bounces,

increasing the field slightly results in the untrapping of this orbit. The next trapped orbit, $n+1$, occurs when the external field reaches a value $B_{ext} + \Delta B$ where ΔB is the period of oscillation. Such trapping/untrapping model leads to oscillatory magnetoresistance (peak when an electron is trapped, minimum when it is untrapped), and correctly predicts the experimental results. B-periodic oscillations were observed in longitudinal resistance of dots and bend resistance of anti-dots. However, one major difference was observed in the dependence of oscillations on electron density in the two cases. The period of oscillations was seen to decrease with increasing density in the dots, whereas it was seen to increase in the case of anti-dots. This observation was explained by the fact that the dots and anti-dots induce effectively inverse magnetic potentials. No oscillatory behaviour was observed in the longitudinal resistance of 3 and $4\mu m$ diameter dots at 4.2K, however, this was restored when the experiments were performed at 600mK. This led to the conclusion that the stability of electron orbits depends strongly on the mean free path of the electron. This experiment showed that stable singly-periodic orbits can be distinguished from the background of multiperiodic ones.

6.2 Future work

At the end of chapter 3, a discussion was started into the possibility of experimental study of effects of tilted temperature gradients on the symmetry of phonon-drag thermopower. Samples with four individual heaters, not joined to the Hall channel, were fabricated, and preliminary studies performed. By varying the amount of heating current applied to each heater, the angle of the gradient was varied and some antisymmetry was observed. However, more work is definitely required in this field in order to obtain a conclusive picture of phonon-drag thermopower in lateral surface superlattices.

Another area which might be of interest involves the fabrication of samples in which the electron system is modulated by a purely magnetic potential. As it was discovered in the superlattice work, dysprosium oxidises very quickly if left exposed to air. In such an oxidised state, the magnetic properties of it are destroyed and the resulting modulation of the electron system was not magnetic but electrostatic. However, careful fabrication of the superlattice and the patterning

of a gate layer on top of it to prevent oxidation, would result in the dominance of magnetic modulation. This was seen in the case of lateral surface dots and anti-dots in which gate layer was fabricated and dysprosium retained it's magnetic properties. Such samples would allow the study of field dependence of phonon-drag thermopower in inhomogeneous magnetic fields. A definitive answer could then be given to the question whether anisotropic scattering rate arises solely due to the electrostatic potential, or whether the presence of any type of periodic potential is sufficient to break the compensation between thermoelectric and drift currents and lead to field dependent phonon-drag thermopower.

The work performed on standing waves of magnetic edge states is possibly one in which more experimental and theoretical work would be useful. The observation of B-periodic oscillations and their strong dependence on mean free path of electrons and the strength of magnetic potential is definitely an interesting phenomenon, however, a more systematic study of such dependence would lead to better understanding. The theoretical model developed is sufficient to explain the behaviour of the electron orbits, however, it fails to correctly predict the dependence of oscillation period on electron density. However, the difficulties encountered in the fabrication of nanostructures in general, and dot and anti-dot patterns in particular, might prove to be an experimental obstacle.

Appendix A

Orbit quantisation angles

This appendix outlines the derivation of angles θ_1 and θ_2 (equations 5.6 and 5.7), which were used in the definition of quantisation condition 5.8. Figure A.1 shows the schematic diagram of the problem.

An electron, moving with initial velocity v_F, is assumed to be incident on the dot profile at an angle ξ with respect to the tangent. The magnetic field, applied in the z-direction, varies in the x-y plane and has the form $\mathbf{B} = (0, 0, B(x, y))$. The equation of motion of the electron is given by

$$m\frac{d\mathbf{v}}{dB} = q\mathbf{v} \times \mathbf{B}. \tag{A.1}$$

Expanding the vector product of equation A.1, the force on the electron is given by

$$m\frac{d\mathbf{v}}{dt} = -e\begin{bmatrix} v_x \\ v_y \\ 0 \end{bmatrix} \times \begin{bmatrix} 0 \\ 0 \\ B \end{bmatrix} = -e\begin{bmatrix} v_y B \\ -v_x B \\ 0 \end{bmatrix}. \tag{A.2}$$

Expressing this in terms of the individual components in the x- and y-directions gives

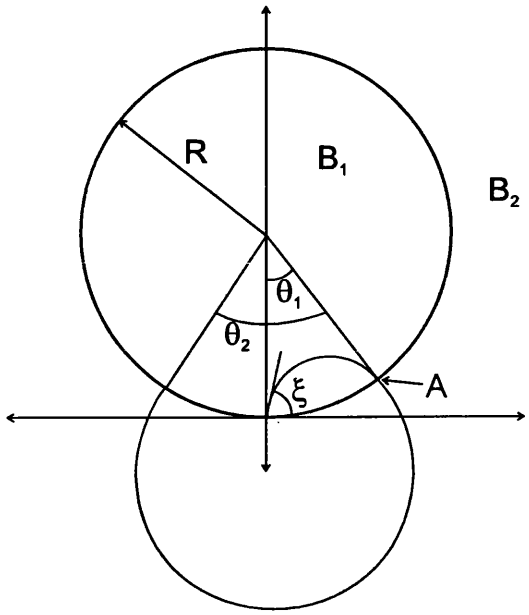

Figure A.1: Schematic diagram of the dot showing angles $\theta_{1,2}$ and ξ.

$$\begin{aligned} m\frac{dv_x}{dt} &= -ev_yB \Rightarrow \frac{dv_x}{dt} = -\omega_c v_y \\ m\frac{dv_y}{dt} &= ev_xB \Rightarrow \frac{dv_y}{dt} = \omega_c v_x, \end{aligned} \tag{A.3}$$

where ω_c is the cyclotron frequency of an electron. The x- and y-components of velocity can then be written as

$$\begin{aligned} v_x &= v_F cos(\omega_c t + \xi) \\ v_y &= v_F sin(\omega_c t + \xi) \end{aligned} \tag{A.4}$$

Integrating these two equations gives the x- and y-coordinates of an electron at a time t,

$$x = \frac{v_F}{\omega_c}\left[sin(\omega_c t + \xi) - sin(\xi)\right]$$
$$y = \frac{v_F}{\omega_c}\left[cos(\xi) - cos(\omega_c t + \xi)\right] \tag{A.5}$$

Considering the dot as the circle of radius R and with the geometry shown in figure A.1, the equation of the circle is $x^2+(y-R)^2 = R^2$. Substituting equations A.5 into this gives

$$4sin^2(\frac{\omega_c t}{2})cos^2(\frac{\omega_c t}{2} + \xi) + \left[2sin(\frac{\omega_c t}{2} + \xi)sin(\frac{\omega_c t}{2}) - a\right]^2 = a^2,$$

where $a = (R\omega_c)/(v_F)$, and simplifying the equation above gives

$$sin^2(\frac{\omega_c t}{2}) - asin(\frac{\omega_c t}{2} + \xi)sin(\frac{\omega_c t}{2}) = 0. \tag{A.6}$$

This equation is only true if $sin(\frac{\omega_c t}{2}) = 0$, or $sin(\frac{\omega_c t}{2}) = asin(\frac{\omega_c t}{2} + \xi)$. The first equation has a trivial solution

$$t = \frac{2n\pi}{\omega_c}. \tag{A.7}$$

It corresponds to an electron returning (with $n = 0, 1, 2, 3..$) to the point of departure. The second equation gives t_A, the time at which an electron intercepts the perimeter:

$$cos(\omega_c t_A) = \frac{[1 - acos\xi]^2 - [asin\xi]^2}{[1 - acos\xi]^2 + [asin\xi]^2},$$
$$sin(\omega_c t_A) = \frac{2asin\xi[1 - acos\xi]}{[1 - acos\xi]^2 + [asin\xi]^2}. \tag{A.8}$$

Substituting A.8 into A.5 gives the x- and y-coordinates of the electron at t_A as

$$x_A = \frac{v_F}{\omega_c}\left[\frac{2asin\xi[cos\xi - asin\xi]}{[1 - acos\xi]^2 + [asin\xi]^2}\right]$$
$$y_A = \frac{v_F}{\omega_c}\left[\frac{2asin^2\xi}{[1 - acos\xi]^2 + [asin\xi]^2}\right]. \tag{A.9}$$

Under the area of the dot the field is B_1 and therefore the cyclotron frequency can be expressed as $\omega_{c,1} = eB_1/m$, and a_1 can be taken to be positive assuming B_1 is positive. Therefore, by knowing $x(t_A)$ and $y(t_A)$, and through simple trigonometric analysis, angle θ_1 becomes

$$cos\theta_1 = \frac{R - y_1}{R} = 1 - \frac{1}{a_1}\left[\frac{2a_1sin^2\xi}{[1 - a_1cos\xi]^2 + [a_1sin\xi]^2}\right]. \tag{A.10}$$

Similarly, angle θ_2 is given by

$$cos\theta_2 = 1 - \frac{1}{a_2}\left[\frac{2a_2sin^2\xi}{[1 - a_2cos\xi]^2 + [a_2sin\xi]^2}\right], \tag{A.11}$$

where $a_2 = (R\omega_2)/(v_F)$ and $\omega_{c,2} = eB_2/m$. In a singly periodic orbit, the electron returns to the point of departure (0,0), and this is fulfilled when an integral number of angles is equal to 2π, in other words, when the quantisation condition

$$n|\theta_1 - \theta_2| = 2\pi \tag{A.12}$$

is satisfied.

References

[1] A. Y. Cho, J. Vac. Sci. Technol. **8**, 31 (1971).

[2] B. J. Curtis and H. R. Brunner, Mat. Res. Bull. **10**, 515 (1975).

[3] K. von Klitzing, G. Dorda, and M. Pepper, Phys. Rev. Lett. **45**, 494 (1980).

[4] D. C. Tsui, H. L. Stormer, and A. C. Gossard, Phys. Rev. Lett. **48**, 1559 (1982).

[5] T. S. Tighe, J. M. Worlock, and M. L. Roukes, Appl. Phys. Lett. **70**, 2687 (1997).

[6] K. Schwab, E. A. Henriksen, J. M. Worlock, and M. L. Roukes, Nature **404**, 974 (2000).

[7] D. Weiss, K. von Klitzing, K. Ploog, and G. Weimann, Europhys. Lett. **8**, 179 (1989).

[8] R. Taboryski, B. Brosh, M. Y. Simmons, D. A. Ritchie, C. J. B. Ford, and M. Pepper, Phys. Rev. B **51**, 17243 (1995).

[9] C. W. J. Beenakker, Phys. Rev. Lett. **62**, 2020 (1989).

[10] D. Weiss, G. Lutjering, and K. Richter, Chaos, Solitons and Fractals **8**, 1337 (1997).

[11] Y. G. Sinai, Usp. Mat. Nauk. **25**, 141 (1970).

[12] K. S. Novoselov, A. K. Geim, S. V. Dubonos, Y. G. Cornelissens, F. M. Peeters, and J. C. Maan, Phys. Rev. B **65**, 233312 (2002).

[13] U. B. Clean-room, Calibration graph of spin-speed against photo-resist thickness for the particular case of Shipley SU1813 resist .

[14] Raith, *Elphy Plus Users manual*, Raith GmbH, 2001.

[15] A. G. Pogosov, M. V. Budantsev, O. V. Kibis, A. Pouydebasque, D. K. Maude, and J. C. Portal, Phys. Rev. B **61**, 15603 (2000).

[16] F. M. Peeters and P. Vasilopoulos, Phys. Rev. B **47**, 1466 (1993).

[17] M. Suhrke, O. Steffens, P. Rotter, and U. Rössler, Physica E **1**, 281 (1997).

[18] P. D. Ye, D. Weiss, K. von Klitzing, K. Eberl, and H. Nickel, Appl. Phys. Lett. **67**, 1441 (1995).

[19] F. Evers, A. D. Mirlin, D. G. Polyakov, and P. Wölfle, Phys. Rev. B **60**, 8951 (1999).

[20] F. M. Peeters and P. Vasilopoulos, Phys. Rev. B **42**, 5899 (1990).

[21] R. R. Gerhardts, D. Weiss, and K. von Klitzing, Phys. Rev. Lett. **62**, 1173 (1989).

[22] P. Ye, D. Weiss, R. R. Gerhardts, K. Seeger, K. von Klitzing, K. Eberl, and H. Nickel, Phys. Rev. Lett. **74**, 3013 (1995).

[23] P. H. Beton, E. S. Alves, P. C. Main, L. Eaves, M. W. Dellow, M. Henini, O. H. Hughes, S. P. Beaumont, and C. D. W. Wilkinson, Phys. Rev. B **42**, 9229 (1990).

[24] R. W. Winkler, J. P. Kotthaus, and K. Ploog, Phys. Rev. Lett. **62**, 1177 (1989).

[25] J. H. Smet, S. Jobst, K. von Klitzing, D. Weiss, W. Wegscheider, and V. Umansky, Phys. Rev. Lett. **83**, 2620 (1999).

[26] K. W. Edmonds, B. L. Gallagher, P. Main, N. Overend, R. Wirtz, A. Nogaret, M. Henini, C. H. Marrows, B. J. Hickey, and S. Thoms, Phys. Rev. B **64**, 041303 (2001).

[27] A. Nogaret, S. J. Bending, and M. Henini, Phys. Rev. Lett. **84**, 2231 (2000).

[28] C. Herring, Phys. Rev. **95**, 1163 (1954).

[29] H. P. R. Frederikse, Phys. Rev. **92**, 248 (1953).

[30] T. H. Geballe and G. W. Hull, Phys. Rev. **94**, 1134 (1954).

[31] B. Tieke, R. Fletcher, U. Zeitler, M. Henini, and J. C. Maan, Phys. Rev. B **58**, 2017 (1998).

[32] M. Tsaousidou, P. N. Butcher, and G. P. Triberis, Phys. Rev. B **64**, 165304 (2001).

[33] P. W. Anderson, E. Abrahams, and T. V. Ramakrishnan, Phys. Rev. Lett. **43**, 718 (1979).

[34] L. P. Gorkov, A. I. Larkin, and D. E. Khmel'nitskii, [Pis'ma Zh. Eksp. Teor. Fiz. **30**, 248 (1979)] JETP Lett. **30**, 228 (1979).

[35] A. Miele, R. Fletcher, E. Zaremba, Y. Feng, C. T. Foxon, and J. J. Harris, Phys. Rev. B **58**, 13181 (1998).

[36] D. G. Cantrell and P. N. Butcher, J. Phys. C: Solid State Physics **20**, 1985 (1987).

[37] D. J. Spence, T. C. Q. Noakes, P. Bailey, and S. P. Tear, (erratum published Phys. Rev. B 63 049901 2001), Phys. Rev. B **62**, 5016 (2000).

[38] I. A. Larkin, J. H. Davies, A. R. Long, and R. Cusco, Phys. Rev. B **56**, 15242 (1997).

[39] A. D. Mirlin and P. Wolfle, Phys. Rev. B **58**, 12986 (1998).

[40] B. L. Gallagher, P. N. Butcher, T. Moss (Ed.), and P. T. Landsberg(Ed.), Handbook on semiconductors **1**, 14 (1992).

[41] R. Fletcher, J. J. Harris, C. T. Foxon, M. Tsaousidou, and P. N. Butcher, Phys. Rev. B **50**, 14991 (1994).

[42] D. Uzur, A. Nogaret, A. G. Pogosov, H. E. Beere, and D. A. Ritchie, J. Phys. Cond. Matt. **15**, 6985 (2003).

[43] A. J. Kent, *Hot electrons in semiconductors*, Clarendon Press (Oxford), 1988.

[44] A. G. Pogosov, M. V. Budantsev, D. Uzur, A. Nogaret, A. E. Plotnikov, A. K. Bakarov, and A. I. Toropov, Phys. Rev. B **66**, 201303 (2002).

[45] M. J. Kearney, R. T. Syme, and M. Pepper, Phys. Rev. Lett. **66**, 1622 (1991).

[46] S. F. Godijn, S. Moller, H. Buhmann, L. W. Molenkamp, and S. A. van Langen, Phys. Rev. Lett. **82**, 2927 (1999).

[47] L. Onsager, Phys. Rev. **37**, 405 (1931).

[48] P. N. Butcher and M. Tsaousidou, Phys. Rev. Lett. **80**, 1718 (1998).

[49] M. Prasad and M. Singh, Phys. Rev. B **29**, 4803 (1984).

[50] A. Nogaret, Phys. Rev. B **66**, 125302 (2002).

[51] W. Thomson, Trans. Roy. Soc. Edin. **21**, 153 (1857).

[52] M. Buttiker, Phys. Rev. Lett. **57**, 1761 (1986).

[53] H. U. Baranger, D. P. DiVincenzo, R. A. Jalabert, and A. D. Stone, Phys. Rev. B **44**, 10637 (1991).

[54] S. Moller, H. Buhmann, S. F. Godijn, and L. W. Molenkamp, Phys. Rev. Lett. **81**, 5197 (1998).

[55] R. Fleischmann, T. Geisel, and R. Ketzmerick, Phys. Rev. Lett. **68**, 1367 (1992).

[56] M. J. Kelly, *Low dimensional semiconductors*, Clarendon Press, 1995.

[57] L. W. Molenkamp, H. van Houten, C. W. J. Beenakker, R. Eppenga, and C. T. Foxon, Phys. Rev. Lett. **65**, 1052 (1990).

[58] A. S. Dzurak, C. G. Smith, C. H. W. Barnes, M. Pepper, L. Martin-Moreno, C. T. Liang, D. A. Ritchie, and G. A. C. Jones, Phys. Rev. B **55**, 10197 (1997).

[59] S. Moller, H. Buhmann, S. F. Godijn, and L. W. Molenkamp, Phys. Rev. Lett. **81**, 5197 (1998).

[60] U. Sivan and Y. Imry, Phys. Rev. B **33**, 551 (1986).

[61] J. Eroms, M. Tolkiehn, D. Weiss, U. Rossler, J. De Boeck, and S. Borghs, Europhys. Lett. **58**, 569 (2002).

[62] A. Lorke, J. P. Kotthaus, and K. Ploog, Phys. Rev. B **44**, 3447 (1991).

[63] X. Kleber, G. M. Gusev, U. Gennser, D. K. Maude, J. C. Portal, D. I. Lubyshev, P. Basmaji, M. d. P. A. Silva, J. C. Rossi, and Y. A. Nastaushev, Phys. Rev. B **54**, 13859 (1996).

[64] K. Hornberger and U. Smilansky, Phys. Rev. Lett. **88**, 024101 (2002).

[65] Z. Voros, T. Tasnadi, J. Cserti, and P. Pollner, Phys. Rev. E **67**, 065202 (2003).

[66] D. N. Lawton, A. Nogaret, S. J. Bending, D. K. Maude, J. C. Portal, and M. Henini, Phys. Rev. B **64**, 033312 (2001).

[67] J. Reijniers, F. M. Peeters, and A. Matulis, Phys. Rev. B **64**, 245314 (2001).

[68] J. Reijniers, F. M. Peeters, and A. Matulis, Phys. Rev. B **59**, 2817 (1999).

[69] F. M. Peeters and X. Q. Li, Appl. Phys. Lett. **72**, 572 (1998).

[70] I. S. Ibrahim, V. A. Schweigert, and F. M. Peeters, Phys. Rev. B **57**, 15416 (1998).

[71] H. S. Sim, G. Ihm, N. Kim, and K. J. Chang, Phys. Rev. Lett. **87**, 146601 (2001).

[72] H.-S. Sim, K. H. Ahn, K. J. Chang, N. Ihm, G. Kim, and S. J. Lee, Phys. Rev. Lett. **80**, 1501 (1998).

[73] Y. Takagaki and D. K. Ferry, Phys. Rev. B **48**, 8152 (1993).

[74] S. J. Bending and A. Oral, J. Appl. Phys. **81**, 3721 (1997).

[75] S. J. Bending, K. von Klitzing, and K. Ploog, Phys. Rev. Lett. **65**, 1060 (1990).

[76] A. K. Geim, S. J. Bending, and I. V. Grigorieva, Phys. Rev. Lett. **69**, 2252 (1992).

[77] C. W. J. Beenakker and H. van Houten, *Quantum transport in semiconductor nanostructures, Solid state physics vol. 44*, Academic Press Inc., 1991.

[78] A. O. Volkov, K. S. Novoselov, M. Missous, S. V. Morozov, S. V. Dubonos, and A. K. Geim, Workbook of CMMP03 (2003).

[79] D. Craik, *Magnetism: Principles and Applications*, Wiley, 1995.

[80] D. Uzur, A. Nogaret, S. J. Bending, C. H. Marrows, B. J. Hickey, H. E. Beere, and D. A. Ritchie, Physica E (also published in Workbook of EP2DS-15 Conference, Japan) (2003).

[81] D. Uzur, A. Nogaret, H. E. Beere, D. A. Ritchie, C. H. Marrows, and B. J. Hickey, submitted to Phys. Rev. B (2003).